Classical and Quantum Effects in Plasmonic Metals

Thesis by
Ana Maii Brown

In Partial Fulfillment of the Requirements for the
degree of
Doctor of Philosophy

CALIFORNIA INSTITUTE OF TECHNOLOGY
Pasadena, California

2016
Defended April 20, 2016

© 2016

Ana Maii Brown
ORCID: 0000-0003-3008-2310

All rights reserved

ACKNOWLEDGEMENTS

First and foremost, and with much gratitude, I thank my adviser, Professor Harry Atwater, for his kind guidance and never-tiring enthusiasm and support. I certainly would not have made it through earning a PhD without his encouragement and unwavering confidence in me. I would also like to thank all of the Atwater Group members and staff, and especially Matt Sheldon and Ravishankar Sundararaman for their patient mentorship, and Jennifer Blankenship, Tiffany Kimoto, Daniel Turner-Evans, and Carissa Eisler for their genuine friendship. I am thankful for the blessing of having David Ayala in my life. David has made me a better person, and makes life, with all its mundane and epic moments, more vivid and exquisite. Finally, it is with deep gratitude that I thank my parents, Norm and Adelina, and my sister, Robin, for their unconditional love and steadfast support. Adelina's inherent strength and humble wisdom, Norm's unending curiosity and love, and Robin's ingenuity and devotion to family have shaped me, and yet still leave me in awe.

I am grateful for the generous financial support for my studies and for the work in this thesis, mainly provided by the National Science Foundation and the Link Energy Foundation.

Ana Maii Brown
April 2016

ABSTRACT

The field of plasmonics exploits the unique optical properties of metallic nanostructures to concentrate and manipulate light at subwavelength length scales. Metallic nanostructures get their unique properties from their ability to support surface plasmons– coherent wave-like oscillations of the free electrons at the interface between a conductive and dielectric medium. Recent advancements in the ability to fabricate metallic nanostructures with subwavelength length scales have created new possibilities in technology and research in a broad range of applications.

In the first part of this thesis, we present two investigations of the relationship between the charge state and optical state of plasmonic metal nanoparticles. Using experimental bias-dependent extinction measurements, we derive a potential-dependent dielectric function for Au nanoparticles that accounts for changes in the physical properties due to an applied bias that contribute to the optical extinction. We also present theory and experiment for the reverse effect– the manipulation of the carrier density of Au nanoparticles via controlled optical excitation. This plasmoelectric effect takes advantage of the strong resonant properties of plasmonic materials and the relationship between charge state and optical properties to elucidate a new avenue for conversion of optical power to electrical potential.

The second topic of this thesis is the non-radiative decay of plasmons to a hot-carrier distribution, and the distribution's subsequent relaxation. We present first-principles calculations that capture all of the significant microscopic mechanisms underlying surface plasmon decay and predict the initial excited carrier distributions so generated. We also preform *ab initio* calculations of the electron-temperature dependent heat capacities and electron-phonon coupling coefficients of plasmonic metals. We extend these first-principle methods to calculate the electron-temperature dependent dielectric response of hot electrons in plasmonic metals, including direct interband and phonon-assisted intraband transitions. Finally, we combine these first-principles calculations of carrier dynamics and optical response to produce a complete theoretical description of ultrafast pump-probe measurements, free of any fitting parameters that are typical in previous analyses.

PUBLISHED CONTENT AND CONTRIBUTIONS

Portions of this thesis have been drawn from the following publications:

1. Sheldon, M. T., Van de Groep, J., Brown, A. M., Polman, A. & Atwater, H. A. Plasmoelectric potentials in metal nanostructures. *Science* **346,** 828–831 (2014).
   doi:10.1126/science.1258405.

2. Brown, A. M., Sheldon, M. T. & Atwater, H. A. Electrochemical Tuning of the Dielectric Function of Au Nanoparticles. *ACS Photonics* **2,** 459–464 (2015).
   doi:10.1021/ph500358q.

3. Brown, A. M., Sundararaman, R., Narang, P., Goddard III, W. A. & Atwater, H. A. Non-Radiative Plasmon Decay and Hot Carrier Dynamics: Effects of Phonons, Surfaces and Geometry. *ACS Nano* **10,** 957–966 (2015).
   doi:10.1021/acsnano.5b06199.

4. Brown, A. M., Sundararaman, R., Narang, P., Goddard III, W. A. & Atwater, H. A. Ab initio phonon coupling and optical response of hot electrons in plasmonic metals. *Physical Review B* (2016). Submitted.

5. Brown, A. M., Sundararaman, R., Narang, P., Schwartzberg, A. & Atwater, H. A. Ultrafast carrier experimental and ab initio dynamics in plasmonic nanoparticles (2016). In preparation.

TABLE OF CONTENTS

Acknowledgements . . . iii
Abstract . . . iv
Published Content and Contributions . . . v
Table of Contents . . . vi
List of Illustrations . . . viii
List of Tables . . . x
Chapter I: Introduction . . . 1
1.1 Properties and Applications of Plasmonic Metallic Nanoparticles . . . 1
1.2 The Drude and Lorentz-Drude Models . . . 3
1.3 Mie Theory: Scattering of Light by Nanospheres . . . 4
1.4 Beyond the Lorentz-Drude Todel and Mie Theory . . . 5
1.5 Scope of This Thesis . . . 5
Chapter II: The Plasmoelectric Effect . . . 8
2.1 Charge Dependent Dielectric Function . . . 8
2.2 Thermodynamic Model . . . 10
2.3 Temperature Calculations . . . 14
2.4 Calculation of Steady-State Nanoparticle Surface Potential and Charge 17
2.5 Charge Accumulation Shell Model . . . 18
2.6 Nanoparticle Emissivity . . . 19
2.7 FDTD Simulation Methods . . . 20
2.8 Plasmoelectric Simulations . . . 21
2.9 Kelvin Probe Force Microscopy Experiments . . . 23
2.10 Optical Measurements of Nanoparticles Under Monochromatic Illumination . . . 28
2.11 Conclusions . . . 32
Chapter III: Electrical Tuning of the Dielectric Function and Optical Properties of Nanoparticles . . . 33
3.1 Previous Work and Overview . . . 33
3.2 Electrochemical Cell Fabrication . . . 34
3.3 Optical Measurements of Nanoparticles Under Applied Bias . . . 36
3.4 Modeling Optoelectronic Effects with FDTD Simulations . . . 40
3.5 Comparison of Simulation and Experimental Results . . . 43
3.6 Conclusions . . . 47
Chapter IV: Complete *ab initio* Description of Non-Radiative Plasmon Decay 49
4.1 Motivation and Previous Work . . . 49
4.2 Experimental Decay Rate . . . 51
4.3 Electronic Structure . . . 52
4.4 Plasmon Decay via Direct Transitions . . . 53
4.5 Plasmon Decay via Phonon-assisted Transitions . . . 54

4.6 Phonon Modes and Matrix Elements . . . 56
4.7 Surface-assisted Transitions . . . 57
4.8 Estimate of Resistive Losses . . . 58
4.9 Results for Common Plasmonic Metals . . . 60
4.10 Conclusions . . . 65
Chapter V: *Ab initio* Description of Hot Electron Relaxation in Plasmonic Metals . . . 66
5.1 Motivation and Previous Work . . . 66
5.2 Computational Methods . . . 69
5.3 Electronic Density of States and Heat Capacity . . . 69
5.4 Phononic Density of States and Heat Capacity . . . 72
5.5 Electron-phonon Matrix Element and Coupling . . . 74
5.6 Temperature Dependent Dielectric function . . . 79
5.7 Conclusions . . . 87
Chapter VI: Experimental and *ab initio* Ultrafast Carrier Relaxation in Plasmonic Nanoparticles . . . 89
6.1 Motivation and Background . . . 89
6.2 *Ab initio* theory . . . 93
6.3 Experimental Methods . . . 99
6.4 Results . . . 99
6.5 Conclusions . . . 104
Chapter VII: Summary and Outlook . . . 106
Bibliography . . . 109
Appendix A: Derivations of Expressions for Direct and Phonon-Assisted Plasmon Decay . . . 121
A.1 Direct Transitions . . . 121
A.2 Phonon-Assisted Transitions . . . 123
A.3 Final Expressions for Direct and Phonon-assisted Plasmon Decay After Accounting For Reverse Transitions . . . 129
Appendix B: Tabulated Electronic Heat Capacity and Electron-Phonon Coupling Factor as a Function of Electron Temperature . . . 131
Appendix C: Dielectric Function Temperature Dependence Prefactor Derivation . . . 136

LIST OF ILLUSTRATIONS

Number *Page*

1.1 Sketch of surface plasmon 2
2.1 Absorption cross section spectrum of a Ag nanoparticle and the plasmoelectric effect 9
2.2 Plasmoelectricly Induced Electron Density 10
2.3 Plasmoelectricly Induced Temperature Increase 15
2.4 Au nano particle heat diffusion and temperature 17
2.5 Electron Transfer 18
2.6 Plasmoelectric Potential and Absorption 20
2.7 Nanoparticle Emissivity 21
2.8 Modeled plasmoelectric response for Ag nanoparticles 22
2.9 KPFM Surface Potential Map 24
2.10 KPFM Control Measurement 25
2.11 Plasmoelectric effect on dense Au nanoparticles on ITO/glass 26
2.12 Schematic of white vs. monochromatic illumination experimental setup 29
2.13 Plasmoelectric effect for 60 nm Au colloids suspended in water . . . 30
3.1 Electrochemical Cell Geometery 35
3.2 Extinction spectra and changes in spectra of Au colloids in electrochemical cell 37
3.3 Experimental and simulated peak parameters as a function of applied bias 38
3.4 Raw Spectra 39
3.5 FDTD simulation geometry 39
3.6 Physical parameters as a function of applied bias 44
3.7 Comparison of experiment and simulation over full wavelength range 47
4.1 Schematic of Plasmon Decay 50
4.2 Comparison of linewidths 61
4.3 Comparison of contribution to Im(ε) 63
4.4 Carrier Distribution 64
5.1 Fundamental parameters for describing hot electron relaxation 68
5.2 Electronic density of states 70

5.3 Electronic heat capacity as a function of electron temperature 71
5.4 Phonon density of states 73
5.5 Lattice heat capacity as a function of lattice temperature 74
5.6 energy resolved electron-phonon coupling strength 77
5.7 Electron-phonon coupling factor G as a function of electron temperature 78
5.8 *Ab initio* dielectric function at room temperature 82
5.9 Complex dielectric function for T_e = 400K 83
5.10 Change in dielectric function for T_e =300 K to 400 K 83
5.11 Complex dielectric function for T_e = 1000K 84
5.12 Change in dielectric function for T_e =300 K to 1000 K 84
5.13 Complex dielectric function for T_e = 5000K 85
5.14 Change in dielectric function for T_e =300 K to 5000 K 85
5.15 Critical interband transitions for dielectric function temperature dependence 87
6.1 Ultrafast transient absorption setup 89
6.2 Differential extinction map as a function of probe wavelength and delay time 91
6.3 Transient differential extinction spectral and kinetic traces 92
6.4 Extinction of Au colloids used in transient absorption measurements . 92
6.5 Electron distribution relaxation evolution 94
6.6 Kinetic signal amplitude dependence on pump power 101
6.7 Transient signal temporal behavior dependence on pump power . . . 101
6.8 Nonthermalized and thermalized electron distribution dependence on pump power 102
6.9 Transient extinction signal for a variety of probe wavelengths 104
6.10 Transient extinction signal for a variety of probe wavelengths 104

LIST OF TABLES

Number *Page*

3.1 Simulation parameter limits and resolution 42

4.1 *ab initio* parameters for metals 60

5.1 Parameters for dielectric function temperature dependence 81

B.1 Tabulated electronic heat capacity and electron-phonon coupling factor as a function of electron temperature 131

Chapter 1

INTRODUCTION

1.1 Properties and Applications of Plasmonic Metallic Nanoparticles

The field of plasmonics exploits the unique optical properties of metallic nanostructures to route and manipulate light at subwavelength length scales. Recent advancements in the ability to fabricate metallic nanostructures with subwavelength length scales have created new possibilities in technology and research focused on the manipulation of light. Plasmonic metallic nanostructures have been used most successfully to achieve extreme concentration of light, as in plasmonic antennas, lenses and resonators.[1]

Traditionally, light concentration has been achieved with dielectric lenses and resonators but these devices have limitations that are far surpassed by plasmonic-based metallic nanostructures. The smallest spot size that can be produced with dielectric lenses and resonators is approximately $\lambda/2$. Therefore the electromagnetic mode volume in which an optical signal can be concentrated is approximately equal to $(\lambda/2)^3$; metallic nanostructures can be used to concentrate light to volumes much smaller than these traditional limits.

Metallic nanostructures get their unique properties from their ability to support surface plasmons– coherent wave-like oscillations of the free electrons at the interface between a conductive and a dielectric medium (Figure 1.1). Surface plasmons are produced when a time-varying electric field constituting incident light produces a force on the free electrons inside the metal which drives them into a collective oscillation in resonance with the incident electric field. Surface plasmons are transverse magnetic in character, and the generation of surface charge requires an electric field normal to the surface. This leads to the field component normal to surface being enhanced near the surface and decaying exponentially with distance away from it. This field component is evanescent and prevents power from propagating away from the surface. The decay length of the field in the dielectric interfacing with the metal is roughly half of the wavelength of the incident light, whereas the decay length inside the metal is determined by the skin depth.

Surface plasmons come in two varieties: one form, termed a local surface plasmon, is a resonant standing wave on a conductive nanostructure with dimensions on or-

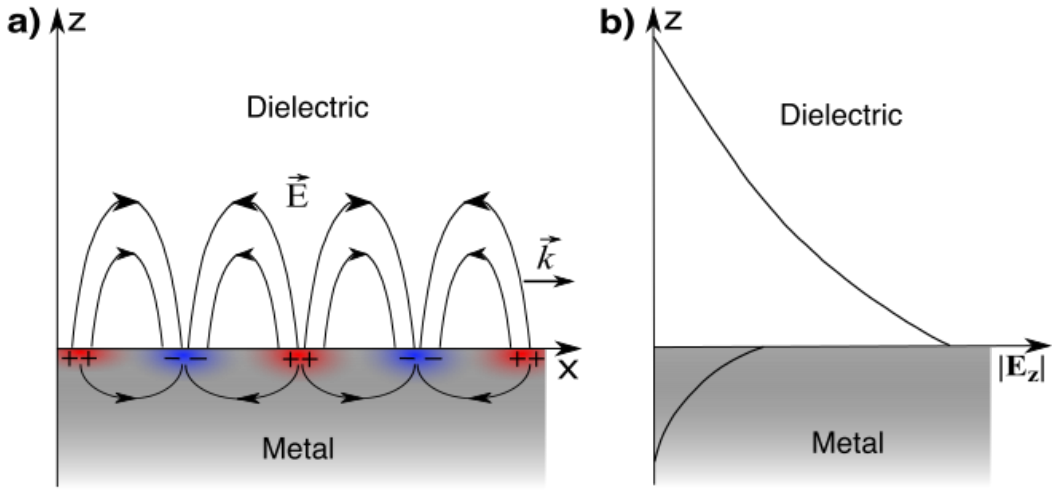

Figure 1.1: Schematic of surface plasmon showing electric fields and oscillating charges. Figure adapted from Reference 2.

der of the exciting optical wavelength; the other form, termed a surface plasmon polariton, is a non-resonant charge-oscillation wave which propagates down the surface of a conductor. Surface plasmon polaritons occur in metal structures with one or more dimensions greater than or equal to the wavelength of incident light; the charge oscillation can propagate down the conducting surface as a surface plasmon polariton mode. Local surface plasmons occur in metallic nanostructures with dimensions significantly shorter than the dimensions of the incident light, where the whole particle is subject to virtually a uniform incident electric field at any one point in time. This results in dipolar charge separation and resonant frequencies, much like the resonances of a standing wave, which produce a very strong charge displacement and associated field concentration.

Plasmons provide a pathway to manipulate electromagnetic radiation at nanometer length scales [1–3] and at femtosecond time scales.[4] Research is currently being conducted to create new passive and active plasmonic devices to generate, guide, modulate, and detect light. Excitation, propagation, and localization of plasmons can be tailored by nanoscale control of size, shape, and architecture.[1, 5] Metal nanostructures exhibiting subwavelength optical confinement [6, 7] have enabled nanoscale photonic waveguides[8, 9], modulators[10], surface plasmons amplified by stimulated emission of radiation (SPASERs)[11, 12], light trapping structures for photovoltaics[13, 14], field enhancement for Raman spectroscopy, and biological labeling techniques[1, 15]. Coupling of laser light to plasmonic structures can result in excitation of extremely high energy densities and efficient localized heating,

because the resonant absorption cross section for plasmonic nanostructures is much larger than their physical cross sections.[16] Recently, there has been considerable interest in plasmonic energy relaxation and conversion mechanisms. Plasmons have relatively short (< 10 fs) lifetimes and can decay into single particle excitations, notably hot electron-hole pairs.[17] Plasmonic resonators have been recently reported to emit optically excited hot electrons across a rectifying metal-semiconductor interface.[18, 19]

Despite more than a decade of intensive scientific exploration, new plasmonic phenomena continue to be discovered, including quantum interference of plasmons, observation of quantum coupling of plasmons to single particle excitations, and quantum confinement of plasmons in single-nanometer scale plasmonic particles. Also, plasmonic structures find widening applications in integrated nanophotonics, biosensing, photovoltaic devices, single photon transistors, and single molecule spectroscopy.

1.2 The Drude and Lorentz-Drude Models

In 1900 Paul Drude proposed a model of electrical conduction to explain the transport and optical properties of electrons in metals.[20, 21] His model approximated a conductor as a collection of free electrons and stationary positively charged ions. In this model, equation of motion for an electron subject to an external electric field $\vec{E}$ is

$$m\frac{d^2\vec{r}}{dt^2} = -m\gamma\frac{d\vec{r}}{dt} - e\vec{E}(\vec{r},t) \tag{1.1}$$

where e is electron charge, m is electron mass, r is the electron displacement from equilibrium, and γ is the harmonic damping constant. By considering the conductivity of this system and the relation $\epsilon = 1 + 4\pi i\sigma/\omega$, we arrive at the Drude dielectric function:

$$\epsilon(\omega) = 1 - \frac{4\pi ne^2/m}{(\omega^2 + i\gamma\omega)} = 1 - \frac{\omega_p^2}{(\omega^2 + i\gamma\omega)} \tag{1.2}$$

where n is the electron density and the plasma frequency is defined as $\omega_p \equiv \sqrt{4\pi ne^2/m}$. The plasma frequency is the resonant frequency of the electrons in the metal. This complex dielectric function accounts for free-electron behavior in metals, and has been used to approximate the dielectric function of metals in countless scientific investigations. However, this model completely neglects the treatment of interband transitions, which become important when incident light has an energy higher than the interband transition threshold.

In 1905, Hendrick Antoon Lorentz extended the Drude model to account for electrons which are bound by a damped harmonic oscillator to an atom or ion in the solid.[22, 23] The equation of motion for an electron in this Lorentz-Drude model in the presence of an external electric field E is given by the Drude-Lorentz equation:

$$m\frac{d^2\vec{r}}{dt^2} = -m\omega_0^2\vec{r} - m\gamma\frac{d\vec{r}}{dt} - e\vec{E}(\vec{r},t) \tag{1.3}$$

where ω_0 is the natural frequency of the oscillator, and the other parameters are the same as those in the Drude model. The dielectric function for this system is given by

$$\epsilon(\omega) = 1 + \frac{4\pi ne^2/m}{(\omega_0^2 - \omega^2 - i\gamma\omega)} = 1 + \frac{\omega_p^2}{(\omega_0^2 - \omega^2 - i\gamma\omega)} \tag{1.4}$$

The Lorentz-Drude model has been used in investigations to approximate the interband contributions to the dielectric function. An extension of the Lorentz-Drude model to more than one oscillator has been used to better approximate the dielectric functions of Ag and Au.[24]

1.3 Mie Theory: Scattering of Light by Nanospheres

Mie theory, which describes the absorption and scattering profiles of a subwavelength sphere illuminated by a plane wave, is named after Gustav Mie, who was the first to electrodynamically describe localized surface plasmon polaritons in metallic nanoparticles in 1908.[25] Using Maxwell's equations, Bohren and Huffman[26] derive the classical analytical solution for the scattering and extinction cross section of the sphere:

$$C_{sca} = \frac{2\pi}{k^2}\sum_{n=1}^{\infty}(2n+1)(|a_n|^2 + |b_n|^2) \tag{1.5}$$

$$C_{ext} = \frac{2\pi}{k^2}\sum_{n=1}^{\infty}(2n+1)Re(a_n + b_n) \tag{1.6}$$

with the scattering coefficients

$$a_n = \frac{\mu m^2 j_n(mx)[xh_n(x)]' - \mu_1 j_n(x)[mxj_n(mx)]'}{\mu m^2 j_n(mx)[xh_n^{(1)}(x)]' - \mu_1 h_n^{(1)}(x)[mxj_n(mx)]'} \tag{1.7}$$

$$b_n = \frac{\mu_1 j_n(mx)[xj_n(x)]' - \mu j_n(x)[mxj_n(mx)]'}{\mu_1 j_n(mx)[xh_n^{(1)}(x)]' - \mu h_n^{(1)}(x)[mxj_n(mx)]'} \tag{1.8}$$

where j_n and h_n are the spherical Bessel functions, x is the size parameter $x = ka$, m is the relative refractive index $m = k_1/k$, k and k_1 are the wave-vectors in the particle and surrounding medium, and μ and μ_1 are the permeabilities of the particles and the surrounding medium, respectively.

1.4 Beyond the Lorentz-Drude Todel and Mie Theory

Mie theory was first experimentally verified in the 1970's, and as advances in technology have made fabrication and characterization of nanoparticles a common research area in recent decades, Mie theory along with the Lorentz-Drude model has been commonly used to describe the optical properties of metallic nanoparticles in a variety of systems. However there are many shortcomings of the Lorentz-Drude model and Mie theory which make them unable to predict or describe nonidealities in real systems, experiments with more complex systems, or microscopic processes related to localized surface plasmons. For example, surfaces and interfaces can change electronic structure and damping, and these effects become more important as the size of nanoparticles decreases.[27, 28] Static or dynamic charge transfer such as those in a system with an applied bias or difference in work function between the plasmonic resonator the the surrounding medium results in a change in the dielectric function and thus to the optical properties.[29, 30] Excitation by incident light leads to an increase in temperature of the electron and phonon bath, resulting in changes in the dielectric function as well as in the heat capacity and electron-phonon coupling.[17, 31, 32] When we examine plasmonic behavior at very short time scales, quantum effects become important.[33–35] Without corrections for these and other effects, Mie theory with the Lorentz-Drude dielectric function will not accurately predict experimental results. [27, 28] The projects included in this thesis go beyond Mie theory and the Lorentz-Drude Model to achieve more accurate descriptions of plasmonic phenomenon in real systems.

1.5 Scope of This Thesis

Though a variety of projects are presented in this thesis, each study was aimed at furthering the understanding of physical phenomena fundamentally related to plasmons. The chapters are organized as follows:

The Plasmoelectric Effect

Chapter 2 presents the theoretical framework and experimental evidence for a novel avenue for the conversion of optical power to an electric potential. This plasmoelectric phenomenon of an optically induced electrochemical potential is described in an all-metal geometry and is based on the plasmon resonance in metal nanostructures. Under certain conditions, we predict that when illuminated with monochromatic light off-resonance, plasmonic systems will absorb or expel electrons from an accessible ground to come into resonance

with the incident light and reach a thermodynamically favorable state. We provide experimental evidence for the plasmoelectric effect in arrays of gold nanoparticles on an indium tin oxide substrate, where we observed plasmoelectric surface potentials as large as 100 millivolts under monochromatic illumination of 100 milliwatts per square centimeter. A spectroscopic analysis of Au nanoparticles in solution showed further evidence for the plasmoelectric effect. Plasmoelectric devices may enable the development of all-metal optoelectronic devices that can convert light into electrical energy.

Electrical Tuning of the Dielectric Function and Optical Properties of Nanoparticles

In Chapter 3 we discuss the tunable dielectric response of plasmonic Au nanoparticles under electrochemical bias. We show that the changes in the optical properties of the Au nanoparticles as a function of applied bias can be interpreted in terms of changes in the surface charge density, surface damping, and the near-surface volume fraction of the nanoparticles that experience a modified dielectric function, as well as changes in the index of refraction of the surrounding electrolyte medium. Using experimental bias-dependent extinction measurements, we derive a potential-dependent dielectric function for Au nanoparticles that accounts for changes in the physical properties contributing to optical extinction.

Complete *ab initio* Description of Non-Radiative Plasmon Decay

Chapter 4 describes first-principles calculations that capture all of the significant microscopic mechanisms underlying surface plasmon decay and predict the initial excited carrier distributions so generated. We present the first *ab initio* predictions of phonon-assisted optical excitations in metals, which are critical to bridging the frequency range between resistive losses at low frequencies and direct interband transitions at high frequencies. In the commonly used plasmonic materials, gold, silver, copper, and aluminum, we find that resistive losses compete with phonon-assisted carrier generation below the interband threshold, but hot carrier generation via direct transitions dominates above threshold.

***Ab initio* Description of Hot Electron Relaxation in Plasmonic Metals**

In Chapter 5 we present *ab initio* predictions of the electron-temperature-dependent electronic heat capacities and electron-phonon coupling coefficients of plasmonic metals. We find substantial differences from free-electron

and semi-empirical estimates, especially in noble metals above transient electron temperatures of 2000 K, because of the previously neglected strong dependence of electron-phonon matrix elements on electron energy. We also present first-principles calculations of the electron temperature dependent dielectric response of hot electrons in plasmonic metals, including direct interband and phonon-assisted intraband transitions, facilitating complete *ab initio* predictions of the time-resolved optical probe signatures in ultrafast laser experiments.

Experimental and *ab initio* Ultrafast Carrier Relaxation in Plasmonic Nanoparticles

Chapter 6 presents ultrafast transient absorption measurements and first-principles calculations of the relaxation of hot electrons excited by plasmon decay. We use results from Chapters 5 and 6 to achieve an improved nonlinearized Boltzmann method that fully accounts for the nonthermal character of the excited electron distribution and electronic-structure effects. The model uses our *ab initio* results for the density of states, electron-phonon matrix elements, dielectric function, and electron distribution produced via plasmon decay to replace approximations of these parameters used by previous investigations. Importantly, our model is free of any fitting parameters, which have been relied upon heavily by other studies to achieve agreement between experiment and theory.

Chapter 2

THE PLASMOELECTRIC EFFECT

It is well known that the plasmon resonance frequency, ω_p, of metallic plasmonic materials is dependent on the electron density. Recent work has demonstrated control over ω_p of metal nanostructures when an external electrostatic field alters the carrier density in the metal [29]. Increasing the carrier density in a noble metal nanoparticle results in a blueshift of the resonance, whereas decreasing it results in a redshift, as illustrated for a 20-nm-diameter Ag nanoparticle in vacuum in Figure 2.1. But until recently, the reverse effect, the generation of an electrostatic potential due to an optically driven change in carrier density in a plasmonic nanostructure, had not been observed. Thermodynamically, however, such a effect, coined the plasmoelectric effect, is expected to occur. This chapter first discusses the thermodynamic model which predicts the plasmoelectric effect, and then presents direct experimental evidence of plasmoelectric potentials in the range 10 to 100 mV on colloidal assemblies, in qualitative agreement with a thermodynamic model. These results may provide a new route to convert optical energy into electrical power.

2.1 Charge Dependent Dielectric Function

Our theoretical framework for the plasmoelectric effect requires a model for the dielectric function dependence on electron density, which then determines the material's optical properties dependence on electron density. In this work, we choose to work with two common plasmonic metals, silver and gold. For the dielectric function of Au we use a Brendel-Bormann Gaussian oscillator model, and use the method outlined by Rakic and coworkers [24]. For the dielectric function of Ag we apply a 6th-order multiple oscillator Lorenz-Drude model, fit to data from the Palik Handbook [36]. These dielectric functions accurately reproduce the observed extinction spectra of spherical gold or silver nanoparticles when input into the exact analytic solutions to Maxwell's equations provided by Mie theory [17, 26]. To introduce the explicit dependence on electron density, n, we assume that all terms in the dielectric function that depend on the bulk plasma frequency, ω_p , depend on electron density, n, according to a simple Drude model relation,

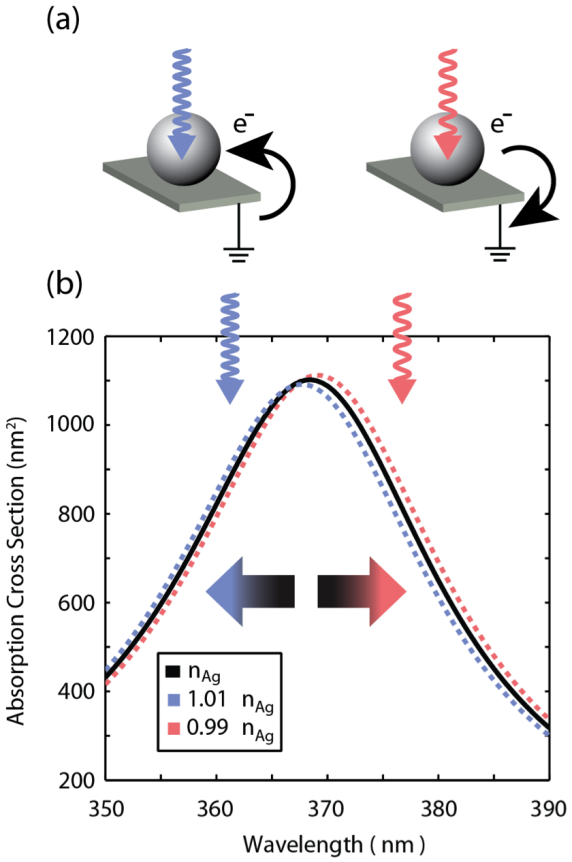

Figure 2.1: (a) Schematic: Spontaneous charge transfer to or from the nanoparticle is thermodynamically favored when the consequent spectral shift increases the absorption, raising the temperature. Irradiation on the blue side of the resonance leads to a negative charge on the particle; irradiation on the red side leads to a positive charge. (b) Calculated absorption cross section for a 20-nm-diameter Ag nanoparticle in vacuum with bulk carrier density n_{Ag} and carrier densities that are reduced or increased by 1%.

$$\omega_p = \left(\frac{ne^2}{\epsilon_o m_e^*} \right)^{1/2} \tag{2.1}$$

where e is the electron charge, ϵ_o is the permittivity of free space, and m_e^* is the electron effective mass [30]. This strategy is consistent with other work that examined carrier density-dependent plasmon shifts, for example in doped semiconductors, electrochemical cells, or at metal surfaces during ultrafast pump-probe measurements [10, 37–39].

Figure 2.2 shows the calculated relative change of the absorption cross section of a 20-nm-diameter Ag nanoparticle in vacuum, calculated with Mie theory, as a func-

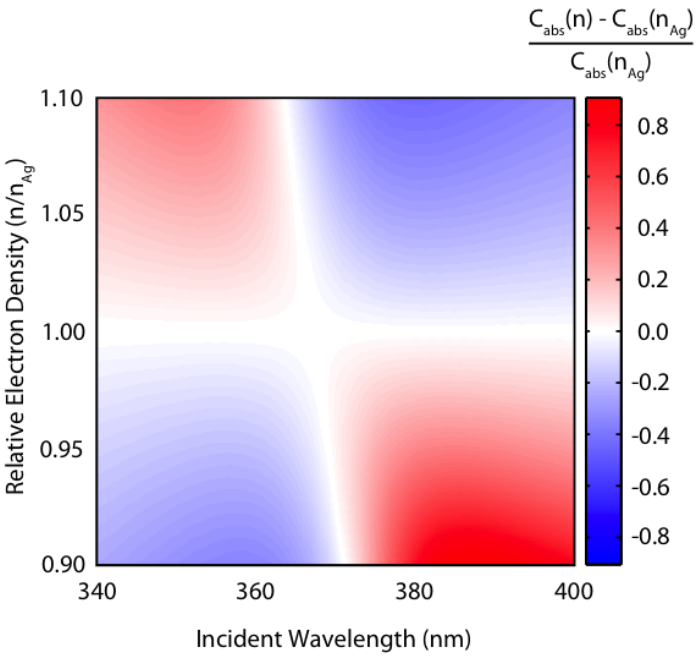

Figure 2.2: Relative change of the absorption cross section, $C_{abs}(n, \lambda)$, of a 20-nm-diameter Ag nanoparticle in vacuum, as a function of wavelength and electron density, and normalized by the absorption cross section for a neutral Ag silver particle with electron density n_{Ag}.

tion of wavelength and electron density, and normalized by the absorption cross section for a neutral Ag silver particle with electron density n_{Ag} [26]. Note that to the blue of the plasmon resonance increasing electron density increases the absorption cross section, and to the red of the plasmon resonance increasing electron density decreases the absorption cross section.

2.2 Thermodynamic Model

Free Energy Minimization

To model the experimentally observed plasmoelectric effect, we consider a metal nanostructure placed on a grounded conducting substrate and illuminated with monochromatic radiation at a wavelength just below the plasmon resonance, λ_p. Random charge fluctuations between particle and substrate will cause the plasmon resonance spectrum to vary by minute amounts (Figure 2.2). If an electron is randomly added to the particle, the resonance will shift toward the blue, leading to an increase in light absorption of the particle, which in turn leads to a small increase in the nanoparticle temperature. The changes in number of electrons N and temperature $T(N)$ change the free energy F of the particle, and an equilibrium charge

density is achieved when the free energy is at a minimum:

$$\frac{\partial F(N,T)}{\partial N} = \left(\frac{\partial F}{\partial N}\right)_T + \left(\frac{\partial F}{\partial T(N)}\right)_N \frac{dT}{dN} = 0 \tag{2.2}$$

Here, we assume that both the intensity and wavelength of the illumination are constant. Using, by definition, the electrochemical potential $\mu(N,T) \equiv (\frac{\partial F}{\partial N})_T$, where μ, and the entropy of the particle $S(N,T) \equiv -(\frac{\partial F}{\partial T})_N$, we find that the free energy minimum corresponds to a configuration with a number of electrons, N, such that

$$\mu(N,T) = S(N,T)\frac{dT(N)}{dN} \tag{2.3}$$

Equation (2.3) shows that under illumination, the plasmonic particle adopts an electrochemical potential that is proportional to dT/dN. This quantity, which is determined only by the plasmon resonance spectrum and the heat flow from the particle to the substrate, provides the unique thermodynamic driving force in the system. It favors charge transfer to or from the particle that increases absorption, and thereby temperature, in order to lower the free energy. The factor dT/dN is largest on the steepest parts of the resonance spectrum; it is positive for irradiation on the blue side of the resonance, leading to a positive chemical potential for the electrons and hence a negative voltage. The reverse is observed for irradiation on the red side of the resonance.

Equation (2.2) can be used to quantitatively estimate the equilibrium plasmoelectric potential by writing $F(N,T)$ as the sum of the free energies of electrons and phonons, using the well-known free energy functions of an electron and phonon gas [40, 41]. The electronic term is composed of a contribution due to the chemical potential of the electrons that is directly given by the Fermi function, and an electrostatic contribution due to charging of the metal nanosphere; the phonon term is given by the Debye model. Taking the derivatives with respect to N and T, we find analytical expressions for $\mu(N,T)$ and $S(N,T)$ (see section 2.2) that are then input into Eq. (2.3).

Our thermodynamic model posits that there is a well-defined, constant temperature, T, of a plasmonic nanoparticle during steady-state illumination at a single wavelength, λ, and intensity, I_λ. This constant T results from the requirement that the optical power absorbed and thermal power conducted away or radiated by the

nanoparticle must be equal in steady state. This temperature is a function of the absorption cross section, C_{abs}, of the nanostructure, which also depends on the electron density, n, due to the strong dependence on n in the complex dielectric function of the metal. Then, $T(n,\lambda)$ is the unique thermodynamic state function that distinguishes an illuminated plasmonic absorber from one in the dark.

We assert that it is reasonable to define such a temperature for a resonantly heated particle, because electronic relaxation processes are fast ($\sim$ 10-100's fs), after which the electronic system and lattice are in equilibrium. We note that similar arguments are central to, for example, the detailed balance calculation of the limiting efficiency of a photovoltaic cell [42]. This well-defined temperature describes a local thermal equilibrium in a thermodynamic system enclosing the particle, and motivates a thermodynamic equilibrium argument based on free energy minimization.

Calculation for the Configuration of Minimum Total Free Energy

We determine the total free energy, F_{tot}, of the nanoparticle by considering the separate contributions from the electrons, F_e, and the phonons, F_p:

$$F_{tot}(N,T(N)) = F_e(N,T(N)) + F_p(T(N)) \tag{2.4}$$

Note that for the optical power densities and time scales we consider, because of the fast electronic relaxation rate and electron-phonon coupling rate in a metal, the electron temperature and phonon temperature are equivalent [17]:

$$T_{electron} \approx T_{phonon} = T(N) \tag{2.5}$$

F_e is defined in terms of the chemical potential of the electrons, μ_e, and the electrostatic potential on the particle, ϕ, as

$$F_e(N,T(N)) = \int_0^N \mu_e(N',T(N'))dN' + \int_0^{N-N_o} \phi(N'-N_o)dN' \tag{2.6}$$

where N_o is the number unbound electrons on the neutral particle, and μ_e is the Fermi function with a small ($< 0.1\%$) temperature correction [40]

$$\mu_e(N,V,T(N,\lambda)) = \epsilon_F(N,V)\left(1 - \frac{1}{3}\left(\frac{\pi k_b T(N,\lambda)}{2\epsilon_F(N,V)}\right)^2\right) \tag{2.7}$$

with

$$\epsilon_F(N,V) = \frac{\hbar}{2m}\left(\frac{3\pi^2 N}{V}\right)^{2/3} \tag{2.8}$$

and ϕ is the electrostatic potential for a conducting sphere:

$$\phi(N - N_o) = \frac{e^2(N - N_o)}{4\pi R\epsilon_0\epsilon_m} \tag{2.9}$$

where R is the sphere radius, e is the electron charge, and ϵ_0 and ϵ_m are the permittivity of free space and the relative permittivity of the surrounding medium, respectively.

F_p is defined in terms of the speed of sound in the particle, v_s, via the Debye temperature, θ, with [41, 43]

$$F_p(T(N)) = 3k_bT(N)A_0 ln\left(\frac{\theta}{T(N)}\right) - k_bT(N)A_0 \tag{2.10}$$

and

$$\theta = \frac{\hbar v_s}{k_b}\left(\frac{6\pi^2 A_0}{V}\right)^{1/3} \tag{2.11}$$

where k_b is Boltzmann's constant, and A_0 the number of atoms in the particle which here is equal to N_o. For Au, $\theta \sim 170K$ [40]. Expression (2.11) is the high-temperature limit of the quantum Debye model, valid for $T > \theta$.

The total electrochemical potential μ and the entropy S can now be derived by applying $\mu \equiv (\frac{\partial F}{\partial N})_T$ and $S \equiv -(\frac{\partial F}{\partial T})_N$ to expression (2.4) for the free energy. We find

$$\mu(N,T(N)) = \epsilon_F(N,V) - \frac{m{k_b}^2T(N)^2}{6\hbar^2}\left(\frac{\pi V}{3N}\right)^{2/3} + \frac{e^2(N - N_0)}{4\pi R\epsilon_0\epsilon_m} \tag{2.12}$$

and

$$S(N,T(N)) = \int_0^N \frac{1}{3}\frac{\pi^2{k_b}^2T(N')}{2\epsilon_F(N')}dN' - 3k_bA_0 ln\left(\frac{\theta}{T(N)}\right) + 4k_bA_0 \tag{2.13}$$

The steady-state charge configuration (value of N) that corresponds to the minimum free energy can then be obtained by using eqs. (2.12) and (2.13) to solve Eq. (2.3). This leads to

$$0 = \epsilon_F(N) - \epsilon_F(N_0) - \frac{m{k_b}^2 T(N)^2}{6\hbar^2}\left(\frac{\pi V}{3N}\right)^{2/3} + \frac{e^2(N-N_0)}{4\pi R\epsilon_0\epsilon_m} - \int_0^N \frac{1}{3}\frac{\pi^2 k_b^2 T(N')}{2\epsilon_F(N')}dN'\frac{dT(N)}{dN} + 3k_b A_0 ln\left(\frac{\theta}{T(N)}\right)\frac{dT(N)}{dN} - 4k_b A_0\frac{dT(N)}{dN} \quad (2.14)$$

This equation can be solved to find the steady-state value for N (for a given λ and I_λ) using as input the function $dT(N)/dN$, which is determined by the plasmon resonance spectrum and the heat conducted or radiated away from the particle.

Theoretical Efficiency Limit

This thermodynamics model shows that an excited plasmonic resonator behaves as a heat engine that can convert absorbed off-resonant optical power into a static electrochemical potential. In principle, optical-to-electrical energy conversion by this mechanism could be optimized to perform with an efficiency at the Carnot limit, as with any generalized heat engine [44].

2.3 Temperature Calculations

Ag Nanoparticle in Vacuum

To calculate the plasmoelectric potential for a Ag nanoparticle in vacuum we calculate the temperature of the nanoparticle, T, given the absorption cross section $C_{abs}(n,\lambda)$ from section 2.1 and incident power density. Under steady state illumination, the power absorbed by the particle must equal the power emitted:

$$P_{in} = P_{out} \quad (2.15)$$

P_{in} constitutes the absorbed monochromatic optical radiation plus the absorbed thermal radiation from the ambient background (at $T_{amb} = 293K$).

$$P_{in} = C_{abs}(n,\lambda)I_\lambda + \sigma A\epsilon T_{amb}^4 \quad (2.16)$$

Here, σ is the Stefan Boltzmann constant, A is the surface area of the nanoparticle, and ϵ is the emissivity. The nanoparticle emissivity $\epsilon = 0.01$ was experimentally determined using FTIR absorption spectroscopy on gold colloids, assuming reciprocity of the absorption and emission in the 2-5 μm wavelength range of the

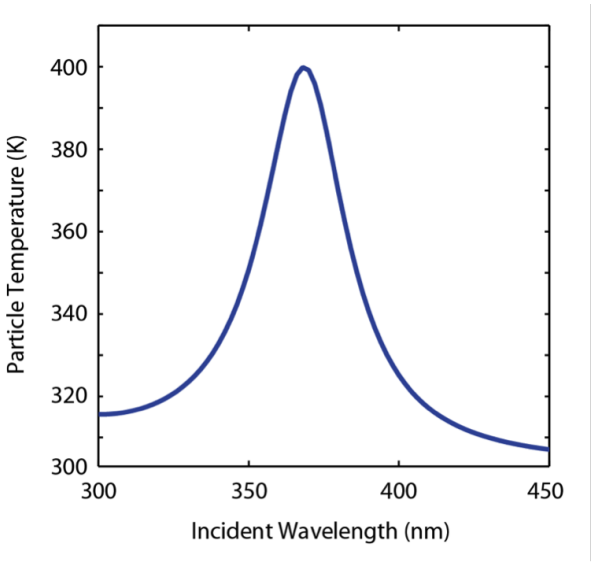

Figure 2.3: Calculated temperature for a 20-nm-diameter Ag particle in vacuum as a function of illumination wavelength (I_λ = 1 mW/cm^2).

measurement (see section 2.6). This value is close to that of bulk gold and silver in the infrared, as reported elsewhere [45] and that predicted by Mie theory. For a Ag nanoparticle in vacuum the only loss channel for the power is thermal radiation, and thus

$$P_{out} = \sigma A \epsilon T^4 \tag{2.17}$$

Solving Equation (2.15) for the temperature of the particle then gives

$$T(n,\lambda) = \left(\frac{C_{abs}(n,\lambda) I_\lambda + \sigma A \epsilon T_{amb}^4}{\sigma A \epsilon} \right)^{1/4} \tag{2.18}$$

Figure 2.3 shows the calculated temperature for a 20-nm-diameter Ag nanoparticle in vacuum as a function of illumination wavelength for an incident power density of 1 mW/cm^2; it peaks at 400 K. The calculated temperature and its dependence on N, $dT(N)/dN$ (for a given λ and I_λ) are then used as input in solving Eqn. (2.14) for the case of a Ag nanoparticle in vacuum (see section 2.4).

Au Nanoparticle on ITO

To calculate the temperature of a Au nanoparticle on ITO/glass we first calculate the absorption cross section spectrum $C_{abs}(n,\lambda)$ using finite-difference-time-domain (FDTD) full wave electromagnetic simulations. In our experiments, described later

in this chapter, the exact dielectric surrounding of the nanoparticle is very complex; there are large variations in inter-particle spacing as well as clusters with different configurations, both inducing near-field coupling and thereby red-shifted resonance wavelengths. Furthermore, Kelvin Probe Force Microscopy (KPFM) experiments were performed in ambient conditions, such that adsorption of water to the particle-ITO interface is likely. Since the exact influence of such conditions on the plasmoelectric potential is beyond the scope of this work, we simplified the geometry to a single 60-nm-diameter Au nanoparticle on an ITO substrate. We assumed a uniform background index of $n = 1.4$ to take into account the red-shift due to the dielectric surrounding described above, such that the modeled scattering spectrum represented the measured scattering spectrum. We then calculated the steady-state power balance to obtain the nanoparticle temperature. Heat flow into the substrate was modeled using a 1D heat transfer model, as sketched in Figure 2.4, with the particle on a glass substrate with thickness $d = 1$ mm covered by a thin layer of ITO. We used the thermal heat conductivity for glass, $\sigma_T = 1.05$ $\mathrm{Wm^{-1}K^{-1}}$ [46]. The heat of the particle can be transferred from the particle (at T_{part}) through a cylinder of glass with cross sectional area equal to the contact area $A_{contact}$ between the glass and the particle, to the bottom of the substrate (at ambient temperature, $T_{amb} = 293$ K). The heat flow is given by [46]

$$P_{diff} = \sigma_T \frac{(T_{part} - T_{amb})}{d} A_{contact} \tag{2.19}$$

Figure 2.4 shows the calculated temperature of the Au nanoparticle as a function of incident wavelength for the three different intensities used in Figure 2.11b. In these calculations the parameter $A_{contact}$ was tuned such that the calculations of the surface potential (see section 2.4) best match the experimentally observed surface potential for the largest power densities. The best fit for the contact area was 2.5 times the geometrical particle cross section, a reasonable value given the simple heat flow model. The same contact area was then used for the lower power densities to calculate the temperature profiles in Figure 2.4 and the surface potentials in Figure 2.4c. We found the same power-dependent trend for slightly more complicated 2D and 3D heat diffusion models, with the assumed contact area between the particle and ITO dominating the magnitude of the temperature. The maximum temperature calculated in Figure 2.4 amounts to 308 K, 15 degrees above ambient temperature, which is a reasonable temperature to sustain for an Au nanoparticle on a substrate. Note that the increase of temperature due to the plasmoelectric effect

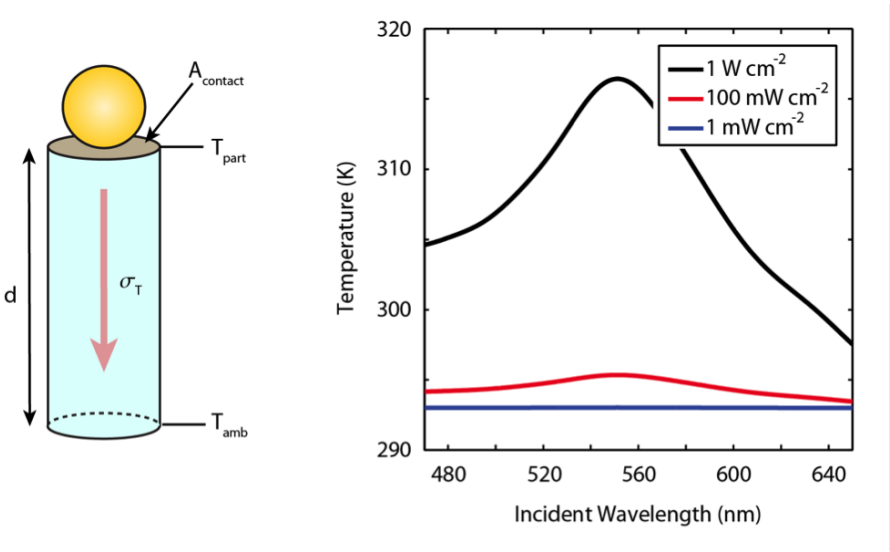

Figure 2.4: (Left) Sketch of 1D heat diffusion model for a Au nanoparticle on ITO/glass. (Right) Au nanoparticle temperature as a function of illumination wavelength, corresponding to the experiments in Figure 2.11b.

compared with a neutral particle is only of order of up to tens of mili-Kelvin, with some variation depending on geometry and illumination intensity. The calculated temperature and its dependence on N, $dT(N)/dN$ (for a given λ and I_λ) were used as input in solving Equation (2.14) for the case of Au nanoparticles on ITO/glass (see section 2.4).

2.4 Calculation of Steady-State Nanoparticle Surface Potential and Charge

Using the temperature and values for $dT(N)/dN$ described in section 2.3 we solved Equation (2.14) to determine the steady-state surface potential and corresponding charge on the nanoparticle as a function of irradiation wavelength. Figure 2.5 shows the calculated charge density change $(N - N_o)$ for Au nanoparticles on ITO/glass, for the highest experimental power density of Figure 2.4b (I_λ=1000 mW/cm^2). The calculations use 6.67×10^6 Au atoms for a 20-nm-diameter Au sphere. As can be seen, the excess electron number $(N - N_o)$ is modulated around a value of -104.69 electrons, observed at the peak of the resonance (where there is no plasmoelectric effect, $dN/dT = 0$). This corresponds to the number of electrons for which the total electrostatic charging energy equals the Fermi energy for Au, $E_F = 5.02$ eV. In the dark, the offset between the Fermi level of the particle and the substrate induces a compensating electrostatic charge on the particle, which is the usual condition for electrochemical equilibration between two dissimilar conductors. Note that the presence of the ITO substrate can be easily accounted for by subtracting the Fermi

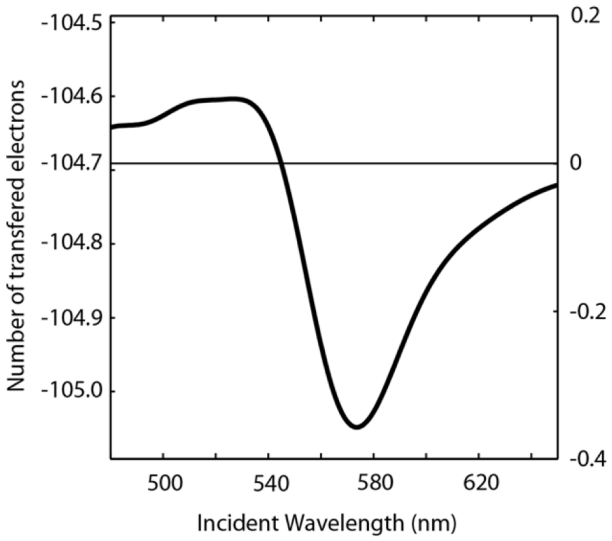

Figure 2.5: Calculated excess electron number $N - N_0$ (right-hand scale) for a 60-nm-diameter Au particle on ITO/glass as a function of illumination wavelength (I_λ = 1000 mW/cm^2). The average number of electrons generating the plasmoelectric effect is shown by the right- hand scale.

energy of the ITO substrate, such that the offset observed in Figure 2.5 is in fact the difference in Fermi energy between the particle and the ITO. Correcting for this "dark" charge (right-hand scale in Figure 2.5), we see that in the time-averaged situation less than one electron on average is added or removed from the nanoparticle to generate the observed plasmoelectric potential. The data in Figure 2.5 can be converted to surface potential, as shown in Figure 2.11c. Additionally, we note that the thermoelectric effect (omitted in our analysis) induces only a minor contribution to the potential state of the particle, even for large temperature gradients between the substrate and particle, because of the small Seebeck coefficient of metals, $\sim \mu V/\Delta K$ [47].

2.5 Charge Accumulation Shell Model

In the calculations described above we assumed that any additional charge carriers that are transferred to the particle are uniformly distributed throughout the nanoparticle. However, electrostatic models require that any surplus charges reside on the surface of a metal object, since no static electric fields can exist inside the metal [48]. On the other hand, the surface plasmon resonance is a dynamic phenomenon, with electromagnetic fields that penetrate into the metal as defined by the electromagnetic skin-depth, which is $\sim$ 1-5 nm for Ag and Au at optical frequencies, and an electron mean free path that is larger than the Fermi screening length. Addition-

ally, the plasmon resonance frequency is predominately determined by the electron density of the portion of the particle within the optical skin depth of the metal, as reported experimentally [27] and verified by us using FDTD simulations. Therefore, electrostatic arguments suggest that any additional charges will reside near the surface of the nanoparticle, and electrodynamic arguments suggest that only the electron density near the surface needs to be increased in order to blue-shift the plasmon resonance. If excess charge resides only near the surface, the plasmoelectric effect thus requires a smaller number of electrons to obtain the same frequency shift, and thereby $dT(N)/dN$ in Equation (2.3) is larger.

To study the influence of non-uniform distributions of charge density in the particle, we consider a simplified shell model, in which we assume that all the additional charge carriers transferred due to the plasmoelectric effect reside in the outer shell with thickness δ (see inset of Figure 2.6). To implement this shell model in Equation (2.14), one has to express the Fermi energy, temperature, and N and V in terms of the number of electrons in the shell volume rather than in the whole particle. Equation (2.14) can then be solved for the number of electrons in the shell, assuming a certain shell thickness.

Figure 2.6 shows the plasmoelectric potential (a) and the relative increase in absorption (b) for a 20-nm-diameter Ag particle in vacuum, as a function of illumination wavelength, with $I_\lambda = 10$ mW/cm^2, and for different shell thicknesses. Figures 2.6 (a) and (b) clearly show the effect of a thinner shell: the transferred electrons induce a relatively larger increase in electron density and thereby a larger increase in absorption. Note that for shell thicknesses larger than 1 nm, the magnitude of the potential rapidly converges to that obtained with uniform charge distribution ($\delta = 10$ nm, green curves). Uniform charge distribution is assumed for calculations throughout this chapter. Further arguments for assuming a uniform distribution of charge include the fact that the area under the absorption spectrum of a dipolar plasmon mode should only scale with the total number of valence electrons in the metal, irrespective of their location inside the particle.

2.6 Nanoparticle Emissivity

We used FTIR absorption spectroscopy to estimate the emissivity of the gold colloids in this study as $\varepsilon \approx 0.01$ (the same order of magnitude as bulk gold), by assuming reciprocity of the absorption and emission in the frequency band of this measurement, between 2-5 μm. This suggests that the IR absorptivity and emis-

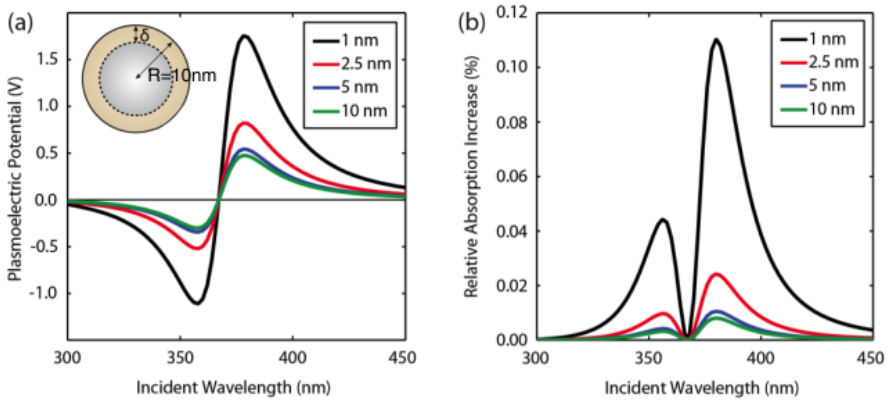

Figure 2.6: Calculated induced potential (a) and relative increase in absorption compared with a neutral particle (b) for a 20-nm-diameter Ag nanoparticle in vacuum as a function of illumination wavelength for shell thicknesses of 1.0, 2.5, 5.0 and 10 nm (black, red, blue and green trace respectively). The illumination power density is 10 mW/cm^2.

sivity of the gold colloids is comparable with bulk gold in the IR, as has been reported elsewhere [45]. Figure 2.7 examines the effect of emissivity on the predicted increase in extinction due to the plasmoelectric effect under monochromatic illumination versus white light illumination (see section 2.10). We find that the difference between the extinction increase for $\varepsilon = 1$ (which represents a perfect black body) and $\varepsilon = 0.01$ (similar to bulk gold) is about one order of magnitude. In the simulations shown in this chapter, we use our experimentally determined emissivity of 0.01.

2.7 FDTD Simulation Methods

We performed full wave modeling using Lumerical finite-difference time-domain (FDTD) [49] simulations to determine the scattering and absorption spectra for Au particles on ITO. Optical constants for Au were, as described in section 2.1, taken from Johnson and Christy [50], and we used the Brendel and Bohrmann model [17] for calculation of the dielectric function. For ITO, optical constants were taken from spectroscopic ellipsometry measurements of sputtered ITO films.

We modeled a 60-nm-diameter Au sphere on top of an ITO slab and a background index of $n = 1.4$ (see section 2.3). The simulations employed Perfectly Matching Layer (PML) boundary conditions on all boundaries. We used a Total Field Scattered Field (TFSF) source to launch and extinguish broadband plane waves (λ =460-650 nm). The scattering and transmission due to the sphere were recorded

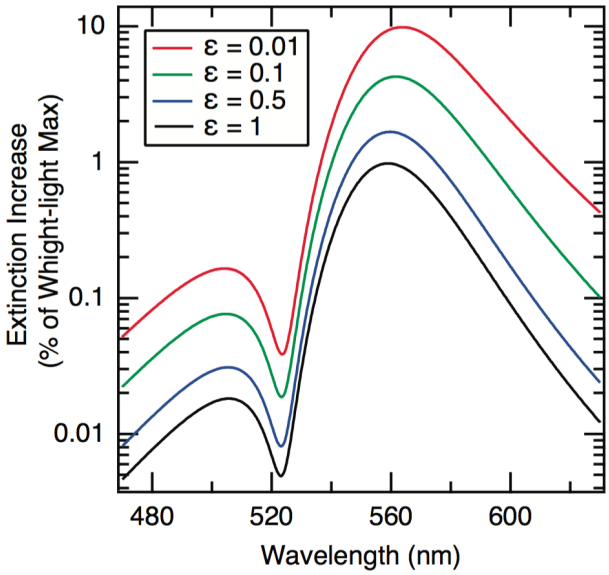

Figure 2.7: Simulated extinction increase compared with white light illumination when Au 60-nm-diameter particles in water are illuminated with 20 mW/cm^2 monochromatic illumination for emissivity values, ε, ranging from 1 (perfect black body) to 0.01 (~bulk gold).

and used to calculate the absorption and extinction spectra.

2.8 Plasmoelectric Simulations

Before applying the model to an experimental geometry (e.g. see Figure 2.11), we first calculated the plasmoelectric potential (i.e., the electrochemical potential gained by the particle from the electron transfer induced by optical absorption) for a spherical 20-nm-diameter Ag nanoparticle in vacuum under monochromatic illumination. For these particles, analytical Mie theory can be used to calculate the absorption cross section spectrum, $C_{abs}(\lambda,n)$, for a given electron density in the nanoparticle by taking into account the dependence of the bulk plasma frequency, ω_p, in the complex dielectric function of the metal on carrier density, $\omega_p \propto n^{1/2}$ (as described in section 2.1). To calculate the nanoparticle temperature, we used a steady-state heat-flow model in which heat is dissipated from the nanoparticle by radiation (see section 2.3). Figure 2.8a shows the calculated plasmoelectric potential of the Ag nanoparticle as a function of illumination wavelength at an incident flux of 1 mW/cm^2, under which the particle obtains a maximum temperature of $\sim 400K$ (see section 2.3). The model predicts a clear negative surface potential below the plasmon resonance and a positive one, up to 150 mV, above it. The asymmetry in the plasmoelectric potential below and above the resonance wavelength is due to

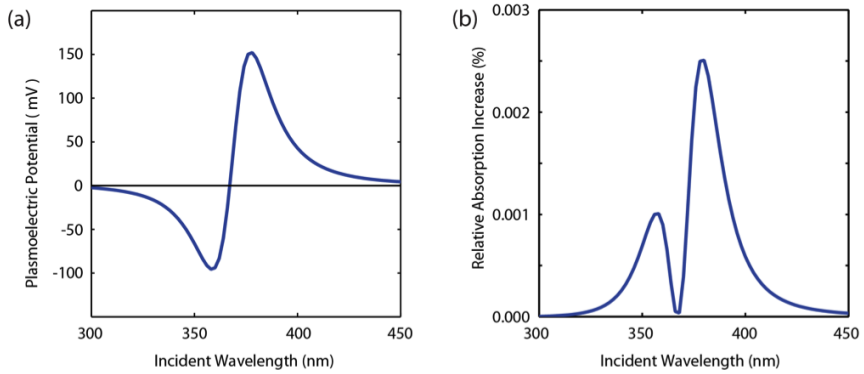

Figure 2.8: A 20-nm-diameter Ag particle in vacuum is illuminated with monochromatic light (I_λ = 1 mW/cm^2). (a) Plasmoelectric potential and (b) relative absorption increase as a function of incident wavelength.

the intrinsic nonresonant interband absorption in the metal. Figure 2.8b shows the corresponding relative absorption increase for the Ag nanoparticle, which ranges up to a factor of 2.5×10^{-5}.

The model for the simple geometry in Figure 2.8 describes the key factors in the plasmoelectric effect: an increase in carrier density under illumination at wavelengths shorter than the resonance peak, inducing a negative plasmoelectric potential and enhanced absorption relative to the neutral particle. Similarly, radiation at longer wavelengths induces a lower carrier density, a positive plasmoelectric potential, and enhanced absorption. These results demonstrate that an excited plasmonic resonator behaves as a heat engine that can convert absorbed off-resonant optical power into a static electrochemical potential.

Next, we used the model to calculate the wavelength-dependent and power-dependent plasmoelectric potential for the experimental geometry in Figure 2.11a, a spherical 60-nm-diameter Au particle on an ITO/glass substrate. We calculated the factor dT/dN in Equation (2.3) using FDTD simulations of the absorption spectra for an Au particle on an ITO/glass substrate to take into account radiative damping from the substrate not captured by simple Mie theory (see section 2.7)and a one-dimensional model for heat conduction into the substrate (see section 2.3). Because of variations in interparticle coupling and clustering (see scanning electron microscopy (SEM) image in Figure 2.11a) and possible adsorption of water onto the particle-ITO interface, the ensemble dielectric environment is complex. The broadened, redshifted scattering spectrum in Figure 2.11a is evidence for some particle aggregation. In the FDTD simulations, we modeled these effects by assuming

a background index of n = 1.4 for the medium above the ITO substrate, such that the absorption spectrum matched the experimentally observed spectrum. As can be seen in Figure 2.11c for the high-power data, the modeled trends correspond well with the experimental trends: the modeled minimum potential occurs at 530 nm (experimental: 500 nm), the modeled zero potential occurs at 545 nm (experimental: 560 nm), and a large positive potential is observed for wavelengths above the resonance, both in model and experiment. The extent of the measured potential to wavelengths up to 640 nm in Figure 2.11b is in agreement with the long-wavelength tail in the spectrum of Figure 2.11a. At 555 nm, the modeled particle temperature peaks at 308 K, 15 K above ambient, in good agreement with other experimental observations [45].

2.9 Kelvin Probe Force Microscopy Experiments

To experimentally probe the plasmoelectric potential, we measured the surface electrostatic potential of films of 60-nm-diameter Au colloid nanoparticles deposited on ITO under optical excitation while varying the wavelength of monochromatic illumination as shown in Figure 2.11. Kelvin probe force microscopy (KPFM) was used to characterize the surface potential. Briefly, a conductive atomic force microscope (AFM) tip employed in non-contact mode determined the static potential difference between the tip and sample surface, indicating the work function difference as well as any trapped charges or other induced potentials at that location. This technique allowed us to measure plasmoelectric potentials induced on the Au particle surfaces as a function of illumination wavelength.

Colloid Desposition

60-nm-diameter Au colloids (BBI International, EM.GC60 Batch #15269, OD1.2) were used for KPFM measurements. Samples for these measurements were prepared on indium tin oxide (ITO) coated glass substrates (SPI brand, 30-60 Ω, 06430, ITO layer thickness: 100 nm) that were first ultrasonicated overnight in a solution containing an equal volume of acetone, methanol, toluene, and isopropyl alcohol and then dried with nitrogen gas. Substrates were placed individually in glass scintillation vials (ITO-side up) with 600 μL Au colloid diluted by 1.2 mL of deionized (DI) water; for control samples, DI water was used instead of the Au colloid solution. Then 60 μL 0.1 M HCl was added, and the vials were immediately centrifuged at 2000 rpm (~670 g-force) for 40 minutes. After centrifuging, the solution had become clear and the ITO film had a noticeable red color due to Au nanoparticles

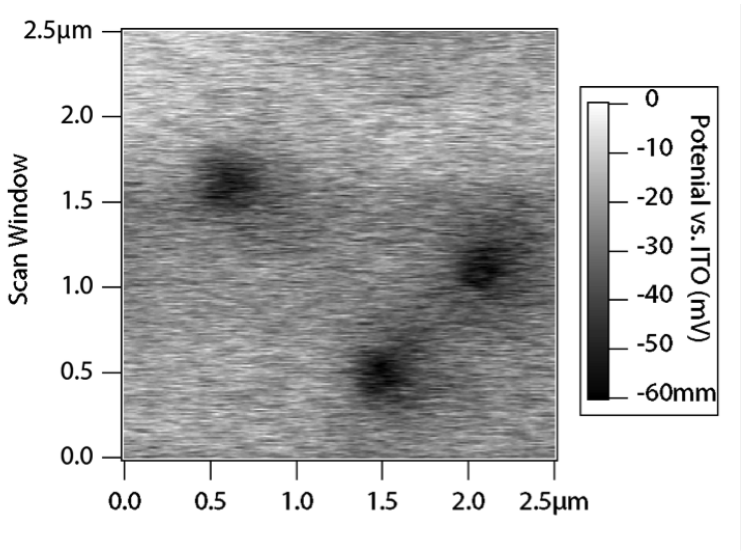

Figure 2.9: KPFM surface potential map of three 60-nm-diameter Au nanoparticles shows the work function offset of Au vs. ITO while the sample was in the dark.

deposited on the surface. Subsequently, the substrates were rinsed thoroughly with DI water and heated to 290 C by placing a heat gun 5 cm above the sample surface for 20 minutes. The scattering spectra of the deposited samples (as in Figure 2.11a) were obtained using a Zeiss Axio Observer inverted microscope equipped with a 20× dark-field objective, with illumination from a halogen lamp. Figure 2.11a shows the measured scattering spectrum for a sample, showing a clear plasmon resonance around λ = 550 nm.

KPFM Measurement Methods

To probe the local static potential difference between the tip and sample surface at room temperature, we used an Asylum Research MFP-3D AFM in scanning Kelvin probe microscopy mode with a n+ silicon conductive tip (Nanosensor ATEC-EFM-20) to measure the surface potential of the ITO-coated glass substrate samples, with the ITO film connected to ground [51]. Figure 2.9 shows that the technique gives mV resolution of the work function difference between Au nanoparticles and ITO, detecting the greater surface electron density of Au compared with ITO when the sample was dark.

Focused optical excitation ($\sim$ 900 μm^2 spot size) adjacent to the AFM tip was provided by a supercontinuum pulsed laser (40 MHz, Fianium SC400-4) that was frequency-selected by an acousto-optic tunable filter (Fianium AOTF) with $\sim$15 nm FWHM bandwidth. During illumination the surface potential in a region of bare

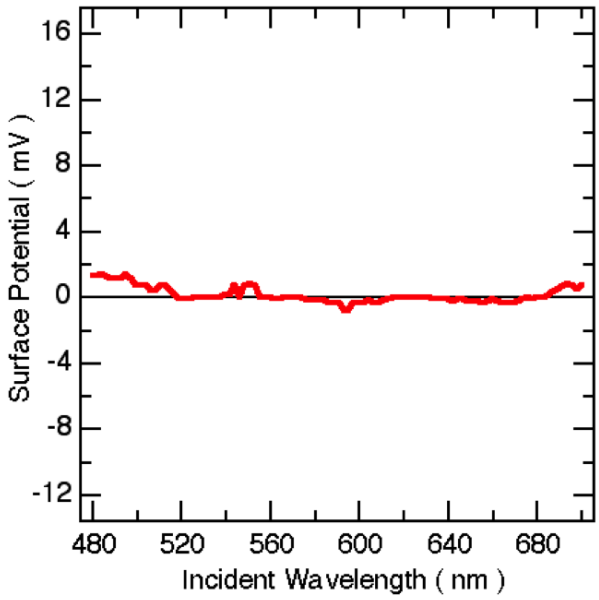

Figure 2.10: KPFM-measured surface potential from a control experiment of bare ITO/glass under 1W/cm^2 scanned monochromatic illumination, plotted on the same scale as Figure 2.11b.

ITO substrate adjacent to the nanoparticle array was compared with the dark signal.

The sample was measured at the limit of highest available particle coverage, and it was anticipated that the measured region of ITO/glass adjacent to the Au particles was equipotential with the particles. Direct illumination of the AFM tip was avoided, and there was no dependence of the magnitude of signal based on the distance from the optical spot, within ~10's of μm. A control measurement of ITO/glass free of Au colloids shown in Fig 2.10 shows no detectable wavelength-dependent signal. The absolute surface potential determined by the KPFM technique is a convolution of the work function difference between the sample and the particular tip used, and factors relating to the tip-sample geometry that define capacitance. Therefore, to emphasize wavelength-dependent changes of potential, the reported data (Figure 2.11b) are plotted relative to the surface potential in the same spot measured in the dark before optical excitation.

Measured Plasmoelectric Potentials

The illumination wavelength was scanned through the plasmon resonance spectrum, from 480 to 650 nm, while we probed the potential of the illuminated Au nanoparticle array. A clear optically-induced surface potential was observed, which varied with illumination wavelength (Figure 2.11b). We observed negative induced po-

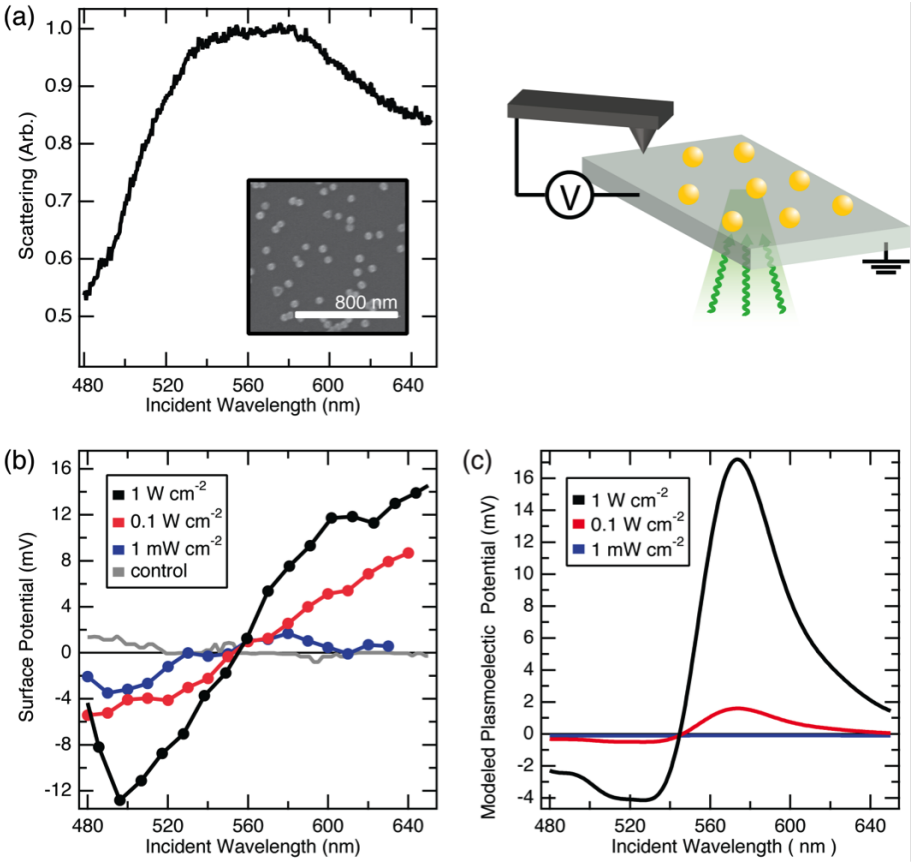

Figure 2.11: Plasmoelectric effect on dense Au nanoparticle arrays on ITO/glass. (a) Dark-field scattering spectrum of 60-nm-diameter Au nanoparticles on ITO/glass. The inset shows a SEM image of the nanoparticle array. (b) KPFM measurements of the surface potential as a function of illumination wavelength (15-nm bandwidth) for three different illumination intensities. The surface potential of a flat region of ITO/glass adjacent to the nanoparticle array was monitored during scanned monochromatic illumination (see schematic geometry). A control measurement of an ITO/glass substrate without nanoparticles (1 W/cm^2) is also plotted (gray). (c) Modeled plasmoelectric potential for 60-nm-diameter Au nanoparticles on ITO/glass for the three illumination intensities in (b).

tentials during excitation to the blue side of the neutral-particle plasmon resonance wavelength near 550 nm, and positive potentials during excitation on the red side of the resonance, with the measured potential changing sign near the peak of the plasmon resonance. The magnitude of the signal increases with increasing optical power density, except at the neutral particle resonance. These data provide evidence for induced plasmoelectric potentials and are consistent with the modeled plasmoelectric response. Notably, these trends are not consistent with the thermoelectric effect. The thermoelectric potential would be maximized at the plasmon resonance, due to the maximal induced heat absorption at that frequency. By contrast, we observe no induced potentials at the plasmon resonance frequency. A thermoelectric potential would also not be expected to change sign based on the wavelength of illumination. Further, even a temperature increase in the particles several hundred Kelvin greater than predicted by our model would induce thermoelectric potentials of only a few hundred μV based on the Seebeck coefficient of bulk Au [47]. This small voltage is below the limit of our measurement sensitivity. However, some offset in the data may be due to the thermoelectric response of the substrate. Control samples of ITO with no Au particles show a weak constant positive potential, ~ 1 mV, during wavelength scans at high optical intensity. Direct illumination of the AFM tip was avoided during measurements.

For comparison, the modeled plasmoelectric response from an individual 60 nm Au particle in this geometry, as described in section 2.8, is displayed (Figure 2.11c). The deviation of the measured surface potential trend as compared to the modeled curves may result from several factors. The KPFM measurement is a non-contact technique, with the conductive AFM tip nominally 300 nm from the sample during our experiments. Therefore the modeled curves (Figure 2.11c) assume the electrostatic potential from the particle decays inversely with distance, exhibiting the potential profile of a charged sphere at the separation distance of the KPFM tip. However, details of the local geometry will strongly determine the magnitude of the measured signal. Further, if the nanoparticles reach a higher or lower temperature than our model anticipates, the plasmoelectric voltage will be proportionally affected. The spectral broadening at longer wavelengths observed in the optical signal (Figure 2.11a), which may be due to particle aggregation during deposition, will also reduce the plasmoelectric response, similar to the effect of particle size polydispersity in Figure 2.13. This contribution may also account for the greater symmetry observed in the magnitude of the negative and positive potentials compared with the theoretical curves, as spectral broadening towards longer

wavelengths would more significantly decrease positive plasmoelectric potentials. Circuit non-idealities, such as contact resistance between the Au and ITO, may also contribute to a reduction in the plasmoelectric potential. In our studies it was necessary to anneal samples for more robust signal, presumably to remove residual surface ligands from the Au colloid, reducing the contact resistance.

2.10 Optical Measurements of Nanoparticles Under Monochromatic Illumination

The plasmoelectic model predicts that when illuminated to either side of the plasmon resonance with monochromatic radiation, the charge density of a plasmonic resonator in contact with a electron reservoir will change such that the absorption cross section will shift towards the illumination wavelength. It follows that the spectra of Au colloids measured with scanned monochromatic light will show a broader resonance peak than the resonance peak in a spectra measured with white light. We performed optical extinction spectroscopy for 60-nm-diameter Au colloids in water to characterize this plasmoelectric response. The changes in the surface charge density of the particles can result from induced polarization across the metal-water interface.

Experimental Setup

To measure the extinction of 60-nm-diameter Au colloids (BBI International, EM.GC60 Batch #15269, OD1.2) in water under broadband (white) and monochromatic illumination, we used lock-in amplifiers (LIA) in combination with two photodiode power meters and a monochromator. The measurements setup is shown in Figure 2.12. For broadband illumination, the cuvette with Au colloids was positioned in front of the monochromator (sample position 1). For the monochromatic illumination conditions, the cuvette was placed in between the two photodiodes. The extinction can easily be obtained by comparing the signal on both power meters for each illumination wavelength and normalizing by spectra of a cuvette with DI water placed in the same two positions as the sample.

Measured Spectral Dependence on Illumination Properties

We compare extinction measurements under white light and monochromatic excitation conditions. As noted above, scanned monochromatic illumination leads to increased optical extinction when a plasmoelectric potential is manifest as compared with the extinction of neutral particles. In contrast, if a particle is excited

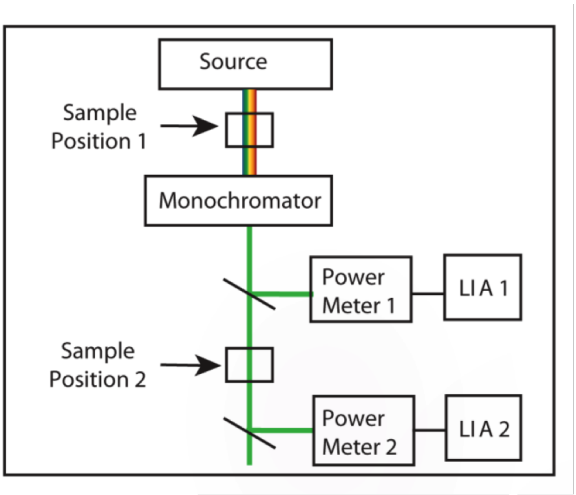

Figure 2.12: Schematic of white vs. monochromatic illumination experimental setup

with broadband ('white light') illumination, so that the excitation power density per unit spectral interval is equivalent both at higher and lower frequencies relative to the plasmon absorption maximum, then there is no thermodynamic driving force for the plasmoelectric effect, so no spectral shift is expected and the particle will remain neutral. Figure 2.13a shows the measured optical extinction spectra of Au colloids during both white light (black curve) and scanned monochromatic excitation (red curve), both with intensities of 20 mW/cm^2. A small, but clearly distinguishable difference in extinction is observed on both sides of the spectrum. Figure 2.13b shows the relative extinction change, derived for the data in Figure 2.13a; data for illumination at 0.2 and 2.0 mW/cm^2 are also shown. A systematic increase of the spectrally-integrated extinction is observed during monochromatic illumination when compared with spectra obtained during white light illumination. The observed wavelength-dependence is in good agreement with the modeled plasmoelectric response trends shown in Figure 2.13c (see section 2.10). Specifically, the minimum increase of extinction is correlated with the extinction maximum at the plasmon resonance near 530 nm. Moreover, the asymmetric absorption increase when comparing each side of the extinction maximum, which is characteristic of the non-plasmonic interband absorption in Au, as described above, is clearly reproduced in the measurement, providing further evidence of induced plasmoelectric potentials during scanned monochromatic illumination.

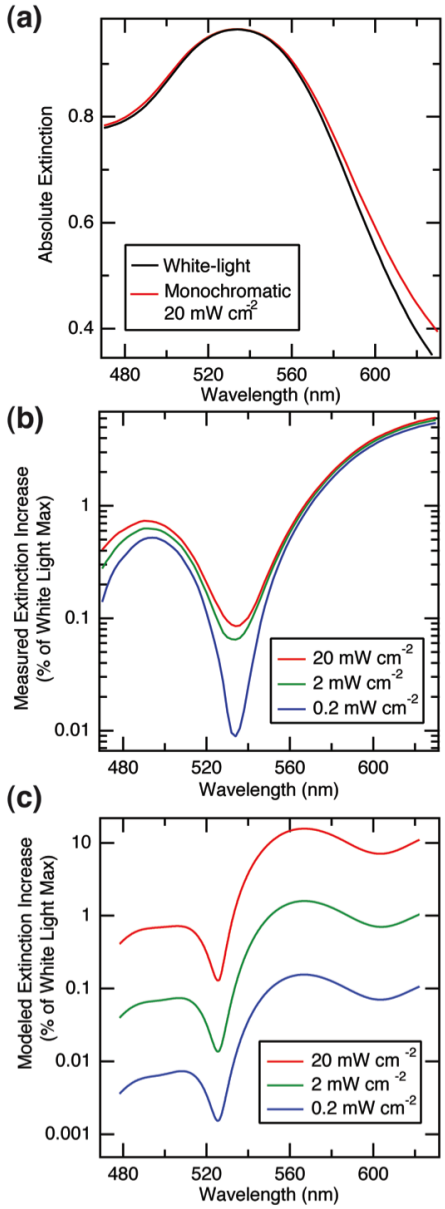

Figure 2.13: Plasmoelectric effect for 60 nm Au colloids suspended in water: (a) Measured extinction spectra for broadband (black curve) and monochromatic (red curve) illumination (both 20 mW/cm^2). (b) Relative increase in extinction for monochromatic illumination derived from the data in (a). Data for 0.2 and 2.0 mW/cm^2 are also shown. (c) Modeled increase in extinction for same fluxes as in (b).

Modeled Optical Plasmoelectric Response

To model the increase in extinction during monochromatic illumination in a water environment, we calculate the thermal energy of the system in diffusion-limited conditions (i.e. particles are in thermal equilibrium with the water) that correspond with the experimental procedure. Assuming that the water in the cuvette is a thermally isolated system, all the power absorbed by the nanoparticle suspension will heat the water (thermal radiation is negligible), and the system will increase its temperature. Using the laser power ($\sim$ 1 mW max), scan speed (1 nm/s), the extinction (measured, see Figure 2.13a), the fraction of extinction that goes into absorption (known from Mie theory), the heat capacity of water, and the volume of water in the cuvette, we calculate that the temperature increase during monochromatic illumination is $\sim$1 mK per second at the highest illumination intensity in our study. We then calculate the thermal energy of a volume of water heated per particle under illumination. Given the particle concentration of the suspension (2.6×10^{10} mL^{-1}), this corresponds to a maximum $\sim$ 1.6×10^{-13} J of thermal energy provided per particle. To solve the governing relation Equation (2.7), the change of this thermal energy per change of surface charge density on the particle (due to changes of absorption) is equated to the change of electrochemical potential. Full wave simulations (FDTD method) were used to calculate the extinction based on the charge density that satisfied Equation (2.7) at each incident wavelength and power, and is depicted in Figure 2.13c.

Our calculations also account for the influence of the colloid polydispersity on the plasmoelectric response, assuming an ensemble of particles with a size distribution that is typical for high-quality Au colloids used in this study (8% coefficient of variation). Relative to a monodisperse colloid or individual particles, polydispersity increases the absorption at all incident wavelengths. For excitation at the ensemble absorption maximum, some fraction of particles larger or smaller than the average size can change surface charge density to enhance absorption. We note that the sub-linear increase of the experimentally measured changes in extinction with incident power (Figure 2.13b) as compared to the modeled linear increase with incident power (Figure 2.13c) suggests an intensity-dependent dissipation mechanism not accounted for by our simple thermal analysis, despite otherwise good agreement with the modeled trend and relative magnitude of the wavelength-dependent response.

2.11 Conclusions

To aid interpretation of our findings, we comment briefly on other mechanisms for generating photopotentials in metals. A thermoelectric effect is several orders of magnitude weaker ($\sim \mu$V/K) than the observed potentials as discussed above [47]. Hot carrier-induced effects would require rectifying contacts, which are not present in our geometry. Moreover, both of these effects would not result in a bisignated signal [18]. "Plasmon drag" or similar direct photon-to-electron momentum transfer mechanisms on Au colloids would not produce a bisignated signal [52]. Future work in this area will benefit from further insight into the microscopic mechanisms that contribute to the observed effect.

The observed plasmoelectric phenomenon takes advantage of the remarkable spectral tailorability of plasmonic nanostructures and can be extended to a variety of material systems, absorber geometries, and radiation environments. Plasmoelectric devices may enable the development of entirely new types of all-metal optoelectronic devices that can convert light into electrical energy by replacing the usual function of doped semiconductors with metal nanostructures that are optically excited off-resonance.

Chapter 3

ELECTRICAL TUNING OF THE DIELECTRIC FUNCTION AND OPTICAL PROPERTIES OF NANOPARTICLES

3.1 Previous Work and Overview

The plasmonic response of metal nanoparticles has generated great scientific interest, motivating both fundamental investigations and exploration of a variety of applications, such as photovoltaic cells [13], photocatalytic fuel cells [30, 53] surface enhanced Raman Spectroscopy (SERS), [54–57] cell labeling, and molecular sensing [27, 28, 56, 58–60]. These complex environments modify the plasmonic behavior in several ways due to the material dynamic response under electrochemical potential changes, by the equilibration of the particle with the surrounding Fermi-level offset, and the effects of chemical reactivity, solvent polarizability, and interface damping [29, 61–67]. In order to achieve precise manipulation of the properties of metallic resonators in tunable plasmonic systems, we are fundamentally interested in how changes of charge density and the properties of the surrounding environment, such as refractive index and electronic surface states, affect the plasmonic absorption. The Drude model can be used as a first approximation to predict how a change in charge density produced by an applied bias tunes the plasmonic resonance [27, 30, 60, 68]. However, it is well known that plasmon resonances are dependent on their environment, [13, 26, 54, 56, 57, 64, 69] and a simple Drude model omits a description of property changes other than a uniform change in charge density. The Drude model does not take into account other effects that happen in parallel with changes in charge density in a real system, such as changes in electronic surface states due to chemical interactions with the surrounding medium and the resultant changes in damping and index of refraction (e.g. adsorbates, oxidation, electric double layer) [27, 28, 56, 59, 60, 64, 67, 70]. Furthermore, using a Drude model to represent a uniform change in charge density in a plasmonic structure does not account for the excess charge residing at the conductor surface. Thus, in order to predict optoelectronic behavior of plasmonic systems, we desire a model that will account not only for changes in charge density, but also for changes in damping, index of refraction, and penetration depth of surface charge and damping. This will allow us to assess the relative spectral contributions of each effect, and how they act in concert in an electrically tuned plasmonic system. Better quantification of

the various contributions that shape plasmonic resonances is crucial for current research in tunable plasmonics, and more broadly, for any system in which plasmonic elements will be used an a non-neutral state, e.g. as catalysts or electrical contacts.

Previous experiments have shown that externally biased Au nanoparticles (AuNPs) are not adequately described by the Drude model [17, 26, 27, 60, 64, 68, 71]. A potential-dependent modified dielectric function and T-matrix-based fitting routine has been proposed to analyze interface damping and uniform charging effects for Au nanorods in an electrochemical cell [68]. This work provided a systematic model for bias-dependent extinction, but did not explicitly address index changes in the surrounding media or non-uniform distribution of charge at the particle surface [68, 72]. Separately, the effects of various surface layers on the dielectric response of Au nanoparticles in an electrochemical cell were investigated, in comparison with modeling that relied on analytical Mie Theory, though analysis of broadening effects and the role of the refractive index of the substrate were not considered [24, 27, 72]. These researchers found evidence of increased damping at a positive applied bias, which they attributed to a lossy layer at the particle surface. Previous research has not analyzed the effects of changes in the surrounding dielectric environment, changes in damping, and concentration of excess charge at the particle surface all occurring in unison. In this Chapter, we present mechanisms for bias-dependent optical extinction of Au nanoparticles, using full wave electromagnetic simulations in conjunction with experimental optical spectra to characterize the response of arrays of colloidal Au nanoparticles immobilized on indium tin oxide (ITO) substrates in an electrochemical cell. Through this combined simulation and experimental approach, we account for the influence of refractive index due to the substrate, index changes in the near-surface environment of the nanoparticle, and a variable-thickness shell of modified damping and charge density at the surface of the gold nanoparticle (AuNP). We compare the simulations with experimental results to quantitatively analyze the contributions from these effects.

3.2 Electrochemical Cell Fabrication

ITO coated glass substrates (SPI brand, 30-60 Ω, 06430) were used as the top and bottom electrodes in the electrochemical cell (Figure 3.1). The substrates were cleaned by ultrasonicating overnight in a solution containing equal volume of acetone, methanol, toluene, and isopropyl alcohol and then dried with nitrogen gas. Parafilm wax was used to cover one half of the bottom electrode ITO slide to prevent Au colloid deposition in the subsequent step, thereby reserving

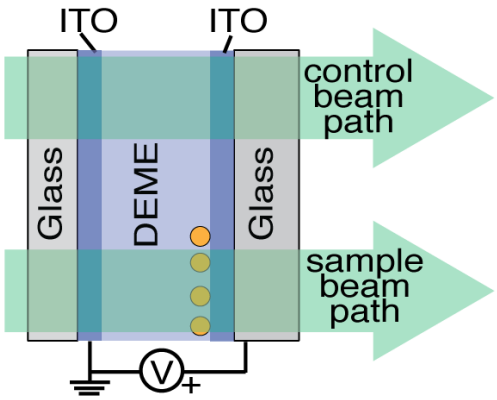

Figure 3.1: Geometry of electrochemical cell with 60-nm-diameter AuNPs on the bottom electrode. The top electrode is grounded, and potentials are applied to the bottom electrode. An optical beam passes through the cell for spectral measurements

half of the bottom electrode for use as a control in the normalization of optical spectra; this allowed us to carefully control for a possible optical response from the ITO substrate as a function of applied bias. The bottom electrode was placed in a glass scintillation vial (ITO-side up) with 300 μL of 60-nm-diameter Au colloids in water (BBI International, EM.GC60 Batch #16516 OD1.2) and 1.5 mL of deionized (DI) water. 60 μL 0.1 M HCl was added to the vial, and the vial was immediately centrifuged at 2000 rpm (~670 g-force) for 40 minutes. After centrifuging, the Au colloid solution had become clear and the bottom ITO electrode has a noticeable red color due to Au nanoparticles deposited on the surface. The Parafilm wax was removed from the bottom electrode and the electrode was rinsed thoroughly with DI water then soaked in toluene for one hour to remove residue from the Parafilm wax. Both electrodes were plasma etched with a direct plasma at 110 W and 300 mTorr O_2 for 20 minutes to remove ligands and any organic mater from the AuNPs and ITO surface. Substrates were then vacuum annealed at 350 C for 20 minutes. The two electrodes were mounted face-to-face with two pieces of Teflon tape used as a spacer between the slides at the slide edges. Under inert atmosphere, Diethylmethyl(2- methoxyethyl)ammonium bis(trifluoromethylsulfonyl)imide (DEME) electrolyte (Sigma Aldrich, 727679) was used to fill the space between the slides and the cell edges were sealed with 5-minute-setting epoxy to prevent water moisture and oxygen from entering the cell.

3.3 Optical Measurements of Nanoparticles Under Applied Bias

Experimental Setup and Procedures

In our experiment, the spectra of an ensemble of 60-nm-diameter Au colloids in an electrochemical cell were recorded as a function of applied bias. The applied bias was swept from 0V to 2.25V and then to -2.25V and back to 0V in 0.25V steps. The top electrode was grounded and potentials were applied to the bottom electrode using a DC voltage source (Tektronix PS282).

The extinction spectra of an array of AuNPs in the electrochemical cell were obtained using a spectral response and lock-in amplifier technique. The beam from a supercontinuum pulsed laser (20 MHz, Fianium SC400-2) was chopped at 100 Hz and directed into a monochromator (Oriel 777000) that was optically in-series with two Si photodiodes (the first photodiode was used as a reference). The spectral resolution of the monochromator was approximately 1.5 nm. The photodiode signals were passed through transimpedance amplifiers (DL Instruments 564) and were detected by lock-in amplifiers (SR830 DSP). Spectra with the optical beam passing through the portions of the bottom electrode with and without Au colloids were collected at each applied bias step. The spectra taken in the portion of the bottom electrode without Au colloids were used as normalization spectra. Approximately 20 minutes elapsed between each voltage step and the corresponding spectral measurement.

Optical Measurement Results

Figure 3.2(a) shows the extinction spectra for AuNPs in the electrochemical cell at selected values of applied bias, which were smoothed with a Savitsky-Golay filter. A red-shift of the peak is observed at positive applied bias and a blue-shift and increase in peak height is observed under negative applied bias. The shift of the peak is more evident in the extinction change spectra (Figure 3.2b) where a red-shift is manifest as a positive change in extinction to the red of the peak and a negative change in extinction to the blue of the peak, and vice versa for a blue-shift. Figure 3.3 shows the change of the spectral properties as a function of applied bias. Over the range of applied potentials, the wavelength of peak extinction shifted by 3nm and the full width half maximum of the peak varied by 4nm (Figure 3.3 a & c). The total peak extinction change was 7% of the initial 0V peak extinction (Figure 3.3b). The hysteresis in the experimental results indicated some nonreversible process and that this electrochemical system did not exhibit ideal reversible charging. Additionally, we found that at negative applied potentials, the peak height increased.

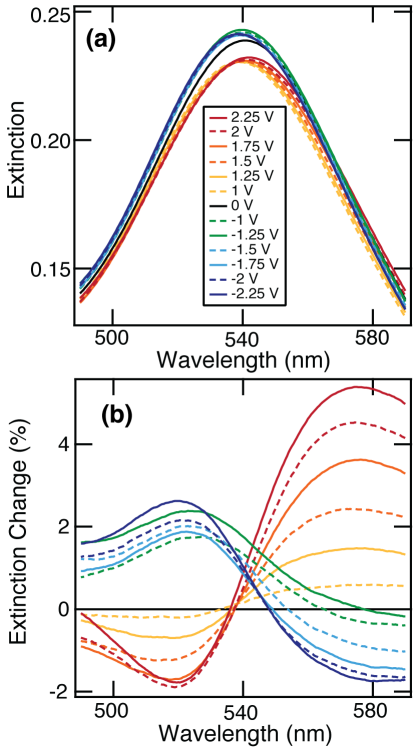

Figure 3.2: (a) Extinction versus wavelength at selected applied potentials as indicated by line color. (b) Extinction change versus wavelength at the same applied potentials in (a).

This is in contrast to what we would expect based on the Drude model and Mie theory [17, 24, 26], which predict a peak height change that decreases monotonically as a function of increasing electron density. This suggests that, at the very least, there was significant damping in the experimental system at positive potentials that is not captured by a Drude and Mie theory model.

Raw Spectra and Noise Level

Below we provide spectra of the particles in the electrochemical cell with no smoothing (Figure 3.4). These spectra have been normalized by the spectra taken in the part of the electrochemical cell with no particles to account for contributions from the substrate or other scatterers in the system. Part (a) shows the spectra over the same wavelength range as that in Figure 3.2. Part (b) shows the spectra over the entire measured wavelength range. As can been seen in the figures, there is very little noise. The signal to noise ratio was roughly 400:1.

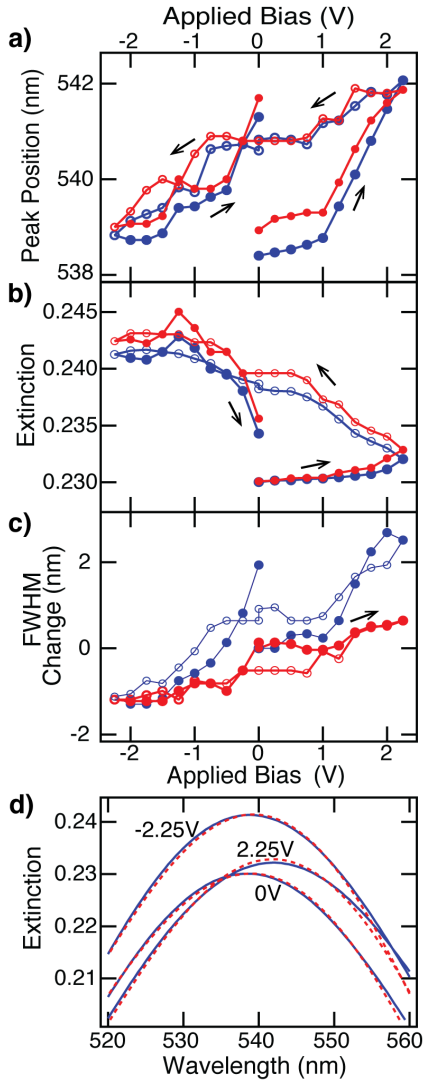

Figure 3.3: Experimental results are displayed in blue; simulation results are displayed in red. (a) Peak position (b) peak extinction, and (c) full with half max change relative to the first 0V applied bias point versus applied bias. For a-c, the markers for the applied bias points for the middle portion of the cycle, from 2V to -2.25V in -0.25V steps are hollow. (d) Experimental extinction spectra at 0V, +2.25V and -2.25V and their best-fit simulated spectra.

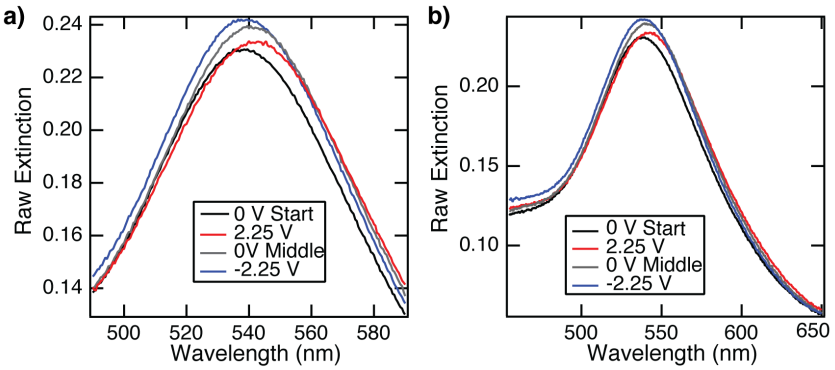

Figure 3.4: Normalized raw spectra at the extremes of the applied bias cycle (2.25V and -2.25V) as well as the first 0V point (0V Start) and the 0V point in the middle of the applied bias cycle (0V Middle).

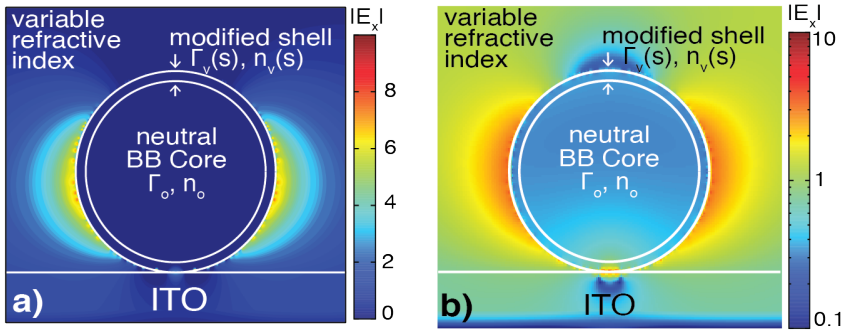

Figure 3.5: Full wave FDTD simulation, x-component of the electric field in a y-normal cross-section. The 60-nm-diameter particle is modeled by a neutral core defined by the BB model and a shell with a modified dielectric that allows for variations in damping and charge density at the surface. The substrate is defined by measured n and k data and the electrolyte is modeled as a uniform dielectric above the substrate. The varied simulation parameters are shell charge density, shell damping, shell thickness, and the refractive index of the electrolyte. (a) Uses a linear color scale to show the dominant dipole field, and (b) uses a log color scale to show fields extending into the particle and ITO substrate.

3.4 Modeling Optoelectronic Effects with FDTD Simulations

Three-dimensional full wave electromagnetic simulations were performed using finite difference time domain methods to model and analyze the experimental system. The simulation geometry consisted of a 60-nm-diameter Au nanosphere on an ITO substrate and in a surrounding medium with uniform index of refraction (Figure 3.5). The ITO substrate was defined by the real and imaginary part of the complex index of refraction, measured with ellipsometry. The AuNP was simulated as a core defined by the Brendel and Bormann (BB) [56, 57, 72, 73] dielectric function with the additional feature of a variable-thickness shell with a modified dielectric function. The BB model uses a superposition of an infinite number of oscillators (termed a BB oscillator) to replace the single Lorentz oscillator used in the Lorentz-Drude model [24, 60, 72, 74]. The BB dielectric function is defined as:

$$\epsilon_{BB}(\omega) = 1 - \frac{\omega_p^2}{\omega(\omega - i\Gamma_o) + \sum_{j=1}^{k} \chi_j(\omega)} \tag{3.1a}$$

$$\omega_p = \sqrt{\frac{n_o e^2}{\epsilon_o m_e}} \tag{3.1b}$$

where Γ_o is the damping constant of bulk gold, $\chi_j(\omega)$ is a BB oscillator, ω_p is the plasma frequency in the Drude model, n_o is the electron density of bulk gold, e is the elementary charge, and m_e is the effective electron mass. Six BB oscillators were used in our parameterization. We obtain an analytic function that satisfies the Kramers-Kronig reciprocity relations for real and imaginary components of the dielectric function. This model has been shown to accurately model the optical properties of gold in the wavelength range relevant to this study [24, 28, 75–78].

Voltage-dependent Dielectric Function

A modified dielectric function at the surface of the particle was used to model changes in the electronic states and population near the surface:

$$\epsilon_{shell}(\omega, s) = 1 - \frac{\omega_{p,v}(s)^2}{\omega\left(\omega - i\left(\Gamma_o + \Gamma_V(s)\right)\right) + \sum_{j=1}^{k} \chi_j(\omega)} \tag{3.2a}$$

$$\omega_{p,V}(s) = \sqrt{\frac{n(s)e^2}{\epsilon_o m_e}} \tag{3.2b}$$

Here, $\omega_{p,V}(s)$ and $n(s)$ are state (s) dependent variables, where the state describes the applied bias (V) applied to the cell and the microscopic state of the system, and these state-dependent variables have replaced the respective constant values used in the BB model. An additional, state-dependent damping term $\Gamma_V(s)$ was added to the bulk damping to allow for changes for damping at the particle surface as a function of the state of the system (largely the applied bias).

Parameter Sweeps and FDTD Simulations

The independent parameters that were varied in our analysis are: the index of surrounding electrolyte, and Γ_V and $n(s)$ in the shell dielectric function, as well as the thickness of this shell. Additionally, to account for polydispersity in the size of particles (8% coefficient of variation as reported by the supplier), we performed electromagnetic simulations for particles with 28, 30, and 32 nm radii and took a weighted average of the resulting spectra to produce simulated extinction spectra for polydisperse samples for each parameter set (surrounding-index, Γ_V, $n(s)$, and shell-thickness). We performed calculations where each of these parameters was varied independently. For each unique parameter set, a full-wave electromagnetic simulation was performed with Lumerical FDTD Solutions software to simulate the extinction spectra corresponding to that parameter set. This approach allowed us to calculate a set of predicted extinction spectra from the effect of changes in index, interface damping changes, and surface charging occurring in parallel. We began with broad parameter sweeps where the values for parameters found in current literature describing damping, surface effects, charging, or electric double layer were well within the sweep limits [24, 27, 28, 71, 75]. The limits for the parameter sweeps are shown in Table 3.1.

Next, we preformed an iterative process for finding the values of parameters that produced simulated extinction spectra with smallest root mean square error (RMSE) in comparison to the Savitsky-Golay smoothed experimental extinction spectra. After each parameter sweep, new parameter sweeps with finer resolution of the parameter space around the parameter values that had produced the lowest error were preformed. This iterative processes was preformed until an acceptable resolution (shown in the Table 3.1) was reached for all parameters and at this point, the parameter set with the smallest RMSE overall was selected as the champion set. Using this iterative process, we determined the parameter values that most closely reproduced the experimental spectra at each applied bias and achieved RMSE errors below 1%. This process was carried out for each applied bias and thus resulted in one

champion set of parameters for each applied bias step. The champion parameters values for these simulations then represented the identifiable physical properties and changes in the system as determined by our model. These parameters are those shown in Figure 3.6.

Physical Interpretation of Simulation Parameters

We believe the model described above represents the most comprehensive analysis to date of the microscopic mechanisms that can contribute to bias-dependent optical extinction for metal nanoparticles. We now discuss the physical basis for the observed variation of nanoparticle parameters. Because gold oxide has a larger dielectric constant than the electrolyte solution, oxidation of the AuNP surface will cause changes of the index of refraction at the surface of the metal nanoparticle relative to an unoxidized Au particle [28, 56, 57, 73, 79]. Further, the refractive index of the surrounding medium could also change due to alignment of dipoles in the electrolyte, as in an electric double layer [60, 64, 67, 70, 71, 74]. Damping may also be modified by an applied bias because of variations of population or depopulation of electronic surface states at the AuNP surface [28, 75–78]. For example, an applied bias could facilitate enhanced chemical reactivity and adsorption at the particle surface and electrons may become trapped in empty adsorbate states, causing an increase in damping[28, 79]. Alternatively, an increase in electron density due to a negative applied bias could result in electron spill-out from the surface and repulsion of solvent molecules from the AuNP surface [53, 80, 81]. This could conceivably give rise to a decreased damping due to a decrease in chemical reactivity and trap state occupation at the particle surface. It is also reasonable to assume that the applied bias will alter the total number of electrons in the AuNP and thereby alter the plasma frequency in accordance with the Drude model [29, 65]. In the electrostatic limit, mobile charges will rearrange to minimize the electric fields in the bulk of a conducting particle, so we assume that excess electrons or holes reside near the particle surface. Finally, the modified electronic states and electron density

Table 3.1: Simulation parameter limits and resolution

Parameter	Lower Limit	Upper Limit	Finest Resolution
Surrounding Index	1.0	1.7	0.001
Shell Charge (n/n_{Au} %)	0.95	1.05	0.005
Shell Thickness (nm)	0	5	0.25
Damping (rad/sec)	0	3e14	2.5e11

at the surface may have a variable penetration depth that depends on the applied bias because of the aforementioned electron spill-out, adsorbate states, and the optical versus the static skin depth of excess charge residing near the surface. We account for changes in the penetration depth of altered electronic states by varying the thickness of the modified dielectric shell in our simulations.

3.5 Comparison of Simulation and Experimental Results

By varying the charging, damping, shell thickness, and electrolyte index independently of one another in our parametric calculations and by computing their net influence on the extinction spectra, we were able to closely model the experimental changes in the extinction as a function of applied bias with full wave electromagnetic simulations. Figure 3.3 shows a comparison of the spectral properties of the simulated and experimental spectra. We see that the best-fit simulations closely track the peak position, height and changes in width. Furthermore, in Figure 3.3d, we show the experimental and best-fit simulated spectra at the extrema of the applied bias range (2.25V and -2.25V) as well as at the first 0V applied bias point, with very good agreement between the curves. We note that the absolute FWHM is sensitive to peak broadening due to particle size polydisparity and other ensemble effects[29, 71] that are not well captured by our FDTD simulations, though changes of FWHM (Figure 3.3c) are primarily due to changes in damping, and therefore are expected to be tracked well by our analysis method. From Figure 3.6a we note that the maximum RMSE of the fits of the simulated and experimental spectra was less than 0.8% of the experimental 0V peak extinction.

The results from performing simulations to obtain the best-fit simulation for each experimental spectra provides a parameter set for the model that is appropriate at each applied bias step. These results are shown in Figures 3.6b-e. The height of the colored band in the plots represents the uncertainty due to the finite step size used in the parameter sweeps. The color of the band goes from red to blue in time to make the time direction and hysteresis of the traces more clear. Our analysis indicates that at the initial 0V data point, before any external voltage has been applied to the electrochemical cell, there is an elevated electron density of 1% at the surface of the particle compared to neutral bulk Au (Figure 3.6b). This may be due to Fermi level offsets between the ITO, electrolyte, and AuNPs or due to interactions with the electrolyte at the surface of the particles. Note that we do not claim a uniform increase of electron density throughout the particle, but only a 1% increase in the surface shell region of the metal particle. As the applied

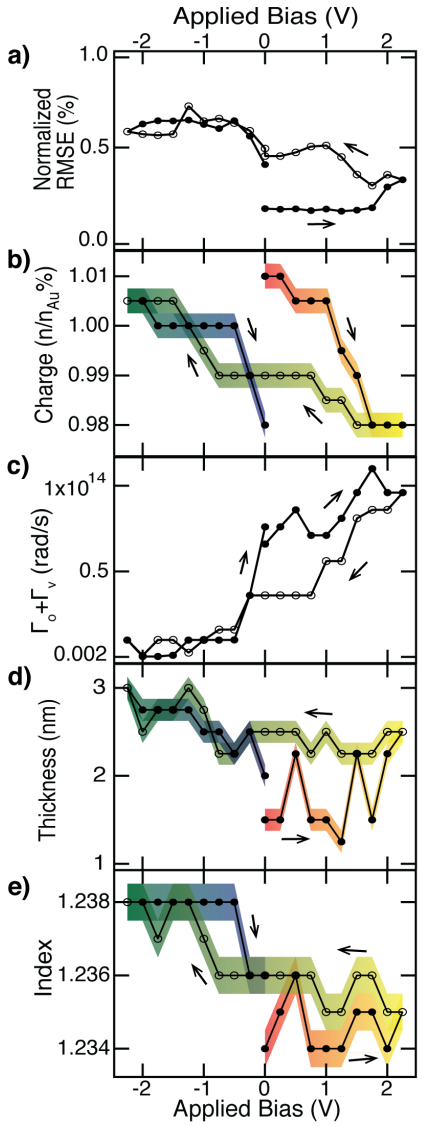

Figure 3.6: Simulation parameters that produced the spectra best-fit to the experimental spectra. (a) Root mean square error of the simulated spectra fit to the experimental spectra, normalized as a percentage of the initial 0V peak extinction. (b) Charge (electron) density and (c) total damping in the modified-dielectric particle shell versus applied bias. (d) Thickness of the modified-dielectric particle shell versus applied bias. (e) Refractive index of the surrounding medium above the ITO substrate versus applied bias. For parts b-e the height of the colored band represents the uncertainty due to the finite step size used in the parameter sweeps. For (c), the step size for Γ is smaller than the thickness of the black line. The color of the band goes from red to blue in time.

bias becomes more positive, the electron density decreases, and then increases as the applied bias becomes more negative, as expected; however, there is significant hysteresis which is not consistent with reversible, ideal charging. The overall shell charge density range for the applied potentials used was within 3% of the neutral charge density. The hysteresis upon charging/discharging is strongest in the first half of the applied bias cycle (from 0 V to 2.25V and back to 0V). This is a common feature in cyclic voltammetry measurements and may be due to initial chemical reactions or "settling" of the system during this initial application of an electric field.

The results for the damping parameter exhibit an overall trend of increased damping at positive biases and decreased damping at negative biases (Figure 3.6c). The damping coefficient used in the BB model to best describe neutral, bulk Au metal is $\Gamma_o = 7.596 \times 10^{13}$ rad/sec [67]. At the first 0V data point, we found the damping constant was 1×10^{13} rad/sec less than this value, indicating that the damping of plasmons on the AuNPs in this system is less than in bulk gold. Recalling that this data point corresponds to a 1% elevation of electron density in the particle shell, we speculate that the decreased damping could be due to electron spill-out and a resulting interlayer where the solvent is repelled and electron trapping in surface or adsorbate states is decreased, resulting in an electron configuration that experiences less damping than in the bulk. At +2.25V, we found $\Gamma_V = 3 \times 10^{13}$ rad/sec. The increase in damping at positive applied voltages is consistent with prior published work [27, 28, 56, 58], and may be due to excitation of sp-electrons in adsorbate states at the surface of the particle. Again, at negative voltages, as in the first 0V case, we found that the damping was lower than for neutral, bulk Au metal, (at -2.25V, $\Gamma_V = -6.6 \times 10^{13}$ rad/sec) and we similarly attribute this to decreased reactivity and electron spill-out at the particle surface.

The thickness of the modified-dielectric particle shell of the best-fit simulations is shown as a function of applied bias in Figure 3.6d. We found that the shell thickness varies between 1-3nm. This thickness is greater than the electrostatic skin depth of bulk metal (i.e. the Fermi screening length is ~0.3 nm for Au) and less than the optical skin depth of the nanoparticle (~10 nm), as determined from full wave simulations. Our simulations suggest that the shell thickness increases during the first rise in applied bias, and then continues to increase more gradually at negative applied biases. The initial increase in shell thickness may be due to reactivity with the electrolyte as the system "settles" under the initial application of voltage. The

electronic structure at the surface changes significantly during this period, enough for the effects on the dielectric constant to penetrate a few nanometers into the surface of the particle. It is also reasonable to suggest that the shell thickness increases at negative applied biases because the associated increase in electron density at the surface might result in the zone with a modified dielectric function protruding deeper into the particle. We believe that the thickness of the metallic shell with a modified dielectric function corresponds to the region of the particle whose electronic structure is modified due to adsorbates, surface states and an excess or deficit of electrons at the surface.

Finally, Figure 3.6e shows the results for the index of the surrounding medium as a function of applied bias. We found less than a 1% change in the refractive index of the surrounding medium. There is an overall trend indicating a slight increase in index as the applied bias goes from positive to negative. This small change could be due to a difference in the index of refraction of the cation and anion of the DEME electrolyte and alignment of these dipoles in an electric double layer [70, 71]. Significantly, we did not see an increase in the index at positive voltages as would be expected in the case of oxidation of the AuNP surface in to Au_xO_x. We note that the formation of Au halide surface compounds, induced by chemical reaction with impurities in the DEME electrolyte (<1% by supplier assay) for example, is similarly inconstant with our observations, as Au halides are also expected to exhibit a larger refractive index.

Comparison of Simulation and Experiment Over Full Wavelength Range

Figure 3.7 shows the best-fit simulation and experimental spectra for the same voltage points shown in Figure 3.3d (the 0V curves are for the first 0V applied bias point at the start of the voltage cycle). It is clear from part (a) of Figure 3.7 that the simulations do not reproduce the broadness of the experimental spectra. We attribute the amplified broadening of the experimental spectra to non-idealities present in the experimental system that were not captured in the simulations. These non-idealities include roughness of the ITO substrate, particle-particle interactions, and heterogeneity of the particles beyond the small changes in radius that are accounted for by the simulations. Part (b) of Figure 3.7 shows the absolute full width at half max for the experimental spectra and the best-fit simulated spectra. The changes in this parameter, relative to the first 0V applied bias point are shown in Figure 3.3c. There we show that the general trends of the changes in experimental peak broadness as a function of voltage are reproduced relatively well by the best-fit simulation peak

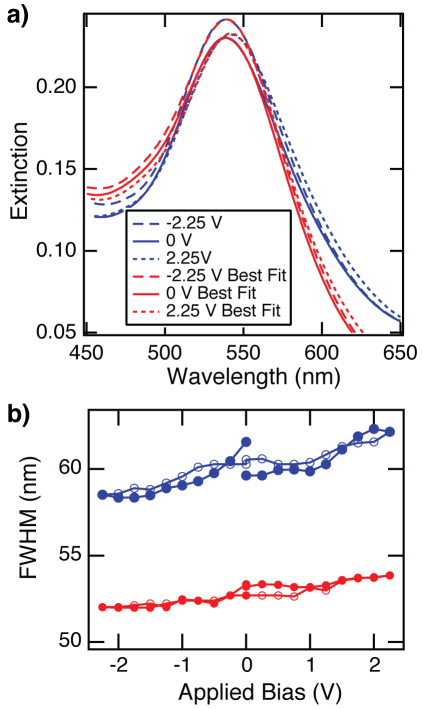

Figure 3.7: Experimental extinction spectra at 0V, +2.25V and -2.25V and their best fit simulated spectra. (b) Absolute full width half max for experimental (blue) and simulated (red) spectra. The markers for the applied bias points for the middle portion of the cycle, from 2V to -2.25V in -0.25V steps are hollow.

broadness changes. However, due to the non-idealities discussed above, the full width at half max is offset between the experimental and simulated spectra by approximately 6nm throughout the applied bias cycle.

3.6 Conclusions

In conclusion, we have shown that by using full wave electromagnetic simulations to model a AuNP with a variable-thickness conducting shell with a modified dielectric function, a variable electrolyte index, and an explicitly modeled ITO substrate, we are able to find good fits to experimental extinction spectra and track changes in the spectra as a function of applied bias. The best-fit simulation spectra correspond to a set of simulation parameters as a function of applied bias, and provide insight into the physical phenomena occurring in the experimental system under bias. Using this analysis, we have modeled the changes in the surface charge density, surface damping, and penetration depth of the resultant modified dielectric function, as well as changes in the index of refraction of the surrounding electrolyte medium. Our approach allowed us to vary these parameters independently, but also

to understand the result of the effects acting in parallel. We find that the changes in surface damping and charge density play the largest role in modifying the optical response of AuNPs under applied bias, with a smaller dependence on changes induced in the surrounding electrolyte. Based on our analysis we can relate the applied bias to changes in charge density in the AuNPs; the most non-neutral charge state of the shell, a decrease of electron density by 2% compared to bulk, occurred at +2.25V applied bias and corresponds to roughly 12,000 holes in the particle shell (calculated assuming a 2% change of charge density in a 3nm-thick shell of a 60-nm-diameter Au nanosphere). This analysis is useful as a guide to understanding optical properties of plasmonic nanostructures in non-neutral states or for which the surrounding electrochemical environment is dynamically modified, e.g. due to changes of solvent, ion concentration or photochemical changes. Thus the results presented here allow us to assess the relative importance of interface damping, surface charging, and index changes on optical extinction of plasmonic nanostructures spanning a large range of conditions relevant for chemical and biological applications.

Chapter 4

COMPLETE *AB INITIO* DESCRIPTION OF NON-RADIATIVE PLASMON DECAY

4.1 Motivation and Previous Work

Illumination of a metallic structure produces strong optical near fields that initiate a cascade of processes with multiple outcomes, including the excitation of surface plasmons, their radiative decay to photons, and their non-radiative decay in the material.[82]. Non-radiative plasmon decay includes the generation of electron-hole pairs. The energies of these electrons and holes depend on the material and the plasmon energy, and are considered 'hot' when they are significantly larger than those of thermal excitations at ambient temperatures. Decay of surface plasmons to hot carriers is a new direction that has recently attracted considerable interest in many applications of plasmonics. The decay of plasmons that determines generated carrier energy distributions and the subsequent scattering and transport of these carriers are both essential to the design of plasmonic hot carrier devices. Typically, scattering events thermalize the carriers and bring their energies closer to the Fermi level of the metal. However, plasmonic hot carrier applications require carriers far from the Fermi level to more efficiently drive both solid state and chemical processes. Hot carrier ejection into semiconductor and molecular systems has been clearly demonstrated in several recent device applications ranging from energy conversion and photocatalysis to photodetection. In particular, demonstrations of photochemistry driven by both hot electrons[83, 84] and hot holes[85] raise interesting questions regarding the timescales of plasmonic hot carrier generation and transport.[86, 87] Yet a theoretical understanding of plasmon decay and the underlying microscopic mechanisms has previously been incomplete.

Losses in metals can proceed either through classical resistive dissipation or single-particle excitations. For plasmons, these single-particle excitations constitute Landau damping that results in generating highly energetic carriers. Direct optical excitation of carriers in most metals is allowed only above an interband threshold energy due to crystal momentum conservation. Below this threshold, which typically corresponds to optical frequencies, phonons provide the necessary momentum to circumvent this selection rule. Additionally, in metals, confinement of

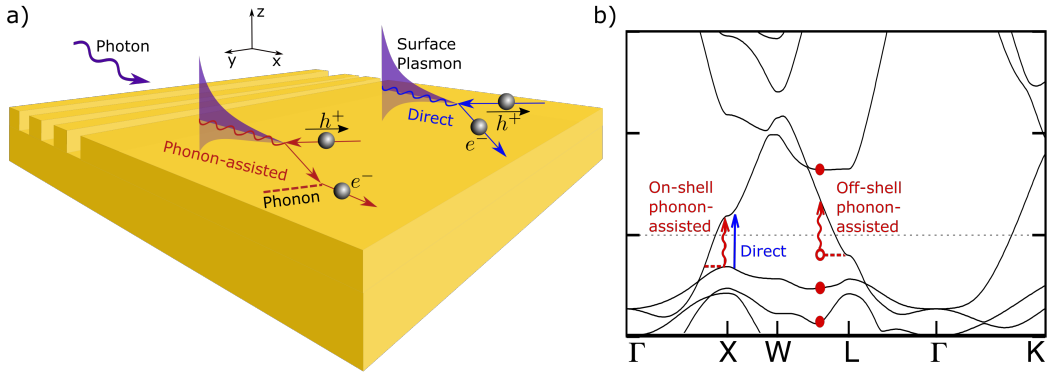

Figure 4.1: (a) Schematic for excitation and decay of surface plasmons. Surface plasmons excited, for example, through coupling to a grating or prism subsequently decay via direct and phonon-assisted transitions to generate hot electrons and holes. (b) Illustrations of direct, surface-assisted and phonon-assisted transitions on the band structure of gold. Surface-assisted transitions constitute the small but non-zero probability of non-vertical transitions due to the momentum distribution of the plasmon. The intermediate virtual state (empty circle) requires a sum over states (filled circles) in perturbation theory. When the intermediate state is a real state on the band structure (goes 'on shell'), it corresponds to a sequential process of electron-phonon scattering followed by a direct transition (or vice versa).

fields to the surface breaks translational invariance that can also provide the momentum necessary to excite intraband transitions.[88] These 'surface-assisted' and phonon-assisted transitions are important contributors to losses in metals at infrared frequencies, and hence are important to understand from both a fundamental and technological perspective.[89–92]

First principles calculations provide an opportunity to quantitatively analyze individually each microscopic mechanism underlying plasmon decay (Figure 4.1(a)) and gauge their relative contributions in different materials and at different frequencies. These calculations can examine the processes at various time scales, separating effects due to the initial distribution of hot carriers and its subsequent transport. Such a detailed understanding, which is extremely challenging to extract from experiment, elucidates opportunities to enhance plasmonic hot carrier devices as well as their fundamental limits.

Previously, Sundararaman et al. studied in detail direct interband transitions in plasmonic metals [33] and showed that the plasmon-generated hot carrier distribution is extremely sensitive to details of the electronic band structure. Specifically, they found that in noble metals the positions of the *d*-bands relative to the Fermi level result in much hotter holes than electrons, and subsequent studies confirmed these

results.[93] Sundararaman et al. also showed that the decay of surface plasmon polaritons is representative of decays in plasmonic nanostructures and that geometry effects on the generation of carriers are significant only at dimensions below ~10 nm.

In this Chapter, we report first-principles calculations that describe all of the significant microscopic mechanisms underlying surface plasmon decay and hot carrier generation. The work presented here completes the theoretical picture of surface plasmon decay by adding *ab initio* calculations of phonon-assisted transitions and resistive losses, allowing us to quantitatively predict the initial excited carrier distributions resulting from decay. Within a quasiparticle picture we include electron-electron and electron-lattice interactions in the quasiparticle energies as a part of the underlying electronic structure calculation. We also calculate electron-electron and electron-phonon scattering contributions to the quasiparticle linewidth, which determines carrier lifetimes and transport. We calculate all of these processes that have significant contributions and dominate in the relevant energy ranges and length scales, but ignore higher order processes such as decays involving multiple electron-hole pairs or multiple phonons, as these do not dominate in any regime. Previous first principles calculations of phonon-assisted transitions treat indirect-gap semiconductors below their optical gap.[94, 95] We report the first *ab initio* calculations of phonon-assisted optical excitations in metals, which are critical to bridging the frequency range between resistive losses at low frequencies and direct interband transitions at high frequencies. In this extension of calculations to metals, we show that it is necessary to treat carefully the energy-conserving 'on-shell' intermediate states, that correspond to sequential processes (Figure 4.1(b)). We predict the relative contributions of these processes and direct transitions and compare the absolute decay rates to those estimated from experimentally-measured complex dielectric functions for frequencies ranging from infrared to ultraviolet.

4.2 Experimental Decay Rate

In order to compare various contributions to surface plasmon decay with experiment on equal footing, we calculate contributions to the imaginary part of the dielectric tensor $\mathrm{Im}\bar{\epsilon}(\omega)$ and relate the complex dielectric function to the plasmon decay rate. The decay rate per unit volume is the energy loss per unit volume (see for example equation 4.26 in Ref.96) divided by the photon energy. Specifically, the decay rate per unit volume is $\frac{1}{2\pi\hbar}\vec{E}^*(\vec{r}) \cdot \mathrm{Im}\bar{\epsilon}(\omega) \cdot \vec{E}(\vec{r})$ at a point in the material where the electric field is $\vec{E}(\vec{r})$. For a surface plasmon polariton with wave-vector $\vec{k}$ and

angular frequency ω on the surface of a semi-infinite metal slab extending over $z < 0$, substituting the electric field profile of a single quantum [97, 98] and integrating over space yields the total decay rate

$$\Gamma = \frac{\omega}{2L(\omega)|\gamma(z<0)|}\vec{\lambda}^* \cdot \mathrm{Im}\bar{\epsilon}(\omega) \cdot \vec{\lambda}. \tag{4.1}$$

Here, $L(\omega)$ is the quantization length for the plasmon determined by normalizing the energy density of the mode, $|\gamma(z<0)|$ is the inverse decay length of the plasmon into the metal, and $\vec{\lambda} \equiv \hat{k} - \hat{z}k/\gamma(z<0)$ is the polarization vector. All of these quantities are fully determined by the experimental dielectric function and described in detail in Refs. 98 and 33.

We calculate the total 'experimental' decay rate of plasmons as a function of frequency by using expression 4.1 directly with the complex dielectric functions measured by ellipsometry.[36]

4.3 Electronic Structure

We require an approximation to quasiparticle energies and optical matrix elements to describe the decay of surface plasmons to quasiparticle excitations (equations 4.2, 4.3). We use the relativistic DFT+U approach that Sundararaman et al. previously established[33] to best reproduce experimental photoemission spectra in contrast to semilocal density-functional or even quasiparticle self-consistent GW methods.[99] Strong screening in metals renders electron-hole interactions and excitonic effects negligible, so that we can work at the independent quasiparticle level rather than with the more expensive Bethe-Salpeter equation[100] that accounts for those effects.

Following Ref. 33, we perform density-functional calculations in the open-source code JDFTx[101] with full-relativistic (spinorial) norm-conserving pseudopotentials at a plane-wave cutoff of 30 E_h (Hartrees). We use the PBEsol[102] exchange-correlation approximation and a rotationally-invariant localized DFT+U correction[103] for the d-electrons in noble metals (U = 1.63 eV, 2.45 eV and 2.04 eV respectively for copper, silver, and gold). Ref. 33 provides more details regarding the selection of the electronic structure method and shows that this method produces accurate electronic band structures in agreement with angle-resolved photoemission (ARPES) measurements within 0.1 eV.

We perform the self-consistent ground state calculations using a $12 \times 12 \times 12$ uniform k-point mesh centered at the Γ point along with a Fermi-Dirac smearing of

0.01 E_h to resolve the Fermi surface. The optical matrix elements correspond to the momentum operator $\hat{\vec{p}} \equiv \frac{m_e}{i\hbar}[\vec{r}, \hat{H}] = \frac{\hbar}{i}\vec{\nabla} + \frac{m_e}{i\hbar}[\vec{r}, \hat{V}_{NL}]$, which accounts for the fact that the nonlocal DFT+U and pseudopotential contributions ($\hat{V}_{NL}$) to the DFT Hamiltonian ($\hat{H}$) do not commute with the position operator, $\vec{r}$. These nonlocal corrections are usually insignificant for s and p-like electrons, but are critical for describing optical transitions involving the d-electrons in the noble metals.[104]

Finally, we interpolate the electronic energies and matrix elements to arbitrary k-points in the Brillouin zone using a basis of maximally-localized Wannier functions.[105, 106] Specifically, we use an sp^3 basis with 4 Wannier bands for aluminum and a relativistic d^5t^2 basis with 14 Wannier bands for the noble metals (where t is an orbital centered on the tetrahedral void sites of the face-centered cubic lattice). These Wannier functions exactly reproduce the orbital energies and matrix elements within the maximum surface plasmon energy of the Fermi level for all metals. We then evaluate equation 4.2 by Monte Carlo sampling $6.4 \times 10^6 \vec{q}$ values in the Brillouin zone for the noble metals (9.6×10^7 for aluminum), and histogram contributions by plasmon and carrier energies to get the direct-transition results in Figures 4.2 and 4.4. Note that aluminum requires more $\vec{q}$ samples to get similar statistics since it contributes fewer pairs of bands per $\vec{q}$.

4.4 Plasmon Decay via Direct Transitions

Within the random phase approximation, direct interband transitions contribute[33]

$$\vec{\lambda}^* \cdot \mathrm{Im}\bar{\epsilon}_{direct}(\omega) \cdot \vec{\lambda} = \frac{4\pi^2 e^2}{m_e^2 \omega^2} \int_{BZ} \frac{d\vec{q}}{(2\pi)^3} \sum_{n'n} (f_{\vec{q}n} - f_{\vec{q}n'}) \delta(\varepsilon_{\vec{q}n'} - \varepsilon_{\vec{q}n} - \hbar\omega) \left| \vec{\lambda} \cdot \langle \vec{p} \rangle_{n'n}^{\vec{q}} \right|^2, \tag{4.2}$$

where $\varepsilon_{\vec{q}n}$ and $f_{\vec{q}n}$ are the energies and occupations of electronic quasiparticles with wave-vectors $\vec{q}$ (in the Brillouin zone BZ) and band index n, and $\langle \vec{p} \rangle_{n'n}^{\vec{q}}$ are momentum matrix elements. (See Appendix Section A.1 for a derivation of equation 4.2). Note that the factor $(f_{\vec{q}n} - f_{\vec{q}n'})$ rather than $f_{\vec{q}n}(1 - f_{\vec{q}n'})$, as usually found in Fermi's Golden rule, accounts for the difference between the forward and reverse processes (see Appendix Section A.3). This is appropriate for the steady state change of plasmon number due to interactions with the electrons rather than the decay rate of a single plasmon mode. However, the two expressions are identical for $\hbar\omega >> k_B T$, which is true for all relevant plasmon energies. To account for finite carrier lifetimes, the energy-conserving δ-function is replaced by a Lorentzian with half-width $\mathrm{Im}\Sigma_{\vec{q}n} + \mathrm{Im}\Sigma_{\vec{q}n'}$, where $\mathrm{Im}\Sigma_{\vec{q}n}$ is the total carrier linewidth due to electron-electron and electron-phonon scattering as calculated in Reference 33.

Substitution of equation 4.2 into expression 4.1 results in exactly the same plasmon decay rate as previously derived by Sundararaman et al. using Fermi's Golden rule within a fully quantum many-body formalism of the electrons and plasmons.[33] We calculate the energies and matrix elements with the relativistic DFT+U method described above (Section 4.3) which produces band structures in excellent agreement with photoemission spectra. Since we use a spinorial electronic structure method to fully treat relativistic effects, and the band indices include spin degrees of freedom.

4.5 Plasmon Decay via Phonon-assisted Transitions

The contribution due to phonon-assisted transitions from second-order perturbation theory, as derived in the Appendix Section A.2, is [94, 95]

$$\begin{aligned}\vec{\lambda}^* \cdot \mathrm{Im}\bar{\epsilon}_{phonon}(\omega) \cdot \vec{\lambda} = \frac{4\pi^2 e^2}{m_e^2 \omega^2} \int_{BZ} \frac{d\vec{q}' d\vec{q}}{(2\pi)^6} \sum_{n' n \alpha \pm} (f_{\vec{q}n} - f_{\vec{q}'n'}) \\ \times \left(n_{\vec{q}'-\vec{q},\alpha} + \frac{1}{2} \mp \frac{1}{2} \right) \delta(\varepsilon_{\vec{q}'n'} - \varepsilon_{\vec{q}n} - \hbar\omega \mp \hbar\omega_{\vec{q}'-\vec{q},\alpha}) \\ \times \left| \vec{\lambda} \cdot \sum_{n_1} \left(\frac{g^{\vec{q}'-\vec{q},\alpha}_{\vec{q}'n',\vec{q}n_1} \langle \vec{p} \rangle^{\vec{q}}_{n_1 n}}{\varepsilon_{\vec{q}n_1} - \varepsilon_{\vec{q}n} - \hbar\omega + i\eta} + \frac{\langle \vec{p} \rangle^{\vec{q}'}_{n' n_1} g^{\vec{q}'-\vec{q},\alpha}_{\vec{q}'n_1,\vec{q}n}}{\varepsilon_{\vec{q}'n_1} - \varepsilon_{\vec{q}n} \mp \hbar\omega_{\vec{q}'-\vec{q},\alpha} + i\eta} \right) \right|^2 , \quad (4.3)\end{aligned}$$

where $\hbar\omega_{\vec{k}\alpha}$ is the energy of a phonon with wave-vector $\vec{k}$ and polarization index α; $n_{\vec{k}\alpha}$ is the corresponding Bose occupation factor and $g^{\vec{k}\alpha}_{\vec{q}'n',\vec{q}n}$ is the corresponding electron-phonon matrix element with electronic states labeled by wave-vectors $\vec{q}, \vec{q}'$ and band indices n, n' (with $\vec{k} = \vec{q}' - \vec{q}$ for crystal momentum conservation). The sum over $\pm$ accounts for phonon absorption as well as emission. Since the *ab initio* matrix elements couple all pairs of wave-vectors in the Brillouin zone, they implicitly account for wrap-around (Umklapp) processes.

We calculate the phonon energies and electron-phonon matrix elements consistently using the same relativistic DFT+U approximation as for the electronic states (Section 4.3). We use a Wannier representation to efficiently interpolate the phonon energies and matrix elements to calculate the Brillouin zone integrals in expression 4.3 accurately (see Section 4.6 for details on the phonon states and matrix elements).

Extrapolation to Eliminate Sequential Processes

The imaginary part of the energy denominator, η, in the second line of equation 4.3 corresponds to the linewidth of the intermediate electronic state (with band index

n_1). The value of η does not affect the phonon-assisted absorption at photon energies less than the optical gap of materials previously considered [94, 95] and is usually treated as a numerical regularization parameter. However, above the optical gap (the interband threshold for metals), the real part of the denominator crosses zero when the intermediate state conserves energy (i. e. is 'on shell'), making the resulting singular contributions inversely proportional to η. These singular contributions correspond to sequential processes: electron-phonon scattering followed by a direct interband transition or vice versa (Figure 4.1(b)). For a metal, including contributions from these sequential processes would lead to a multiple counting of the direct transition. Scattering events preceding the optical transition are a part of the equilibrium Fermi distribution, while scattering events following the optical transition correspond to the subsequent inelastic relaxation of the generated carriers. We avoid multiple counting by taking advantage of the η independence of the non-singular part and the η^{-1} variation of the singular part and extrapolating from calculations done using two values of η, as described below.

By taking the limit $\eta \to 0$ in equation 4.3 and noting that $|1/(x+i\eta)|^2 \to \pi\delta(x)/\eta$, we can show that

$$\vec{\lambda}^* \cdot \mathrm{Im}\bar{\epsilon}_{phonon}(\vec{q}'n', \vec{q}n) \cdot \vec{\lambda} = \frac{\mathrm{Im}\Sigma^{e-ph}_{\vec{q}n'}}{\eta} \left(\vec{\lambda}^* \cdot \mathrm{Im}\bar{\epsilon}_{direct}(\vec{q}n', \vec{q}n) \cdot \vec{\lambda}\right) + \left(\vec{\lambda}^* \cdot \mathrm{Im}\bar{\epsilon}_{direct}(\vec{q}'n', \vec{q}'n) \cdot \vec{\lambda}\right) \frac{\mathrm{Im}\Sigma^{e-ph}_{\vec{q}n}}{\eta} + O(\eta^0) + O(\eta^1) + \cdots, \quad (4.4)$$

where $\mathrm{Im}\bar{\epsilon}(\vec{q}'n', \vec{q}n)$ denotes the contribution to $\mathrm{Im}\bar{\epsilon}$ due to a specific pair of initial and final electronic states. Here, $\mathrm{Im}\Sigma^{e-ph}_{\vec{q}n}$ is the electron line width due to electron-phonon scattering, given by

$$\mathrm{Im}\Sigma^{e-ph}_{\vec{q}n} = \pi \int_{BZ} \frac{\Omega d\vec{q}'}{(2\pi)^3} \sum_{n'\alpha\pm} \left(n_{\vec{q}'-\vec{q},\alpha} + \frac{1}{2} \mp \frac{1}{2}\right) \times \delta(\varepsilon_{\vec{q}'n'} - \varepsilon_{\vec{q}n} \mp \hbar\omega_{\vec{q}'-\vec{q},\alpha}) \left| g^{\vec{q}'-\vec{q},\alpha}_{\vec{q}'n',\vec{q}n} \right|^2, \quad (4.5)$$

where the electronic states, phonon modes, and electron-phonon matrix elements are computed exactly as for the phonon-assisted decay (see Ref. 34).

The above expansion in η (equation 4.4) clearly illustrates that the singular contributions correspond to sequential processes. The first term on the right hand side

corresponds to a direct transition followed by electron-phonon scattering while the second term corresponds to the reverse. If we substitute the intermediate state linewidth $\mathrm{Im}\Sigma_{\vec{q}n}$ for η as the formalism prescribes,[94, 95] and for simplicity focus only on electron-phonon scattering contributions $\mathrm{Im}\Sigma^{e-ph}_{\vec{q}n}$ (which are dominant for low energy carriers), then we see that the η-singular part reduces to simply twice the direct contribution (expression 4.2). For a metal, this contribution should not be counted as a separate decay rate since scattering events preceding and following a transition are part of the initial Fermi distribution and the subsequent carrier transport, respectively.

We eliminate the singular contributions using an extrapolation scheme designed to exploit the fact that the η dependence is different for on-shell and off-shell processes. To retain the non-singular $O(\eta^0)$ terms while canceling the $O(\eta^{-1})$ singular terms discussed above, we modify equation 4.3 as

$$(4.3)_{corrected} = 2\ (4.3)|_{2\eta} - (4.3)|_{\eta}\ . \tag{4.6}$$

We find that $\eta = 0.1$ eV, which was previously used for semiconductors,[94] is sufficiently large to keep the singular terms resolvable for effective subtraction and sufficiently small to have negligible impact on the physical non-singular contributions. We note that this extrapolation only has an effect and is necessary above the optical gap of the material. Previous *ab initio* studies of phonon-assisted processes did not deal with this issue since they focused on predictions for semiconductors above the indirect gap and below the direct (optical) gap.

4.6 Phonon Modes and Matrix Elements

We calculate the *ab initio* force matrix for phonons and electron-phonon matrix elements from direct perturbations of atoms in a $4 \times 4 \times 4$ supercell using exactly the same electronic DFT parameters as above in JDFTx.[101] All four metals considered here have a single atom basis and hence exactly three acoustic phonon modes. We cast these phonon energies and matrix elements into a Wannier basis to enable interpolation for a dense sampling of the Brillouin zone integrals. (See Ref. 107 for a detailed introduction; we implement an analogous method in JDFTx, with additional support for spinorial relativistic calculations.)

We use the aforementioned Wannier basis to cover the energy range close to the Fermi level, and add random-initialized maximally-localized Wannier orbitals orthogonal to the first set to extend the energy range of included unoccupied states. We use a total of 24 Wannier bands for aluminum and 46 spinorial Wannier bands

for the noble metals that exactly reproduce the orbital energies, and optical and phonon matrix elements up to at least 50 eV above the Fermi level. We find this energy range of unoccupied states sufficient to fully converge the sum over states in the second order perturbation theory expression 4.3 at all plasmon energies considered.

Finally, we evaluate the double integral over the Brillouin zone in expression 4.3 by Monte Carlo sampling with $2 \times 10^7\{\vec{q},\vec{q}'\}$ pairs for the noble metals (3×10^8 pairs for aluminum to get similar statistics). We use standard temperature, $T = 298$ K, to calculate the Fermi occupations for electrons and Bose occupations for phonons. Note that such low electronic temperatures (compared to the Fermi energy $\sim 10^5$ K) necessitate extremely dense Brillouin zone sampling, which is, in turn, made practical by the Wannier interpolation.[107] Histogramming by plasmon and carrier energies, we collect the phonon-assisted contributions to Figures 4.2 and 4.4 (after incorporating the extrapolation discussed above to eliminate sequential process contributions).

4.7 Surface-assisted Transitions

In metals, the strong confinement of fields at the surface introduces an additional mechanism for intraband transitions. The exponential decay of the fields in the metal with inverse decay length $|\gamma(z<0)|$ introduces a Lorentzian distribution in the momentum of the plasmon normal to the surface with width $\sim |\gamma(z<0)|$. (This can also be interpreted in terms of the uncertainty principle.) This momentum distribution allows diagonal intraband transitions on the band structure (Figure 4.1(b)), which contributes a 'surface-assisted' loss[88, 108]:

$$\mathrm{Im}\epsilon_{surface}(\omega) = \frac{\omega_p^2}{\omega^3} \times \left(\frac{3}{4}|\gamma(z<0)|v_F\right) \frac{2k^2}{k^2+|\gamma(z<0)|^2}. \tag{4.7}$$

Here, $\omega_p = \sqrt{4\pi ne^2/m_e}$ is the the bulk plasma frequency of the metal and $v_F = (\hbar/m_e)\sqrt[3]{3\pi^2 n}$ its Fermi velocity, where n is the bulk carrier density of the metal. In nano-confined geometries, such as spherical nanoparticles, the probability of intraband transitions due to crystal momentum non-conservation can be greatly enhanced, as shown by several numerical studies using free-electron jellium models.[109–111] We can show from a full quantum-mechanical treatment of the states of a spherical nanoparticle that geometry-assisted transitions effectively contribute

$$\mathrm{Im}\epsilon_{sphere}(\omega) = \frac{\omega_p^2}{\omega^3} \times \frac{6\pi^2 v_F}{R}, \tag{4.8}$$

where R is the radius of the spherical nanoparticle. This is similar to expression 4.7 except for dimensionless prefactors and the particle radius setting the length scale instead of the skin depth. See Ref. 108 for detailed derivations of these contributions.

The direct, surface/geometry-assisted, and phonon-assisted transitions considered above are the lowest-order processes for the decay of a plasmon to single-particle excitations, which correspond to the Landau damping of the plasmon on the Fermi sea.[112–114] Higher-order processes including multiple electron-hole pairs or multiple phonons are suppressed by phase-space factors at low energies and become important only at higher energies that are not usually accessed by surface plasmons.[4]

4.8 Estimate of Resistive Losses

Apart from Landau damping, an additional source of plasmon loss is the intrinsic lifetime of the electronic states comprising the collective oscillation and results in heating rather than production of a few energetic carriers. This corresponds to a resistive loss in the material. Single electron-hole pair generation dominates the plasmon decay at high frequencies, while resistive loss in the metal dominates at frequencies close to 0 eV. Here, we estimate these losses from the frequency-dependent resistivity calculated *ab initio* within a linearized Boltzmann equation with a relaxation time approximation.

The Boltzmann equation for electron occupations $f_{\vec{q}n}(t)$ in a uniform time-dependent electric field $\vec{E}(t)$ is[115]

$$\frac{\partial f_{\vec{q}n}(t)}{\partial t} + e\vec{E}(t) \cdot \frac{\partial f_{\vec{q}n}(t)}{\partial \vec{p}} = \left.\frac{\partial f_{\vec{q}n}}{\partial t}\right|_{coll}. \tag{4.9}$$

We then substitute $f_{\vec{q}n}(t) = f_{\vec{q}n} + \delta f_{\vec{q}n}(t)$, where the first term is the equilibrium Fermi distribution and the second contains perturbations to linear order due to the applied electric field, and collect contributions at first order in $\vec{E}(t)$.

To first order, the collision integral on the right-hand side of equation 4.9 can be written as $-\delta f_{\vec{q}n}\tau^{-1}_{\vec{q}n}$, where $\tau^{-1}_{\vec{q}n}$ is the difference between rates of scattering out of and into the electronic state $\vec{q}n$. Within the relaxation time approximation, we assume that $\tau^{-1}_{\vec{q}n}$ is approximately constant for carriers near the Fermi level, and replace it by an average τ^{-1} (inverse of momentum relaxation time). This is an excellent approximation for metals where electron-phonon scattering dominates carrier relaxation near the Fermi level,[115] which is the case for most elemental metals

(except those with partially occupied d-shells) including aluminum and the noble metals.

Switching equation 4.9 to the frequency domain, linearizing, invoking the relaxation time approximation, and rearranging, we get

$$\delta f_{\vec{q}n}(\omega) = \frac{-e f'_{\vec{q}n}}{\tau^{-1} - i\omega} \vec{v}_{\vec{q}n} \cdot \vec{E}(\omega), \tag{4.10}$$

where $\vec{v}_{\vec{q}n} \equiv \frac{\partial \varepsilon_{\vec{q}n}}{\partial \vec{q}}$ is the group velocity of electronic state $\vec{q}n$ and $f'_{\vec{q}n}$ is the energy derivative of the Fermi-Dirac distribution. We then calculate the current density $\vec{j} = \sum_{\vec{q}n} e f_{\vec{q}n} \vec{v}_{\vec{q}n}$, and obtain the conductivity tensor by factoring out $\vec{v}_{\vec{q}n}$. Averaging over directions, the isotropic conductivity is then

$$\sigma(\omega) = \frac{1}{1 - i\omega\tau} \underbrace{e^2 \tau \int_{BZ} \frac{d\vec{q}}{(2\pi)^3} \sum_n (-f'_{\vec{q}n}) \frac{v^2_{\vec{q}n}}{3}}_{\equiv \sigma_0}, \tag{4.11}$$

where σ_0 is the zero-frequency (DC) conductivity.

Finally we calculate the momentum relaxation time τ using Fermi golden rule for electron-phonon scattering. In the average, we weight the scattering rates by $(-f'_{\vec{q}n}) \frac{v^2_{\vec{q}n}}{3}$ since that determines the relative contributions to the conductivity above. It is then straightforward to show that $\tau^{-1} = \Gamma_{sum}/w_{sum}$, where

$$\begin{aligned} \Gamma_{sum} = \frac{2\pi}{\hbar} \int_{BZ} \frac{\Omega d\vec{q} d\vec{q}'}{(2\pi)^6} \sum_{n'n\alpha\pm} (-f'_{\vec{q}n}) \frac{v^2_{\vec{q}n} - \vec{v}_{\vec{q}n} \cdot \vec{v}_{\vec{q}'n'}}{3} \\ \times \left[n_{\vec{q}'-\vec{q},\alpha} + \frac{1}{2} \mp \left(\frac{1}{2} - f_{\vec{q}'n'} \right) \right] \\ \times \delta(\varepsilon_{\vec{q}'n'} - \varepsilon_{\vec{q}n} \mp \hbar\omega_{\vec{q}'-\vec{q},\alpha}) \left| g^{\vec{q}'-\vec{q},\alpha}_{\vec{q}'n',\vec{q}n} \right|^2 \end{aligned} \tag{4.12}$$

with all the *ab initio* electron and phonon properties defined exactly as before, and where the denominator for normalizing the weights is

$$w_{sum} = \int_{BZ} \frac{d\vec{q}}{(2\pi)^3} \sum_n (-f'_{\vec{q}n}) \frac{v^2_{\vec{q}n}}{3}. \tag{4.13}$$

Note that with this definition, we can simplify the DC conductivity, $\sigma_0 = e^2 \tau w_{sum} = e^2 w^2_{sum}/\Gamma_{sum}$.

Given the frequency-dependent conductivity of the metal, we can calculate the resistive losses $\mathrm{Im}\epsilon = \mathrm{Im}\left[4\pi i \sigma(\omega)/\omega\right]$, which, upon simplification gives

$$\mathrm{Im}\epsilon_{resistive}(\omega) = \frac{4\pi\sigma_0}{\omega(1 + \omega^2\tau^2)}, \tag{4.14}$$

Table 4.1: *ab initio* momentum relaxation times and resistivities of plasmonic metals at $T = 298$ K, compared to experimental resistivities from Ref. 116.

Metal	τ [fs]	$\rho_0 = \sigma_0^{-1}$ [Ωm]	Expt ρ_0 [Ωm]
Al	12.0	2.46×10^{-8}	2.71×10^{-8}
Cu	35.6	1.58×10^{-8}	1.71×10^{-8}
Ag	36.4	1.58×10^{-8}	1.62×10^{-8}
Au	26.3	2.23×10^{-8}	2.26×10^{-8}

We calculate w_{sum} and Γ_{sum} using Monte Carlo sampling of the Brillouin zone integrals with $1.6 \times 10^6 \vec{q}$ values for the single integral and $5 \times 10^7 \{\vec{q}, \vec{q}'\}$ pairs for the double integral, which converges τ and σ_0 within 1%. Table 4.1 lists the momentum-relaxation time and resistivity we predict for the common plasmonic metals. The excellent agreement with experimental resistivities demonstrates the quantitative accuracy of the *ab initio* electron-phonon coupling (better than 10% in all cases).

4.9 Results for Common Plasmonic Metals

Fig. 4.2 compares the plasmon linewidth and decay rates estimated directly from the experimentally-measured complex dielectric functions with theoretical predictions for cumulative contributions from direct, surface-assisted, phonon-assisted transitions and resistive losses. For all the common plasmonic metals, aluminum and the noble metals, we find that direct transitions dominate above the interband threshold ($\sim 1.6 - 1.8$ eV for aluminum, gold, and copper and ~ 3.5 eV for silver). All other contributions add to less than 10% above threshold, and hence the cumulative results overlay the direct transition lines. In silver, the maximum plasmon frequency coincides with the interband threshold and hence there is no accessible frequency range for which direct transitions dominate. In aluminum, direct transitions are in fact possible at all frequencies due to a band crossing near the Fermi level,[33] but an additional channel for direct transitions with much higher density of states opens up at the effective threshold of ~ 1.6 eV.

Below the threshold, direct transitions are forbidden (or for aluminum, are weak) and the contributions due to the other processes become important. Surface-assisted processes contribute only a small fraction (at most 5%) of the experimental linewidth over the entire frequency range below threshold. Phonon-assisted transitions and resistive losses compete significantly and dominate this frequency range. The relative importance of phonon-assisted transitions increases slightly with frequency,

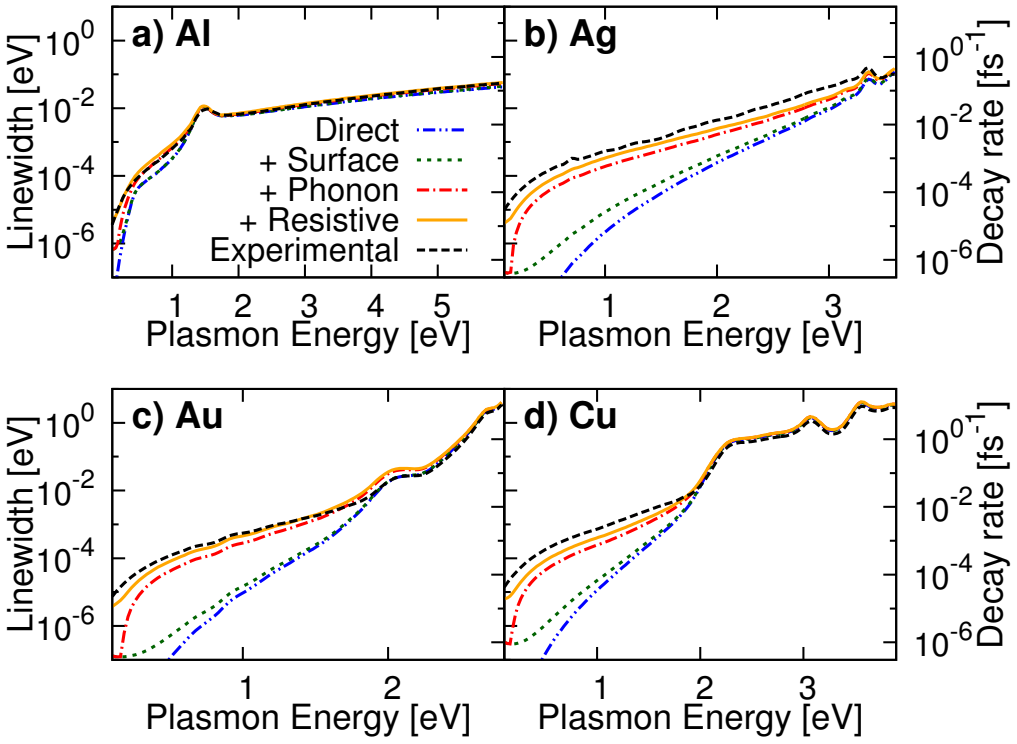

Figure 4.2: Comparison of calculated and experimental linewidths (left axis) and decay rates (right axis) in (a) Al (b) Ag (c) Au and (d) Cu. The theoretical curves indicate cumulative contributions from direct transitions alone ('Direct'), including surface-assisted transitions ('+Surface'), including phonon-assisted transitions ('+Phonon'), and including resistive losses ('+Resistive').

with resistive and surface-assisted losses dominating at very low frequencies (close to 0 eV in these plots), an approximately even split between the three processes at $\sim$ 1 eV, and a greater contribution from phonon-assisted transitions just below threshold.

The total theoretical prediction including all these contributions agrees very well with experiment over the entire range of frequencies.[36] Above threshold for the noble metals, the theoretical predictions overestimate experiment by $\sim 10-20\%$, which is the typical accuracy of optical matrix elements involving d electrons in density-functional theory.[104] Below threshold, the total theory result underestimates the experimental value but it is typically within a factor of two from it. This is, in part, because material non-idealities could contribute additional losses and our theoretical calculations estimate an ideal lower bound. In fact, the largest discrepancy is for silver because these ideal losses are the smallest and the non-idealities become more important relatively. Also note that there is a significant spread in tab-

ulated experimental dielectric functions for the noble metals,[36] with discrepancies a factor of two or higher in the imaginary parts at infrared frequencies. (We used the measurements that covered the greatest frequency range.) Therefore, more careful experimental measurements in that frequency range with higher quality samples would be necessary and useful for a stricter comparison.

The results in Fig. 4.2 are based on calculations at standard room temperature, $T = 298$ K. We expect the direct and surface-assisted contributions to be approximately independent of temperature, the resistive contributions to decrease almost linearly with temperature, and the phonon-assisted contributions to reduce by a factor of two upon lowering the temperature (phonon emission persists while phonon absorption freezes out). Therefore, at very low temperatures, phonon-assisted transitions will dominate below threshold, while direct transitions continue to dominate above threshold.

Fig. 4.3 compares the relative contributions due to all the above processes to absorption in the surface of bulk gold and spherical gold nanoparticles of various sizes. Geometry-assisted intraband contributions are negligible for a semi-infinite surface, and are comparable to the phonon-assisted and resistive contributions for a 40 nm diameter sphere below threshold. With decreasing particle size, the relative contributions of the geometry-assisted transitions increase in inverse proportion and dominate the sub-threshold absorption in gold spheres smaller than 20 nm. However, direct transitions continue to dominate above the interband threshold even for these small spheres. Therefore, simplified treatment of localized plasmon decay in nanoparticles using jellium models that preclude direct transitions[109–111] is only reasonable for frequencies below the interband threshold. Those approximations are therefore reasonable for silver, where the interband threshold exceeds the dipole resonance frequency, but not for gold, copper or aluminum.

Figure 4.4 shows the initial carrier distributions generated via direct and phonon-assisted transitions, which we calculate by histogramming the integrands in expressions 4.2 and 4.3 by the initial (hole) and final (electron) state energies. The carrier distributions are plotted as a function of carrier energy (horizontal axis) and plasmon / photon energy (axis normal to the page). The color scale indicates the fraction of carriers generated by direct or phonon-assisted transitions. Note that carrier energies may exceed the plasmon energy with low probability because of the Lorentzian broadening due to carrier linewidths in energy conservation (equivalently, a consequence of the uncertainty principle); this causes the small contributions from direct

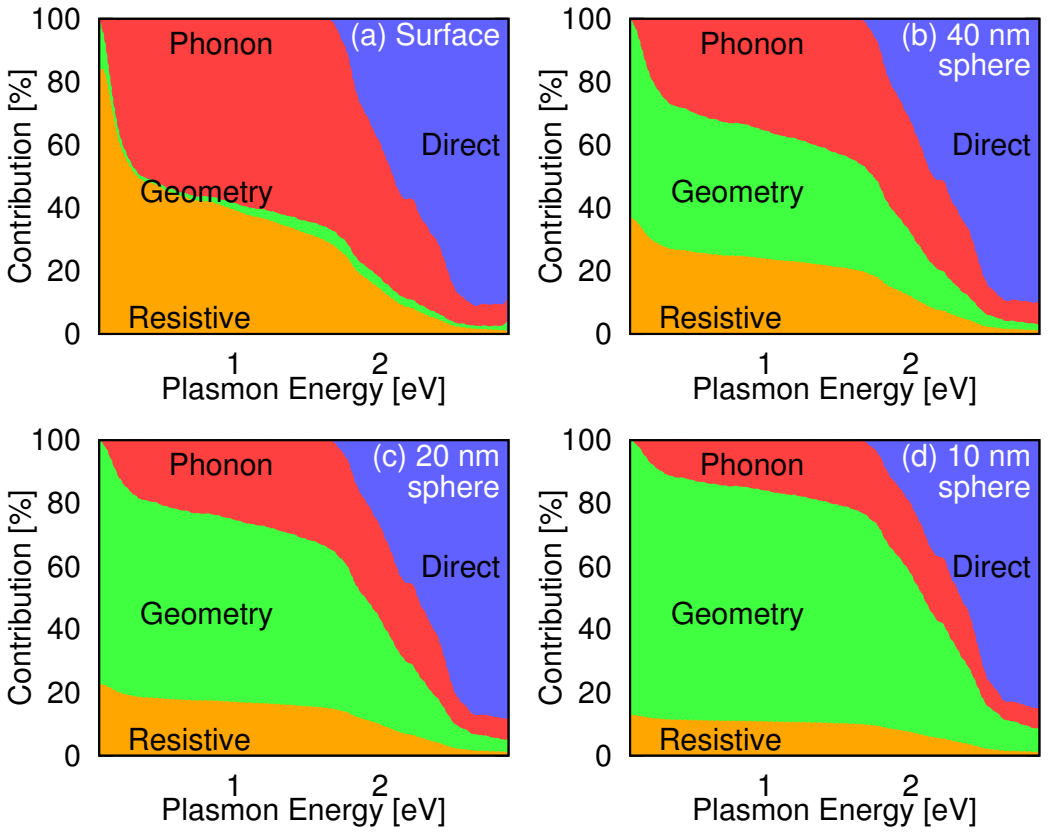

Figure 4.3: Comparison of resistive, geometry-assisted, phonon-assisted and direct transition contributions to absorption in gold as a function of frequency for (a) a semi-infinite surface, or (b) 40 nm, (c) 20 nm or (d) 10 nm diameter spheres. The surface/geometry contributions are negligible for the semi-infinite surface, are comparable to the phonon-assisted and resistive contributions for a 40 nm sphere, and increase in inverse proportion with decreasing sphere diameter. Direct transitions dominate above threshold in all cases.

transitions below threshold seen for the noble metals in Figure 4.4.

Direct transitions, shown in blue, dominate at high energies and exhibit the strong material dependence previously discussed in detail in Ref. 33. For copper and gold, direct transitions occur from the *d*-bands to unoccupied states above the Fermi level, which results in holes that are much more energetic than electrons. Aluminum exhibits a relatively flat distribution of electrons and holes, while silver exhibits a bimodal distribution of hot electrons as well as holes from direct transitions in a very narrow frequency range close to the maximum plasmon frequency.

Phonon-assisted transitions, shown in red, exhibit a flat distribution of electrons and holes extending from zero to the plasmon energy for all the metals. In aluminum,

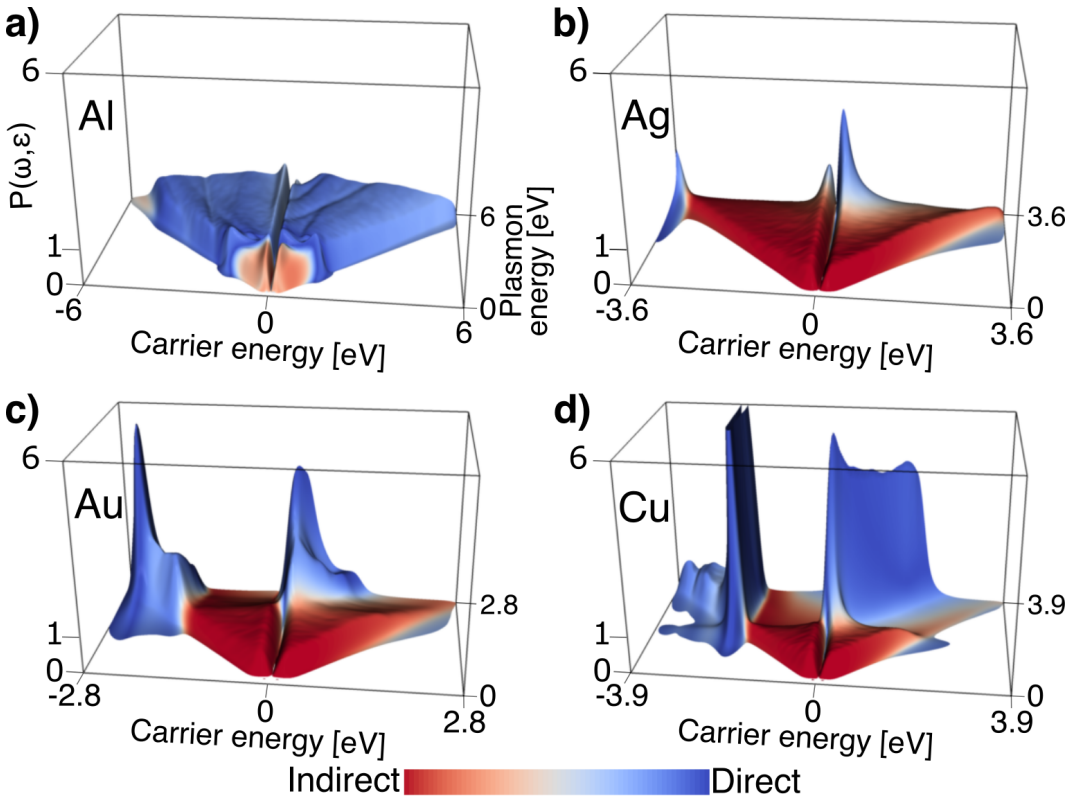

Figure 4.4: Probability density energy distributions of hot carriers, $P(\omega,\varepsilon)$, generated by the decay of surface plasmons due to phonon-assisted and direct transitions, as a function of plasmon frequency (ω) and carrier energy (ε), in (a) Al (b) Ag (c) Au and (d) Cu. The color-scale indicates the relative contributions of phonon-assisted (red) and direct (blue) transitions. For each frequency, $P(\omega,\varepsilon)$ is normalized such that it equals 1 for a flat distribution, similar to the red plateaus below threshold where phonon-assisted transitions dominate.

direct transitions are also possible below the threshold at 1.6 eV and contribute $\sim$ 25% of the generated carriers. Geometry-assisted intraband transitions (in the surface or sphere cases) have a similar phase space to phonon-assisted transitions and also generate flat distributions of electron and hole energies. Resistive losses compete with phonon-assisted transitions but dissipate thermally and do not generate energetic hot carriers. Due to these losses, below threshold $\sim 30-50\%$ of the absorbed energy is dissipated without hot carrier generation. Therefore, plasmonic hot-carrier applications could benefit from the higher efficiency above threshold, where direct transitions dominate by far and result in high-energy carriers. Additionally, we predict aluminum to be an excellent candidate for general hot carrier applications since it allows direct transitions at all energies and has the smallest fraction of resistive loss (despite its absolute resistivity being higher than other met-

als).

4.10 Conclusions

We preformed the first *ab initio* calculations of phonon-assisted optical excitations in metals, allowing us to link the energy range between resistive losses at low energies (microwave-infrared) and direct interband transitions at high energies (visible-ultraviolet). Along with surface-assisted transitions due to field confinement in metals,[88] this completes the theoretical picture of surface plasmon decay, accounting for all relevant mechanisms.

We find good agreement with experimental measurements for the total decay rate, but we additionally predict the relative contributions of all these processes and the initial generation of hot carriers in plasmonic metals. We find that direct transitions dominate above threshold and generate hot carriers, while below threshold, hot carrier generation by phonon-assisted transitions is diminished by competition from resistive losses. We also find that surface-assisted transitions are enhanced in nano-confined geometries and become dominant below threshold for particle sizes ~ 10 nm, but that direct transitions remain dominant above the interband threshold even for small particles.

We suggest that aluminum is quite promising as a general-purpose plasmonic hot carrier generator since it generates hot carriers efficiently for the widest frequency range, and generates high-energy electrons and holes with equal probability. Compared to the noble metals, aluminum also exhibits the best transport properties for high energy holes. In the future, a detailed analysis of the transport of energetic carriers in real metal nanostructures, based on the initial carrier distributions and scattering rates predicted here, could enable directed design of optimal hot carrier devices.

Chapter 5

AB INITIO DESCRIPTION OF HOT ELECTRON RELAXATION IN PLASMONIC METALS

5.1 Motivation and Previous Work

In the previous Chapter, we discussed the non-radiative decay of plasmons into hot electron-hole pairs. After this decay has taken place and a nonthermal distribution of electrons and holes has thus been established, a series of decay processes take place in which the electrons thermalize among themselves and with the lattice until a new equilibrium state is reached. Understanding the energy transfer mechanisms during these equilibration processes is critical for a wide array of applications.

In the system we consider here, an incident ultrashort laser pulse excites a plasmon on the surface of a metal. This plasmon may decay into a hot (non-thermal) electron-hole pair, as discussed in Chapter 4. The electron bath is then warmed by the energy of the hot electron via electron-electron scattering. The electron dynamics during this thermalization process are determined by the electronic density of states and the related electronic heat capacity. The electron bath then cools by transferring energy to the lattice via electron-phonon scattering. The rate of this electron-phonon equilibration process is determined by the electron-phonon scattering matrix element and the density of states. Finally, the lattice cools via phonon-phonon scattering with the surrounding environment. See Figure 5.1 for a schematic representation of these processes.

Describing the evolution of the excited non-equilibrium electron distribution has been the subject of intense research for two decades.[117–121] The dynamics of the nonthermalized and thermalized electrons and phonons are most efficiently observed with pulsed laser measurement techniques in transient absorption experiments, where resolution of tens of femtoseconds can be achieved.[122–128] The majority of investigations of hot carrier relaxation have employed various approximate models for analysis of experimental data, typically based on free-electron models and empirical electron-phonon interaction parameters, to calculate the energy absorption, electron-electron thermalization, and electron-phonon relaxation.[32, 129–133] A complete *ab initio* description of the time evolution and optical response of this non-equilibrium electron gas from femtosecond to picosecond time

scales had not yet been achieved, and few analyses have avoided empirical treatment of electron-phonon interactions.[31]

The initial internal electron thermalization via electron-electron scattering is qualitatively described within Landau Fermi liquid theory.[134–137] The subsequent relaxation of the high temperature electron gas with the lattice is widely described by the two-temperature model (TTM),[31, 32, 126–128] given by coupled differential equations for the electron and lattice temperatures, T_e and T_l, respectively,

$$\begin{aligned} C_e(T_e)\frac{dT_e}{dt} &= \nabla \cdot (\kappa_e \nabla T_e) - G(T_e) \times (T_e - T_l) + S(t) \\ C_l(T_l)\frac{dT_l}{dt} &= \nabla \cdot (\kappa_p \nabla T_p) + G(T_e) \times (T_e - T_l). \end{aligned} \tag{5.1}$$

Here, $C_e(T_e)$ and $C_l(T_l)$ are the electronic and lattice heat capacities, $G(T_e)$ is the electron-phonon coupling factor, $S(t)$ is the source term which describes energy deposition by a laser pulse, and κ_e and κ_p are the thermal conductivities of the electrons and phonons. In nanostructures, temperatures rapidly become homogeneous in space and the contributions of the thermal conductivities drop out. A vast majority of studies treat the material parameters $C_e(T_e)$, $C_l(T_l)$ and $G(T_e)$ as phenomenological temperature-independent constants or as linear approximations.

A key challenge in the quantitative application of the two temperature model is the determination of these *temperature-dependent* material parameters. With pulsed lasers, it is possible to absorb sufficient energy in plasmonic nanostructures to melt the metal once the electrons and lattice have equilibrated.[138] The highest electron temperature, T_e^{max}, accessible in repeatable measurements is therefore limited only by the equilibrated lattice temperature being less than the melting temperature T_m of the metal,[116] which yields the condition $\int_{T_m}^{T_e^{max}} dT_e C_e(T_e) = \int_{T_0}^{T_m} dT_l C_l(T_l)$. Starting at room temperature $T_0 = 300$ K and using our *ab initio* calculations of the electron and lattice heat capacities, $C_e(T_e)$ and $C_l(T_l)$ (see Sections 5.3, 5.4), we find $T_e^{max} \approx 5700$, 8300, 7500, and 6700 K, respectively, for aluminum, silver, gold, and copper. These maximum electron temperatures are much higher than the melting temperatures of the metals because the lattice heat capacity is on the order of two times larger than the electronic heat capacity. For gold and copper in particular, these maximum electron temperatures are sufficient to change the occupations of the d-band electrons ~ 2 eV below the Fermi level. Consequently, it is important to derive the temperature dependence of these material parameters from electronic structure calculations rather than free-electron like models.[31]

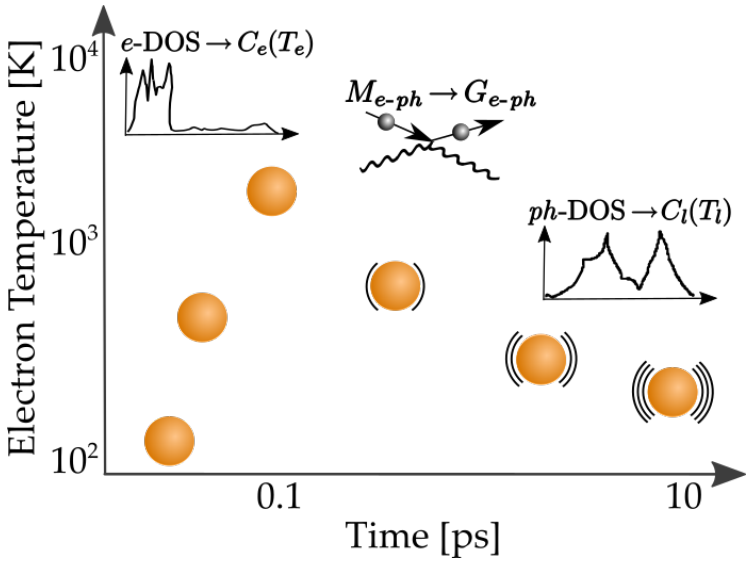

Figure 5.1: Evolution of the non-equilibrium 'hot' electrons with time with different regimes dominated by distinct material properties. The electronic density of states (DOS) determines the electronic heat capacity $C_e(T_e)$ and the temperature to which the electrons equilibrate. The electron-phonon coupling $G(T_e)$ determines the dynamics of energy transfer from the electrons to the phonons. The phonon density of states determines the lattice heat capacity C_l and the temperature to which the lattice equilibrates. All of these properties are particularly sensitive to the electron temperature T_e, and are essential for a quantitative description of the ultrafast response of plasmonic metals under laser excitation.

To accurately predict the transient optical response of metal nanostructures, we account for the electron temperature dependence of the electronic heat capacity, electron-phonon coupling factor, and dielectric function. These properties, in turn, require accurate electron and phonon band structures as well as electron-phonon and optical matrix elements. In Chapter 4, we showed that *ab initio* calculations can quantitatively predict optical response, carrier generation, and electron transport in plasmonic metals in comparison with experiment, with no empirical parameters.[34] In this Chapter, we calculate $C_e(T_e)$, $G(T_e)$ and the temperature and frequency-dependent dielectric function, $\epsilon(\omega, T_e)$ from first principles. This is the first *ab initio*, temperature dependent dielectric function presented for metals, which is a great advancement over the Drude model dielectric function with Matthiessen's rule for temperature dependence, which has been heavily relied upon by previous investigations.[31, 121, 139] Our calculations implicitly include electronic-structure effects in the density of states and electron-phonon interaction matrix elements, and implicitly account for processes such as Umklapp scattering. We show substantial differences between our fully *ab initio* predictions and those from

simplified models due to the energy dependence of the electron-phonon matrix elements, especially at high electron temperatures where the d-bands contribute.

5.2 Computational Methods

We perform *ab initio* calculations of the electronic states, phonons, electron-phonon and optical matrix elements, as well as several derived quantities based on these properties, for four plasmonic metals: aluminum, copper, silver, and gold. We use the PBEsol+U density functional theory methods described in Section 4.3.

We calculate phonon energies and electron-phonon matrix elements using perturbations on a $4 \times 4 \times 4$ supercell. In *ab initio* calculations, these matrix elements implicitly include Umklapp-like processes. We then convert the electron and phonon Hamiltonians to a maximally-localized Wannier function basis,[106] with 12^3 k-points in the Brillouin zone for electrons. Specifically, we employ 24 Wannier centers for aluminum and 46 spinorial centers for the noble metals, which reproduces the DFT band structure exactly to at least 50 eV above the Fermi level.

Using this Wannier representation, we interpolate the electron, phonon, and electron-phonon interaction Hamiltonians to arbitrary wave-vectors and perform dense Monte Carlo sampling to accurately evaluate the Brillouin zone integrals for each derived property below. This dense Brillouin zone sampling is necessary because of the large disparity in the energy scales of electrons and phonons, and directly calculating DFT phonon properties on dense k-point grids is computationally expensive and impractical. See Chapter 4 for further details on the *ab initio* calculation methods and benchmarks of the accuracy of the electron-phonon coupling (e.g. resistivity within 5% for all four metals).

5.3 Electronic Density of States and Heat Capacity

The electronic density of states (DOS) per unit volume is given by:

$$g(\varepsilon) = \int_{BZ} \frac{d\vec{k}}{(2\pi)^3} \sum_n \delta(\varepsilon - \varepsilon_{\vec{k}n}), \tag{5.2}$$

where $\varepsilon_{\vec{k}n}$ are energies of quasiparticles with band index n and wave-vector $\vec{k}$ in the Brillouin zone BZ. The density of states directly determines the electronic heat capacity and is an important factor in the electron-phonon coupling and dielectric response of hot electrons. Above, the band index n implicitly counts spinorial orbitals in our relativistic calculations, and hence we omit the explicit spin degeneracy factor.

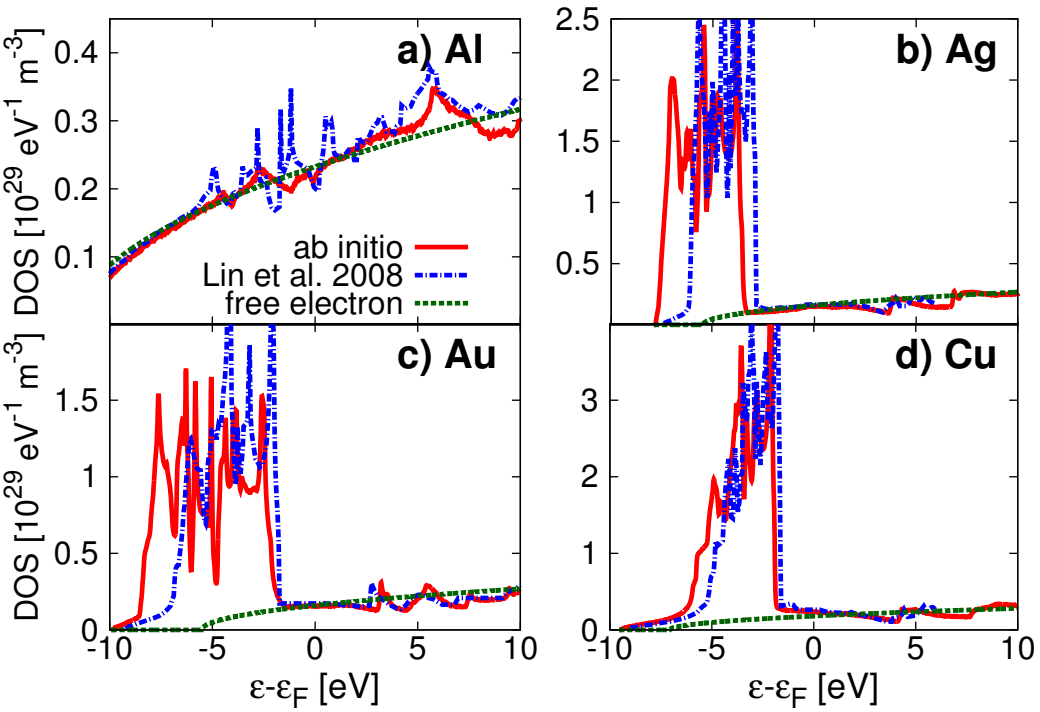

Figure 5.2: Comparison of electronic density of states of for (a) Al, (b) Ag, (c) Au and (d) Cu from our relativistic PBEsol+U calculations (*ab initio*), previous semi-local PBE DFT calculations[31] (less accurate band structure), and a free electron model.

Figure 5.2 compares the density of states predicted by our relativistic PBEsol+U method with a previous non-relativistic semi-local estimate[31] using the PBE functional,[140] as well as a free electron model $\varepsilon_{\vec{k}} = \frac{\hbar^2 k^2}{2m_e}$ for which $g(\varepsilon) = \frac{\sqrt{\varepsilon}}{2\pi^2}\left(\frac{2m_e}{\hbar^2}\right)^{3/2}$. The free electron model is a reasonable approximation for aluminum and the PBE and PBEsol+U density-functional calculations also agree reasonably well in this case. The regular 31^3 k-point grid used in Reference 31 for Brillouin zone sampling introduces the sharp artifacts in the density of states, compared to the much denser Monte Carlo sampling in our calculations with 640,000 k-points for Au, Ag, and Cu, and 1,280,000 k-points for Al.

For the noble metals, the free electron model and the density functional methods agree reasonably near the Fermi level, but differ significantly for energies ~2 eV below the Fermi level where d-bands contribute. The free electron models ignore the d-bands entirely, whereas the semi-local PBE calculations predict d-bands that are narrower and closer to the Fermi level than the PBEsol+U predictions. The U correction[103] that we employ accounts for self-interaction errors in semi-local DFT and positions the d bands in agreement with angle-resolved photoemission

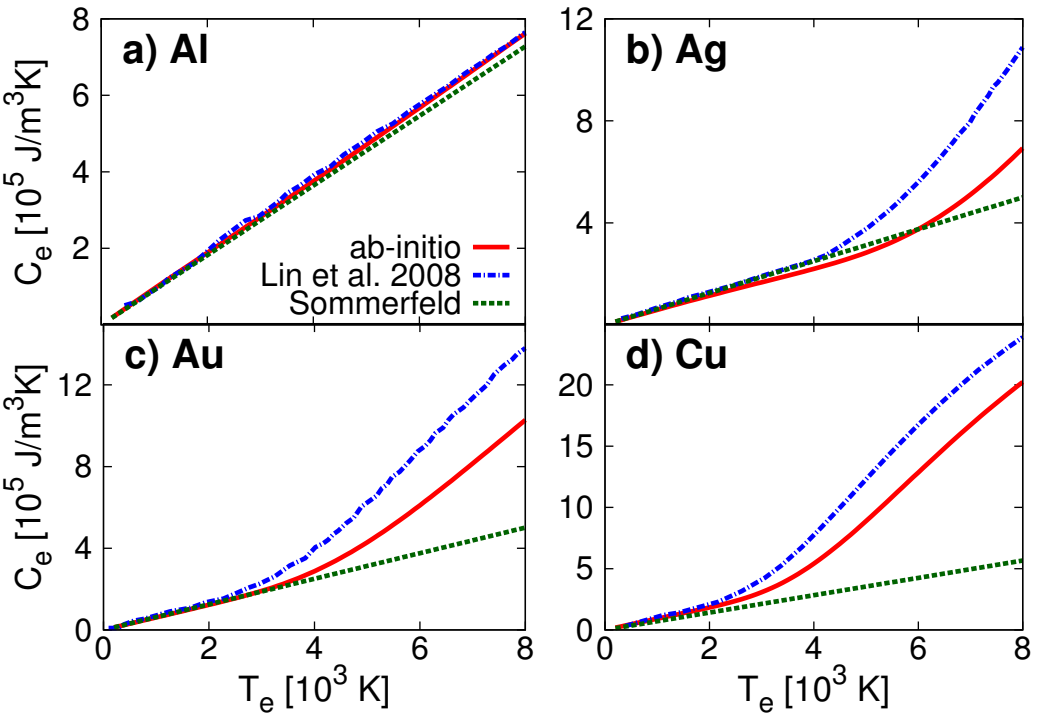

Figure 5.3: Comparison of the electronic heat capacity as a function of electron temperature, $C_e(T_e)$, for (a) Al, (b) Ag, (c) Au and (d) Cu, corresponding to the three electronic density-of-states predictions shown in Figure 5.2. The free electron Sommerfeld model underestimates C_e for noble metals at high T_e because it neglects d-band contributions, whereas previous DFT calculations[31] overestimate it because their d-bands are too close to the Fermi level.

spectroscopy measurements (to within $\sim$ 0.1 eV).[33] Additionally, the density of states in the non-relativistic PBE calculations strongly peaks at the top of the d-bands (closest to the Fermi level), whereas the density of states in our relativistic calculations is comparatively balanced between the top and middle of the d-bands due to strong spin-orbit splitting, particularly for gold. Below, we find that these inaccuracies in the density of states due to electronic structure methods previously employed for studying hot electrons propagate to the predicted electronic heat capacity and electron-phonon coupling.

The electronic heat capacity, defined as the derivative of the electronic energy per unit volume with respect to the electronic temperature (T_e), can be related to the density of states as

$$C_e(T_e) = \int_{-\infty}^{\infty} d\varepsilon g(\varepsilon)\varepsilon \frac{\partial f(\varepsilon,T_e)}{\partial T_e}, \tag{5.3}$$

where $f(\epsilon,T_e)$ is the Fermi distribution function. The term $\partial f/\partial T_e$ is sharply

peaked at the Fermi energy ε_F with a width of approximately $k_B T_e$, and therefore the heat capacity depends only on electronic states within a few $k_B T_e$ of the Fermi level. For the free electron model, Taylor expanding $g(\varepsilon)$ around ε_F and analytically integrating expression 5.3 yields the linear Sommerfeld model $C_e(T_e) = \frac{\pi^2 n_e k_B^2}{2\varepsilon_F} T_e$, which is valid for $T_e \ll T_F$ ($\sim 10^5$ K). Above, $n_e = 3\pi^2 k_F^3$, $\varepsilon_F = \frac{\hbar^2 k_F^2}{2m_e}$ and k_F are the number density, Fermi energy, and Fermi wave-vector of the free electron model, respectively.

At temperatures $T_e \ll T_F$, the electronic heat capacities are much smaller than the lattice heat capacities,[119, 126, 136] which makes it possible for laser pulses to increase T_e by $10^3 - 10^4$ Kelvin, while T_l remains relatively constant.[127, 141, 142] Figure 5.3 compares $C_e(T_e)$ from the free-electron Sommerfeld model with predictions of expression 5.3 using the density of states from PBE and PBEsol+U calculations. The free-electron Sommerfeld model is accurate at low temperatures (up to $\sim$ 2000 K) for all four metals.

With increasing T_e, $\partial f / \partial T_e$ in expression 5.3 is non-zero increasingly further away from the Fermi energy, so that deviations from the free electron density of states eventually become important. For aluminum, the density of states remains free-electron-like over a wide energy range and the Sommerfeld model remains valid even at high temperatures. For the noble metals, the increase in density of states due to d-bands causes a dramatic increase in $C_e(T_e)$ once T_e is high enough that $\partial f / \partial T_e$ becomes non-zero in the d-band energy range. Copper and gold have shallower d-bands and deviate at lower temperatures compared to silver. Additionally, the d-bands are too close to the Fermi level in the semi-local PBE calculations of Reference 31 which results in an overestimation of $C_e(T_e)$ compared to our predictions based on the more accurate relativistic PBEsol+U method.

See Appendix Chapter B for a table of the electronic heat capacity as a function of electron temperature predicted by expression 5.3

5.4 Phononic Density of States and Heat Capacity

Similarly, the phonon density of states per unit volume is given by

$$D(\varepsilon) = \int_{BZ} \frac{d\vec{q}}{(2\pi)^3} \sum_{\alpha} \delta(\varepsilon - \hbar\omega_{\vec{q}\alpha}), \tag{5.4}$$

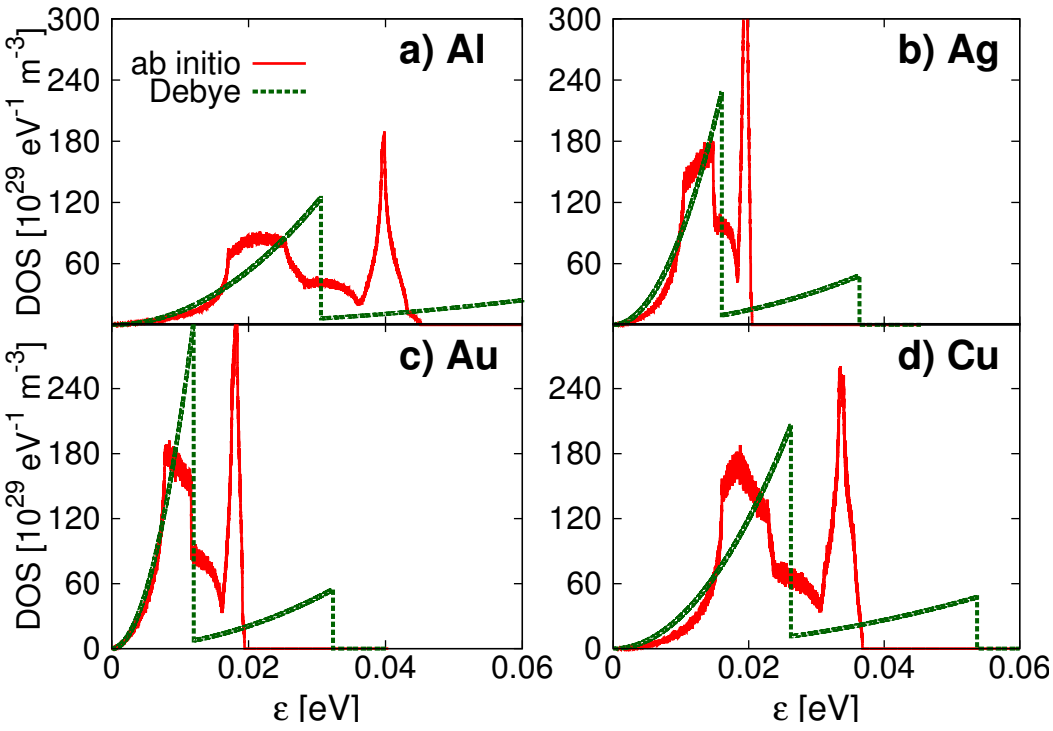

Figure 5.4: Comparison of *ab initio* phonon density of states and the Debye model for (a) Al, (b) Ag, (c) Au, and (d) Cu.

where $\hbar\omega_{\vec{q}\alpha}$ is the energy of a phonon with polarization index α and wave-vector $\vec{q}$. The phonon density of states directly determines the lattice heat capacity,

$$C_l(T_l) = \int_0^\infty d\varepsilon D(\varepsilon)\varepsilon\frac{\partial n(\varepsilon,T_l)}{\partial T_l}, \tag{5.5}$$

where $n(\varepsilon,T_l)$ is the Bose occupation factor.

Within the Debye model, the phonon energies are approximated by an isotropic linear dispersion relation $\omega_{\vec{q}\alpha} = v_\alpha q$ up to a maximum Debye wave-vector q_D chosen to conserve the number of phonon modes per unit volume. This model yields the analytical phonon density of states, $D(\varepsilon) = \frac{\varepsilon^2}{(2\pi^2)}\sum_\alpha \theta(\hbar q_D v_\alpha - \varepsilon)/(\hbar v_\alpha)^3$, where $v_\alpha = \{v_L, v_T, v_T\}$ are the speeds of sound for the one longitudinal and two degenerate transverse phonon modes of the face-centered cubic metals considered here.[116]

Figure 5.4 compares the *ab initio* phonon density of states with the Debye model predictions, and shows that the Debye model is a good approximation for the density of states only up to 0.01 eV. However, Figure 5.5 shows that the corresponding predictions for the lattice heat capacities are very similar, rapidly approaching the equipartition theorem prediction of $C_l = 3k_B/\Omega$ at high temperatures, which is in-

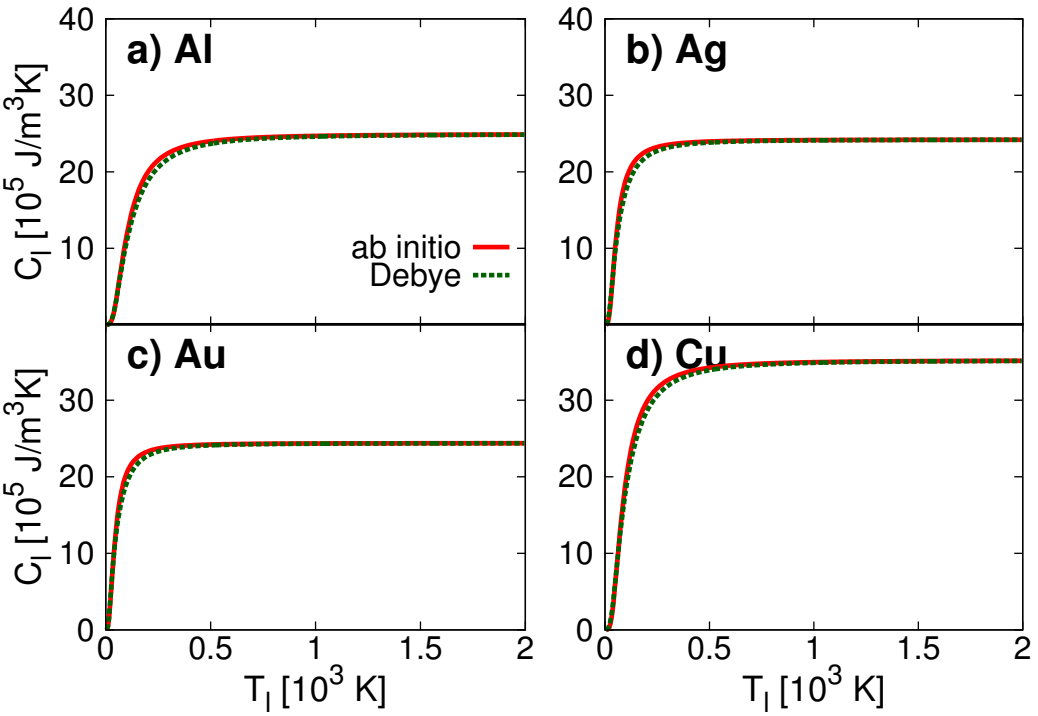

Figure 5.5: Comparison of *ab initio* and Debye model predictions of the lattice heat capacity as a function of lattice temperature, $C_l(T_l)$, for (a) Al, (b) Ag, (c) Au, and (d) Cu. Despite large differences in the density of states (Figure 5.4), the predicted lattice heat capacities of the two models agree within 10%.

sensitive to details in the phonon density of states. In fact, the largest deviations of the Debye model heat capacity are below 100 K and deviate less than 10% from the *ab initio* predictions for all four metals. We therefore find that a simple Debye model of the phonons is adequate for predicting the lattice heat capacity, in contrast to the remaining quantities we consider below which are highly sensitive to details of the phonons and their coupling to the electrons.

5.5 Electron-phonon Matrix Element and Coupling

In Section 5.3 we showed that the electronic heat capacity, which determines the initial temperature that the hot electrons equilibrate to, is sensitive to electronic structure especially in noble metals at high T_e where d-bands contribute. Now we analyze the electron-phonon coupling which determines the subsequent thermalization of the hot electrons with the lattice. We show that details in the *ab initio* electron-phonon matrix elements also play a significant role, in addition to the electronic band structure, and compare previous semi-empirical estimates of the temperature dependent phonon coupling to our direct *ab initio* calculations.

The rate of energy transfer per unit volume from electrons at temperature T_e to the lattice at temperature T_l via electron-phonon scattering is given by Fermi's golden rule as

$$\frac{dE}{dt} \equiv G(T_e)(T_e - T_l) \tag{5.6}$$

$$= \frac{2\pi}{\hbar} \int_{BZ} \frac{\Omega d\vec{k} d\vec{k}'}{(2\pi)^6} \sum_{nn'\alpha} \delta(\varepsilon_{\vec{k}'n'} - \varepsilon_{\vec{k}n} - \hbar\omega_{\vec{k}'-\vec{k},\alpha}) \times \hbar\omega_{\vec{k}'-\vec{k},\alpha} \left| g^{\vec{k}'-\vec{k},\alpha}_{\vec{k}'n',\vec{k}n} \right|^2 S_{T_e,T_l}(\varepsilon_{\vec{k}n}, \varepsilon_{\vec{k}'n'}, \hbar\omega_{\vec{k}'-\vec{k},\alpha}) \tag{5.7}$$

with

$$S_{T_e,T_l}(\varepsilon, \varepsilon', \hbar\omega_{ph}) \equiv f(\varepsilon, T_e) n(\hbar\omega_{ph}, T_l)(1 - f(\varepsilon', T_e)) - (1 - f(\varepsilon, T_e))(1 + n(\hbar\omega_{ph}, T_l)) f(\varepsilon', T_e). \tag{5.8}$$

Here, Ω is the unit cell volume, $\hbar\omega_{\vec{q}\alpha}$ is the energy of a phonon with wave-vector $\vec{q} = \vec{k}' - \vec{k}$ and polarization index α, and $g^{\vec{k}'-\vec{k},\alpha}_{\vec{k}'n',\vec{k}n}$ is the electron-phonon matrix element coupling this phonon to electronic states indexed by $\vec{k}n$ and $\vec{k}'n'$.

Above, S is the difference between the product of occupation factors for the forward and reverse directions of the electron-phonon scattering process $\vec{k}n + \vec{q}\alpha \rightarrow \vec{k}'n'$, with $f(\varepsilon, T_e)$ and $n(\hbar\omega, T_l)$ being the Fermi and Bose distribution function for the electrons and phonons, respectively. Using the fact that $S_{T_e,T_l} = 0$ for an energy-conserving process, $\varepsilon + \hbar\omega_{ph} = \varepsilon'$, by detailed balance, we can write the electron-phonon coupling coefficient as

$$G(T_e) = \frac{2\pi}{\hbar} \int_{BZ} \frac{\Omega d\vec{k} d\vec{k}'}{(2\pi)^6} \sum_{nn'\alpha} \delta(\varepsilon_{\vec{k}'n'} - \varepsilon_{\vec{k}n} - \hbar\omega_{\vec{k}'-\vec{k},\alpha}) \times \hbar\omega_{\vec{k}'-\vec{k},\alpha} \left| g^{\vec{k}'-\vec{k},\alpha}_{\vec{k}'n',\vec{k}n} \right|^2 (f(\varepsilon_{\vec{k}n}, T_e) - f(\varepsilon_{\vec{k}'n'}, T_e)) \times \frac{n(\hbar\omega_{\vec{k}'-\vec{k},\alpha}, T_e) - n(\hbar\omega_{\vec{k}'-\vec{k},\alpha}, T_l)}{T_e - T_l}. \tag{5.9}$$

This general form for *ab initio* electronic and phononic states is analogous to previous single-band / free electron theories of the electron-phonon coupling coefficient; see for example the derivation by Allen et al.[143]

The direct *ab initio* evaluation of $G(T_e)$ using expression 5.9 requires a six-dimensional integral over electron-phonon matrix elements from DFT with very fine k-point

grids that can resolve both electronic and phononic energy scales. This is impractical without the recently-developed Wannier interpolation and Monte Carlo sampling methods for these matrix elements,[34, 107] and therefore our results are the first fully *ab initio* predictions of $G(T_e)$. See Appendix Chapter B for a table of the electron-phonon coupling factor as a function of electron temperature predicted by expression 5.9.

Previous theoretical estimates of $G(T_e)$ are semi-empirical, combining DFT electronic structure with empirical models for the phonon coupling. For example, Wang et al.[144] assume that the electron-phonon matrix elements averaged over scattering angles are independent of energy and that the phonon energies are smaller than $k_B T_e$, and then approximate the electron-phonon coupling coefficient as

$$G(T_e) \approx \frac{\pi k_B}{\hbar g(\varepsilon_F)} \lambda \langle (\hbar\omega)^2 \rangle \int_{-\infty}^{\infty} d\varepsilon g^2(\varepsilon) \frac{-\partial f(\varepsilon, T_e)}{\partial \varepsilon}, \tag{5.10}$$

where λ is the electron-phonon mass enhancement parameter and $\langle (\hbar\omega)^2 \rangle$ is the second moment of the phonon spectrum.[31, 117, 145] Lin et al.[31] treat $\lambda \langle (\hbar\omega)^2 \rangle$ as an empirical parameter calibrated to experimental values of G at low electron temperatures obtained from thermoreflectance measurements, and extrapolate it to higher electron temperatures using expression 5.10. See Refs. 144 and 31 for more details.

For clarity, we motivate here a simpler derivation of an expression of the form of equation 5.10 from the general form (equation 5.9). First, making the approximation $\hbar\omega_{\vec{q}\alpha} \ll T_e$ (which is reasonably valid for T_e above room temperature) allows us to approximate the difference between the electron occupation factors in the second line of equation 5.9 by $\hbar\omega_{\vec{q}\alpha} \partial f / \partial \varepsilon$ (using energy conservation). Additionally, for $T_e \gg T_l$, the third line of equation 5.9 simplifies to $k_B/(\hbar\omega_{\vec{k}'-\vec{k},\alpha})$. With no other approximations, we can then rearrange equation 5.9 to collect contributions by initial electron energy,

$$G(T_e) \approx \frac{\pi k_B}{\hbar g(\varepsilon_F)} \int_{-\infty}^{\infty} d\varepsilon h(\varepsilon) g^2(\varepsilon) \frac{-\partial f(\varepsilon, T_e)}{\partial \varepsilon} \tag{5.11}$$

with

$$h(\varepsilon) \equiv \frac{2g(\varepsilon_F)}{g^2(\varepsilon)} \int_{BZ} \frac{\Omega d\vec{k} d\vec{k}'}{(2\pi)^6} \sum_{nn'\alpha} \delta(\varepsilon - \varepsilon_{\vec{k}n}) \times \delta(\varepsilon_{\vec{k}'n'} - \varepsilon_{\vec{k}n} - \hbar\omega_{\vec{k}'-\vec{k},\alpha}) \hbar\omega_{\vec{k}'-\vec{k},\alpha} \left| g^{\vec{k}'-\vec{k},\alpha}_{\vec{k}'n',\vec{k}n} \right|^2. \tag{5.12}$$

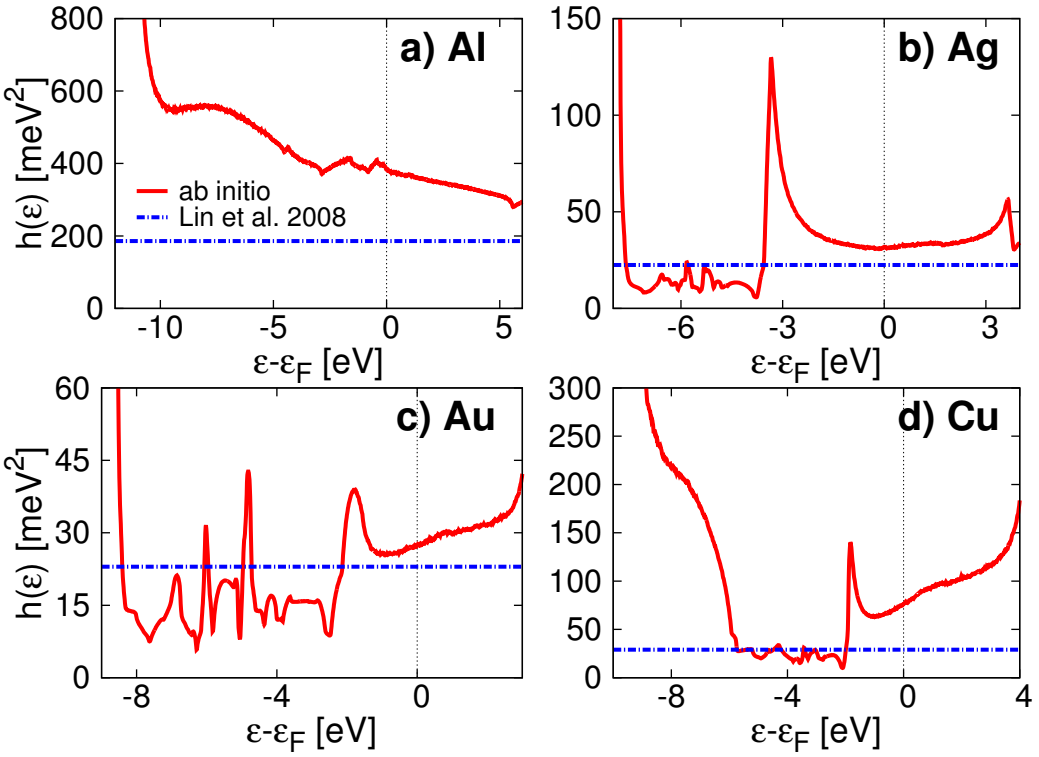

Figure 5.6: Energy-resolved electron-phonon coupling strength $h(\varepsilon)$, defined by expression 5.12, for (a) Al, (b) Ag, (c) Au, (d) Cu. For the noble metals, $h(\epsilon_F)$ is substantially larger than its value in the d-bands, which causes previous semi-empirical estimates[31] using a constant $h(\varepsilon)$ to overestimate the electron-phonon coupling ($G(T_e)$) at $T_e \sim 3000$ K, as shown in Figure 5.7.

Comparing this with expression 5.10, we can see that the the primary approximation in previous semi-empirical estimates[31, 144] is the replacement of $h(\varepsilon)$ by an energy-independent constant $\lambda\langle(\hbar\omega)^2\rangle$, used as an empirical parameter.

Figure 5.6 compares *ab initio* calculations of this energy-resolved electron-phonon coupling strength, $h(\varepsilon)$, with previous empirical estimates of $\lambda\langle(\hbar\omega)^2\rangle$, and Figure 5.7 compares the resulting temperature dependence of the electron-phonon coupling, $G(T_e)$, from the *ab initio* (expression 5.9) and semi-empirical methods (expression 5.10). For noble metals, $G(T_e)$ increases sharply beyond $T_e \sim 3000$ K because of the large density of states in the d-bands. However, $h(\varepsilon)$ is smaller by a factor of $2-3$ in the d-bands compared to near the Fermi level. Therefore, assuming $h(\varepsilon)$ to be an empirical constant equal to its value at the fermi level[31, 32] results in a significant overestimate of the contributions of the d-bands to $G(T_e)$ at high T_e, compared to the direct *ab initio* calculations. Additionally, the shallowness of the d-bands in the semi-local PBE band structure used in Reference 31 lowers

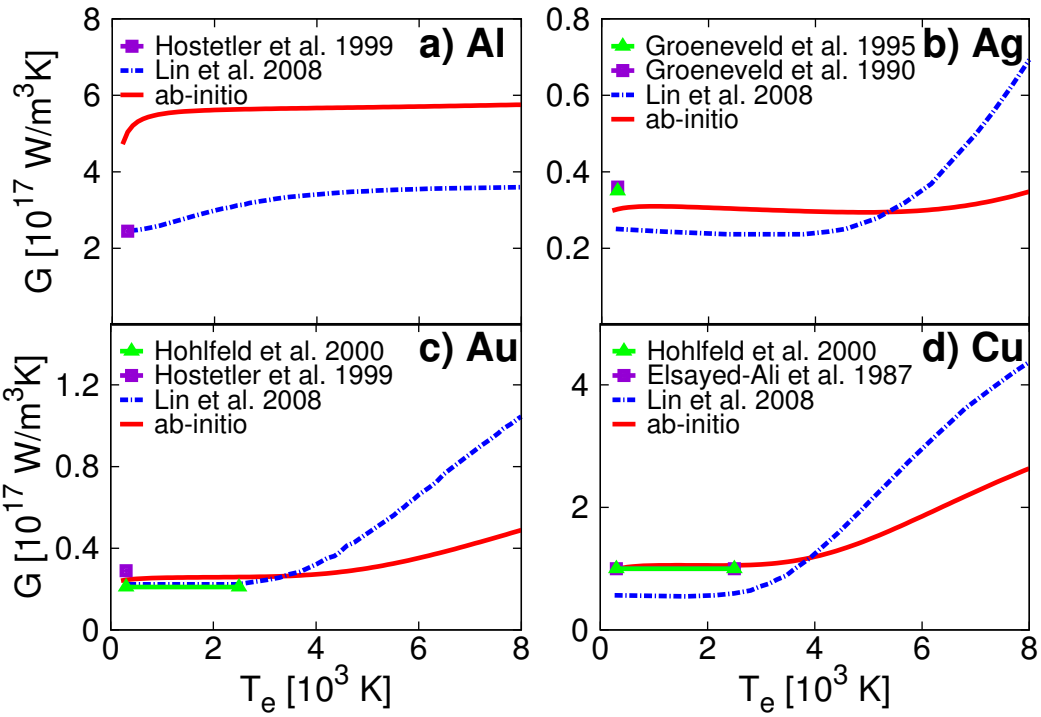

Figure 5.7: Comparison of predictions of the the electron-phonon coupling strength as a function of electron temperature, $G(T_e)$, for (a) Al, (b) Ag, (c) Au and (d) Cu, with experimental measurements where available.[124, 130, 131, 146, 147] The DFT-based semi-empirical predictions of Lin et al.[31] overestimate the coupling for noble metals at high temperatures because they assume an energy-independent electron-phonon coupling strength (Figure 5.6) and neglect the weaker phonon coupling of d-bands compared to the conduction band. The experimental results (and hence the semi-empirical predictions) for aluminum underestimate electron-phonon coupling because they include the effect of competing electron-electron thermalization which happens on the same time scale.

the onset temperature of the increase in $G(T_e)$, and results in further overestimation compared to our *ab initio* predictions.

The *ab initio* predictions agree very well with the empirical measurements of $G(T_e)$ available at lower temperatures for noble metals.[124, 130, 131, 146, 147] In fact, the semi-empirical calculation based on $\lambda\langle(\hbar\omega)^2\rangle$ underestimates the room temperature electron-phonon coupling for these metals; the significant overestimation of $G(T_e)$ seen in Figure 5.7 is in despite of this partial cancellation of error. This shows the importance of *ab initio* electron-phonon matrix elements in calculating the coupling between hot electrons and the lattice.

Experimental measurements of the electron-phonon coupling in noble metals are

reliable because of the reasonably clear separation between a fast electron-electron thermalization rise followed by a slower electron-phonon decay in the optical transient signal. In aluminum, these time scales significantly overlap making an unambiguous experimental determination of G difficult. Consequently, the value of G for Al is not well agreed upon.[148] For example, in Reference 146, measurements showed no fast transient free-electron spike and G was extracted from the lattice temperature variation instead. However, the measured rate for the lattice temperature rise includes competing contributions from electron-electron and electron-phonon thermalization; attributing the entire rate to electron-phonon coupling only provides a lower bound for G. Indeed, Figure 5.7(a) shows that this experimental estimate[146] and its phenomenological extension to higher T_e[31] significantly underestimate our *ab initio* predictions by almost a factor of two. Note that density functional theory is highly reliable for the mostly free-electron-like band structure of aluminum, and the *ab initio* electron-phonon matrix elements are accurate to within 5%.[34] We therefore conclude that electron-electron thermalization is only about two times faster then electron-phonon thermalization in aluminum, causing the significant discrepancy in experimental measurements. This further underscores the importance of *ab initio* calculations over phenomenological models of electron-phonon coupling.

5.6 Temperature Dependent Dielectric function

The final ingredient for a complete *ab initio* description of hot electron relaxation dynamics is the electron-temperature-dependent dielectric function of the material. In Chapter 4 we showed that we could predict the imaginary part of the dielectric function $\mathrm{Im}\epsilon(\omega)$ of plasmonic metals in quantitative agreement with ellipsometric measurements for a wide range of frequencies by accounting for the three dominant contributions,

$$\mathrm{Im}\epsilon(\omega) = \frac{4\pi\sigma_0}{\omega(1+\omega^2\tau^2)} + \mathrm{Im}\epsilon_{\mathrm{direct}}(\omega) + \mathrm{Im}\epsilon_{\mathrm{phonon}}(\omega). \tag{5.13}$$

Here we focus on electron temperature dependence of these contributions; see Chapter 4 for a detailed description of this expression.

The first term of expression 5.13 accounts for the Drude response of the metal due to free carriers near the Fermi level, with the zero-frequency conductivity σ_0 and momentum relaxation time τ calculated using the linearized Boltzmann equation with *ab initio* collision integrals. The second and third terms of expression 5.13,

derived in Appendix Chapter A and discussed in Chapter 4,

$$\mathrm{Im}\epsilon_{\mathrm{direct}}(\omega) = \frac{4\pi^2 e^2}{m_e^2\omega^2}\int_{BZ}\frac{d\vec{q}}{(2\pi)^3}\sum_{n'n}(f_{\vec{q}n} - f_{\vec{q}n'})\delta(\varepsilon_{\vec{q}n'} - \varepsilon_{\vec{q}n} - \hbar\omega)\left|\hat{\lambda}\cdot\langle\vec{p}\rangle_{n'n}^{\vec{q}}\right|^2 \tag{5.14}$$

and

$$\begin{aligned}\mathrm{Im}\epsilon_{\mathrm{phonon}}(\omega) = \frac{4\pi^2 e^2}{m_e^2\omega^2}\int_{BZ}\frac{d\vec{q}'d\vec{q}}{(2\pi)^6}\sum_{n'n\alpha\pm}(f_{\vec{q}n} - f_{\vec{q}'n'}) \\ \times\left(n_{\vec{q}'-\vec{q},\alpha} + \frac{1}{2} \mp \frac{1}{2}\right)\delta(\varepsilon_{\vec{q}'n'} - \varepsilon_{\vec{q}n} - \hbar\omega \mp \hbar\omega_{\vec{q}'-\vec{q},\alpha}) \\ \times\left|\hat{\lambda}\cdot\sum_{n_1}\left(\frac{g_{\vec{q}'n',\vec{q}n_1}^{\vec{q}'-\vec{q},\alpha}\langle\vec{p}\rangle_{n_1 n}^{\vec{q}}}{\varepsilon_{\vec{q}n_1} - \varepsilon_{\vec{q}n} - \hbar\omega + i\eta} + \frac{\langle\vec{p}\rangle_{n'n_1}^{\vec{q}'}g_{\vec{q}'n_1,\vec{q}n}^{\vec{q}'-\vec{q},\alpha}}{\varepsilon_{\vec{q}'n_1} - \varepsilon_{\vec{q}n} \mp \hbar\omega_{\vec{q}'-\vec{q},\alpha} + i\eta}\right)\right|^2,\end{aligned} \tag{5.15}$$

capture the contributions due to direct interband excitations and phonon-assisted intraband excitations, respectively. Here $\langle\vec{p}\rangle_{n'n}^{\vec{q}}$ are matrix elements of the momentum operator, $\hat{\lambda}$ is the electric field direction (results are isotropic for crystals with cubic symmetry), and all remaining electron and phonon properties are exactly as described previously in Chapter 4. The energy-conserving delta functions are replaced by a Lorentzians of width equal to the sum of initial and final electron linewidths, to account for the finite lifetime of the quasiparticles.

The dielectric function calculated using expressions 5.13-5.15 depends on the electron temperature in two ways. First, the electron occupations $f_{\vec{q}n}$ directly depend on electron temperature. Second, the phase-space for electron-electron scattering increases with electron temperature, which increases the momentum relaxation rate (τ^{-1}) in the first Drude term of expression 5.13 and the Lorentzian broadening in the energy conserving δ-function in equations 5.14 and 5.15.

We calculate *ab initio* electron linewidths using Fermi golden rule calculations for electron-electron and electron-phonon scattering at room temperature, as detailed in Chapter 4. Because these calculations are computationally expensive and difficult to repeat for several electron temperatures, we instead use the *ab initio* linewidths at room temperature with an analytical correction for the T_e dependence. The electron-phonon scattering rate depends on the lattice temperature, but is approximately independent of T_e because the phase space for scattering is determined primarily by the electronic density of states and electron-phonon matrix elements, which depend strongly on the electron energies but not on the occupation factors or electron temperature. The phase space for electron-electron scattering, on the other hand,

Table 5.1: Parameters to describe the change in dielectric function with electron temperature using expression 5.17, extracted from fits to *ab initio* calculations. The energies and effective masses for the parabolic band approximation for the $d \rightarrow s$ transition in noble metals are indicated Figure 5.15(a).

	Al	Ag	Au	Cu
Physical constants:				
ω_p [eV/$\hbar$]	15.8	8.98	9.01	10.8
τ^{-1} [eV/$\hbar$]	0.0911	0.0175	0.0240	0.0268
Fits to *ab initio* calculations:				
D_e [eV^{-1}]	0.017	0.021	0.016	0.020
A_0 [eV$^{3/2}$]	-	70	22	90
ε_c [eV]	-	0.31	0.96	0.98
ε_0 [eV]	-	3.36	1.25	1.05
m_v^*/m_c^*	-	5.4	3.4	16.1

depends on the occupation factors and electron temperature because an electron at an energy far from the Fermi level can scatter with electrons close to the Fermi level. The variation of this phase-space with temperature is primarily due to the change in occupation of states near the Fermi level, and we can therefore estimate this effect in plasmonic metals using a free electron model.

Within a free electron model, the phase-space for electron-electron scattering grows quadratically with energy relative to the Fermi level, resulting in scattering rates $\propto (\varepsilon - \varepsilon_F)^2$ at zero electron temperatures, as is well-known.[123, 149] We can extend these derivations to finite electron temperature to show (see Appendix Chapter C for derivation) that the energy and temperature-dependent electron-electron scattering rate

$$\tau_{ee}^{-1}(\varepsilon, T_e) \approx \frac{D_e}{\hbar}[(\varepsilon - \varepsilon_F)^2 + (\pi k_B T_e)^2] \tag{5.16}$$

for $|\varepsilon - \varepsilon_F| \ll \varepsilon_F$ and $T_e \ll \varepsilon_F/k_B$. Within the free electron model, the constant of proportionality $D_e = \frac{m_e e^4}{4\pi\hbar^2(\epsilon_b^0)^2\varepsilon_S^{3/2}\sqrt{\varepsilon_F}}\left(\frac{\sqrt{4\varepsilon_F\varepsilon_S}}{4\varepsilon_F+\varepsilon_S} + \tan^{-1}\sqrt{\frac{4\varepsilon_F}{\varepsilon_S}}\right)$, where the background dielectric constant ϵ_b^0 and the Thomas-Fermi screening energy scale ε_S are typically treated as empirical parameters.[123] Here, we extract D_e by fitting (5.16) to the *ab initio* electron-electron scattering rates at room temperature T_0.[34] The resulting fit parameters are shown in Table 5.1. We then estimate the total scattering rates at other temperatures by adding $(D_e/\hbar)(\pi k_B)^2(T_e^2 - T_0^2)$ to the total *ab initio* results (including electron-phonon scattering) at T_0.

Finally, we use the Kramers-Kronig relations to calculate $\mathrm{Re}(\epsilon(\omega, T_e))$ from $\mathrm{Im}(\epsilon(\omega, T_e))$. Given the dearth of published temperature-dependent dielectric functions in the lit-

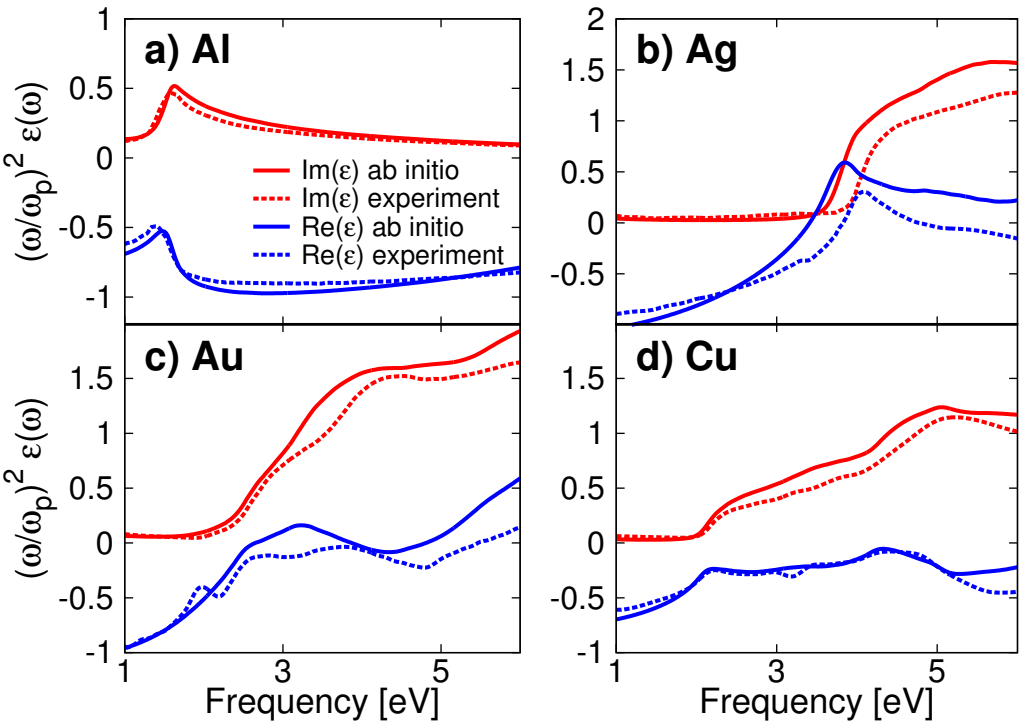

Figure 5.8: Predicted complex dielectric functions for (a) Al, (b) Ag, (c) Au, (d) Cu at room temperature (300 K) compared with ellipsometry measurements.[36] The y-axis is scaled by ω^2/ω_p^2 in order to represent features at different frequencies such as the Drude pole and the interband response on the same scale.

erature, we have published detailed tables of our *ab initio* predictions for electron temperatures up to 8000 K, and spanning frequencies from the infrared to the ultraviolet, in the supplementary information of Reference [35].

Figure 5.8 compares the predicted dielectric functions with ellipsometry measurements[36] for a range of frequencies spanning from near-infrared to ultraviolet. Note that we scale the y-axis by $(\omega/\omega_p)^2$, where the free-electron plasma frequency $\omega_p = \sqrt{4\pi e^2 n_e/m_e}$, in order to display features at all frequencies on the same scale. We find excellent agreement for aluminum within 10% of experiment over the entire frequency range, including the peak around 1.6 eV due to an interband transition. The agreement is reasonable for noble metals with a typical error within 20%, but with a larger error $\sim$ 50% for certain features in the interband $d \rightarrow s$ transitions due to inaccuracies in the d-band positions predicted by DFT (especially for silver).

Figures 5.9, 5.11 and 5.13 show the *ab initio* dielectric functions at electron temperatures of 400, 1000, and 5000 K compared to those at 300 K. As electron temperature increases, features in the dielectric functions become increasingly broad. Note

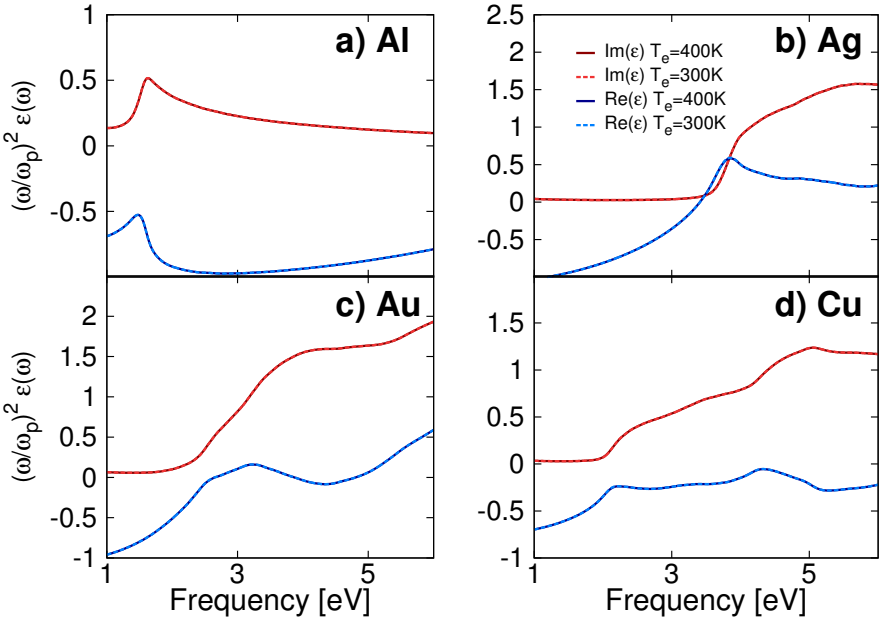

Figure 5.9: *Ab initio* predicted complex dielectric functions for (a) Al, (b) Ag, (c) Au, (d) Cu at 400 K compared to 300 K with the same scaling as in Figure 5.8.

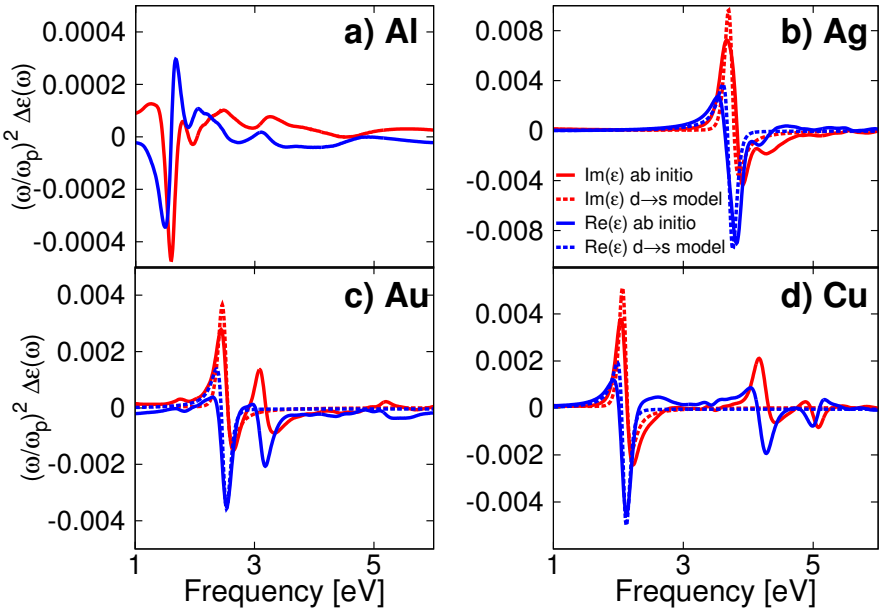

Figure 5.10: Change in the predicted complex dielectric function for (a) Al, (b) Ag, (c) Au, (d) Cu from room temperature (300 K) to electron temperature T_e = 400 K (with the lattice remaining at room temperature) with the same scaling as in Figure 5.8. The analytical model given by expression 5.17, with fit parameters summarized in Table 5.1, captures the essential features of the *ab initio* data for noble metals at lower temperatures, but misses the contributions of broadening due to electron-electron scattering at higher temperatures.

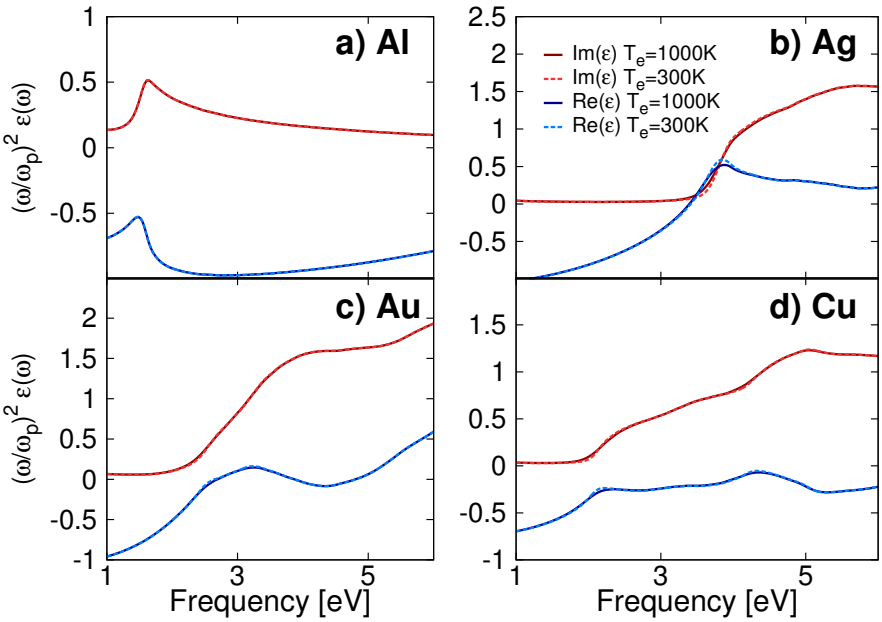

Figure 5.11: *Ab initio* predicted complex dielectric functions for (a) Al, (b) Ag, (c) Au, (d) Cu at 1000 K and 300 K with the same scaling as in Figure 5.8.

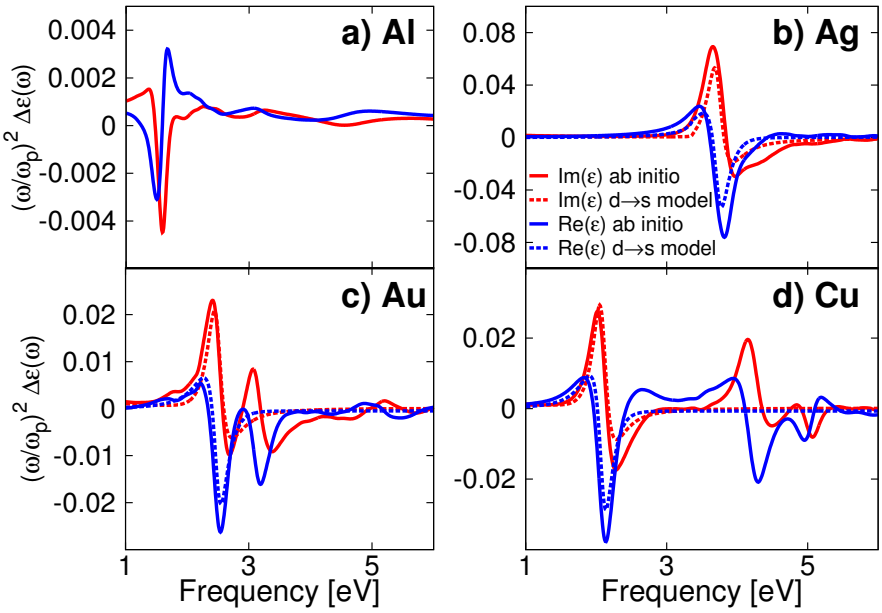

Figure 5.12: Change in the predicted complex dielectric function for (a) Al, (b) Ag, (c) Au, (d) Cu from room temperature (300 K) to electron temperature T_e = 1000 K (with the lattice remaining at room temperature) with the same scaling as in Figure 5.8.

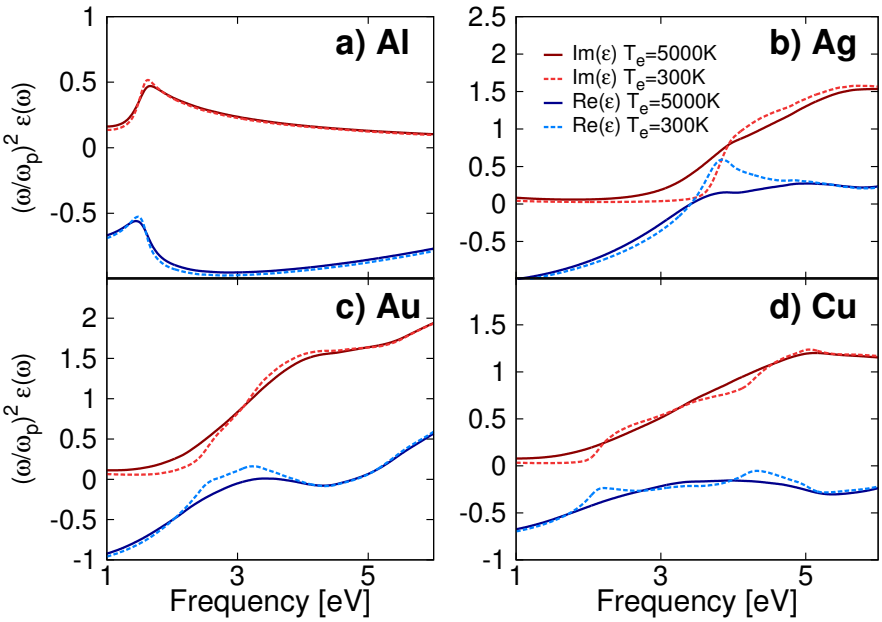

Figure 5.13: *Ab initio* predicted complex dielectric functions for (a) Al, (b) Ag, (c) Au, (d) Cu at 5000 K compared to 300 K with the same scaling as in Figure 5.8.

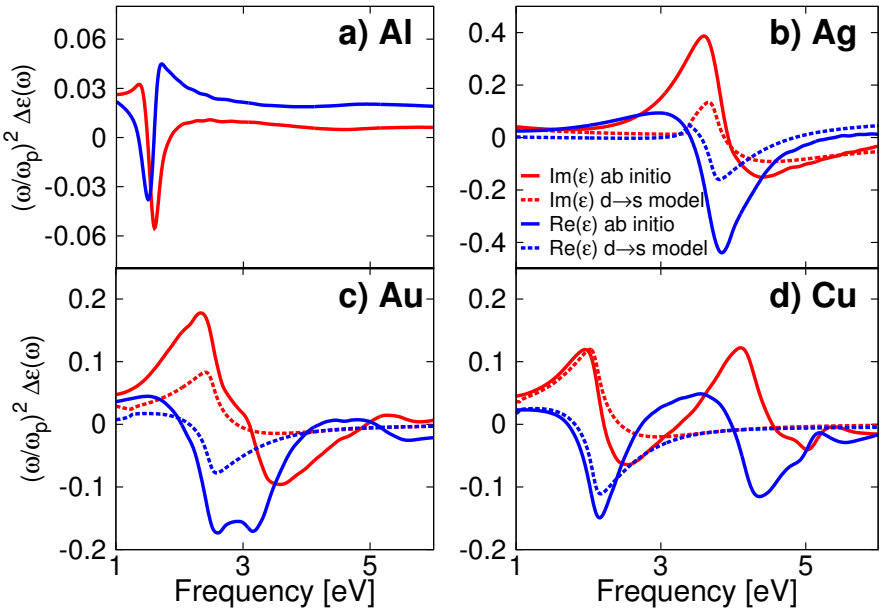

Figure 5.14: Change in the predicted complex dielectric function for (a) Al, (b) Ag, (c) Au, (d) Cu from room temperature (300 K) to electron temperature T_e = 5000 K (with the lattice remaining at room temperature) with the same scaling as in Figure 5.8.

that the change in dielectric function (relative to 300 K) is not noticeable on the scale of the dielectric functions for all but the highest temperatures; we therefore directly plot the change of the complex dielectric function upon increasing the electron temperature T_e from room temperature to 400 K, 1000 K and 5000 K while the lattice remains at room temperature in Figures 5.10, 5.12, and 5.14, respectively. For all four metals, the response from infrared to ultraviolet frequencies is dominated by 'sharp' features due to interband transitions that broaden with increasing temperature, rather than a change in the Drude response which would be the only contribution in a free-electron model.

The strongest temperature dependence in noble metals results from transitions between the highest occupied d-band to the Fermi level near the L point, as shown in Figure 5.15(a). Assuming a parabolic dispersion and a constant transition matrix element, and accounting for the change in the Drude response, this temperature dependence can be modeled as[32, 150]

$$\Delta\epsilon(\omega) = -\Delta\left[\frac{\omega_p^2}{\omega(\omega + i(\tau^{-1} + \frac{D_e}{\hbar}(\pi k_B T_e)^2))} + \mathcal{K}\frac{A_0}{(\hbar\omega)^2}\int_{-\varepsilon_c}^{\infty}\frac{d\varepsilon(1 - f(\varepsilon, T_e))}{\sqrt{\frac{m_v^*}{m_c^*}(\hbar\omega - (\varepsilon + \varepsilon_0 + \varepsilon_c)) - (\varepsilon + \varepsilon_c)}}\right]. \quad (5.17)$$

The denominator in the second term captures the joint density of states for transitions between the bands, and the numerator counts unoccupied states near the Fermi level, which introduces the temperature dependence. Above, $\mathcal{K}$ fills in the real part of the dielectric function, given the imaginary part using the Kramers-Kronig relation.

Table 5.1 lists the parameters for the parabolic band approximation obtained from the *ab initio* band structures. Figure 5.10 shows that this approximation captures the correct shape of $\Delta\varepsilon(\omega)$ for small changes in T_e. However, this model underestimates the T_e dependence for higher electron temperatures because it ignores the quadratic increase in broadening of the electronic states due to increased electron-electron scattering, as Figures 5.12 and 5.14 show. Aluminum exhibits a sharp change in the dielectric function around $\hbar\omega \approx 1.5$ eV, which results from several transitions to/from the Fermi level near the W point as Figure 5.15(b) shows. Additionally, two of the involved bands are not parabolic, making it difficult to construct a simple model like expression 5.17. Therefore, simplified models are adequate for qualitative analysis of lower temperature excitation experiments in noble met-

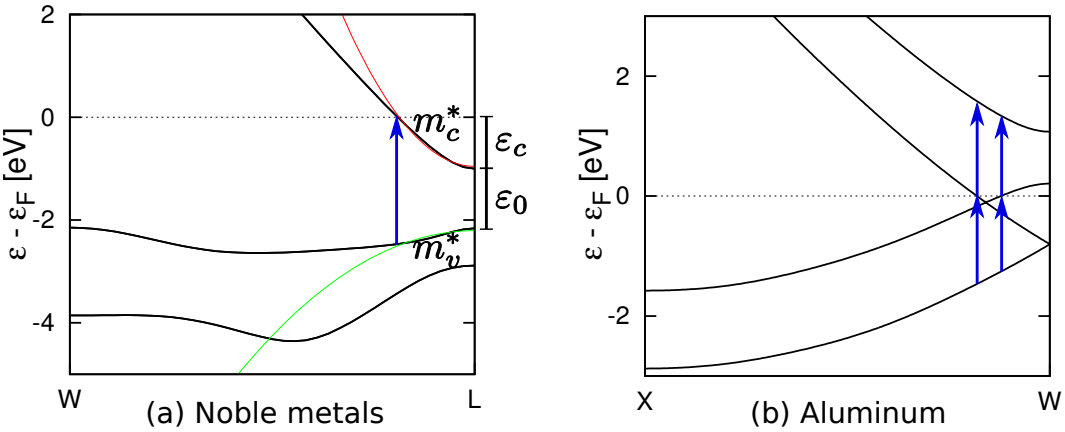

Figure 5.15: Critical interband transitions determining the 'sharp' features in the dielectric function change for (a) noble metals (gold shown; similar shapes for silver and copper) and (b) aluminum. A parabolic band model around the L point (parameters in Table 5.1) approximates the critical transition in noble metals. This is difficult in aluminum because of four such transitions in a narrow energy range $\approx 1.3 - 1.6$ eV.

als,[32] but *ab initio* dielectric functions are necessary for a quantitative analysis of higher temperature experiments and a wider range of materials and probe frequencies.

5.7 Conclusions

In this chapter we presented *Ab initio* calculations of electron-phonon coupling, electron and lattice heat capacities, and dielectric functions and show qualitative differences from free-electron and previous semi-empirical estimates because of the substantial energy dependence of electron-phonon matrix elements and electronic density of states. These changes are particularly important for gold and copper at transient electron temperatures greater than 2000 K because of the change in occupations of the *d*-bands situated ~ 2 eV below the Fermi level in these metals. Our *ab initio* temperature dependent dielectric function is, to our knowledge, the first of its kind and a great improvement over the free-electron based models and parabolic band approximations that are commonly used. We show that while simple models can account for some of the qualitative features of the change in dielectric function for small changes in temperature, *ab initio* treatment is essential to quantitatively account for the complete frequency and temperature dependence, including effects such as carrier linewidth broadening and transitions between multiple non-parabolic bands. The temperature dependence of the optical response is, in particular, important for a wide range of applications beyond understanding ultrafast transient

measurements.

This work has direct implications for analysis of experimental pump-probe studies of metal nanostructures, such as those discussed in Chapter 6. The *ab initio* material properties predicted in this Chapter allow a parameter-free description of the spectra obtained in transient absorption studies since we implicitly account for all the microscopic processes in the non-equilibrium dynamics of electrons in plasmonic metals.

Chapter 6

EXPERIMENTAL AND *AB INITIO* ULTRAFAST CARRIER RELAXATION IN PLASMONIC NANOPARTICLES

6.1 Motivation and Background

Plasmonic hot carriers provide tremendous opportunities for combining efficient light capture with energy conversion and catalyst activity at the nano scale.[83, 151, 152] Hot carriers can be used to directly drive chemical reactions at the metal surface, or they can be transferred to a semiconductor for use in photovoltaics[153, 154] and photoelectrochemical systems.[155, 156] Dynamics of hot carriers are typically studied via ultrafast pump-probe measurements of plasmonic nanostructures.[122–128, 157] Ultrafast transient absorption measurements have been used to investigate microscopic processes on femtosecond time scales, such as plasmon decay and hot electron relaxation through electron-electron, electron-surface, and electron-phonon scattering.[17, 119, 123, 130, 131, 158–162]

In ultrafast transient absorption measurements on metals, a laser pulse, referred to as the pump pulse, is used to excite a plasmon on the surface of the metal (see Figure 6.1). The plasmon can then decay via absorption by an electron and produce

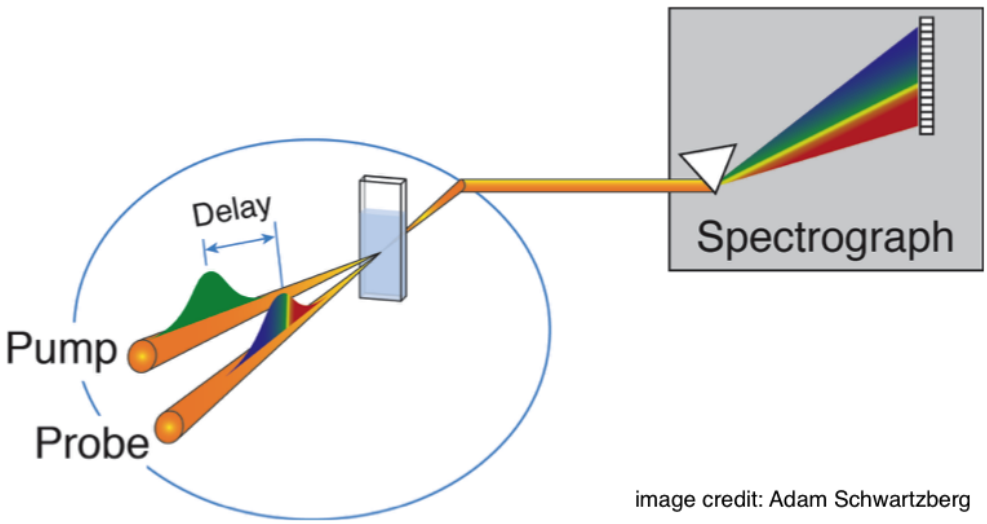

Figure 6.1: Ultrafast transient absorption measurement setup. A pump pulse excites the sample. A white light probe pulse is delayed with respect to the pump pulse and collected by a spectrometer. By varying the pump-probe delay time, the absorption or extinction of the sample may be monitored as a function of time.

a hot electron-hole pair. This process of plasmon decay typically occurs within 10 fs[17]; an *ab initio* description of this process was discussed in Chapter 4. The excited high-energy nonthermal electron loses energy to other electrons through electron-electron scattering and heats the thermal electron bath. Electron thermalization has been shown to be on the order of 500 fs in the noble metals, in contrast to previous assumptions of instantaneous thermalization.[17, 32, 159, 163] The hot electron bath then equilibrates with the phonon bath via electron-phonon scattering on a time scale of a few picoseconds.[17, 119, 164, 165] *Ab initio* descriptions of the processes of electron-electron and electron-phonon thermalization were discussed in Chapter 5. In ultrafast absorption measurements, these processes are monitored using a low-power laser pulse (probe pulse) which is delayed in time with respect to the pump pulse. The probe and pump pulse duration are on a time scale much shorter than that of electron-electron and electron-phonon thermalization. By changing the delay between the pump and probe pulse, the optical response of the sample can be mapped over time, and from this we can draw conclusions about the electron and phonon dynamics which produce the observed optical changes.

Ultrafast pulsed lasers produce much larger excitations than their continuous counterparts. For example, an absorbed 1 ps pulse of 1 μJ deposits an energy density which is six orders of magnitude larger than that of a 1 W continuous laser per picosecond, and it is reasonable to assume that this 1 ps pulse in the metal will excite on the order of one conduction electron per atom.[147] It is this capacity for strong excitation and femtosecond time resolution that has allowed researchers to investigate the microscopic processes of electron and phonon relaxation after plasmon decay.

Figure 6.2 shows a representative map of the optical signal (differential extinction cross section) as a function of pump-probe delay time and probe wavelength. Taking a slice of the map at one probe wavelength reveals the temporal behavior of the electron relaxation (Fig. 6.3(b)). The typical temporal behavior is characterized by an initial fast rise (100's fs) attributed to electron-electron scattering that converts fewer high-energy excited carriers into several more lower-energy carriers, followed by a slower decay (1-10 ps) attributed to electron-phonon scattering. By properly choosing the probe wavelength at which to monitor the temporal response, different mechanisms can be investigated, and studies have taken advantage of this to investigate electron-electron scattering, electron-phonon coupling, electron-spin relaxation, and electronic transport.[32, 123, 125, 131, 166–169]

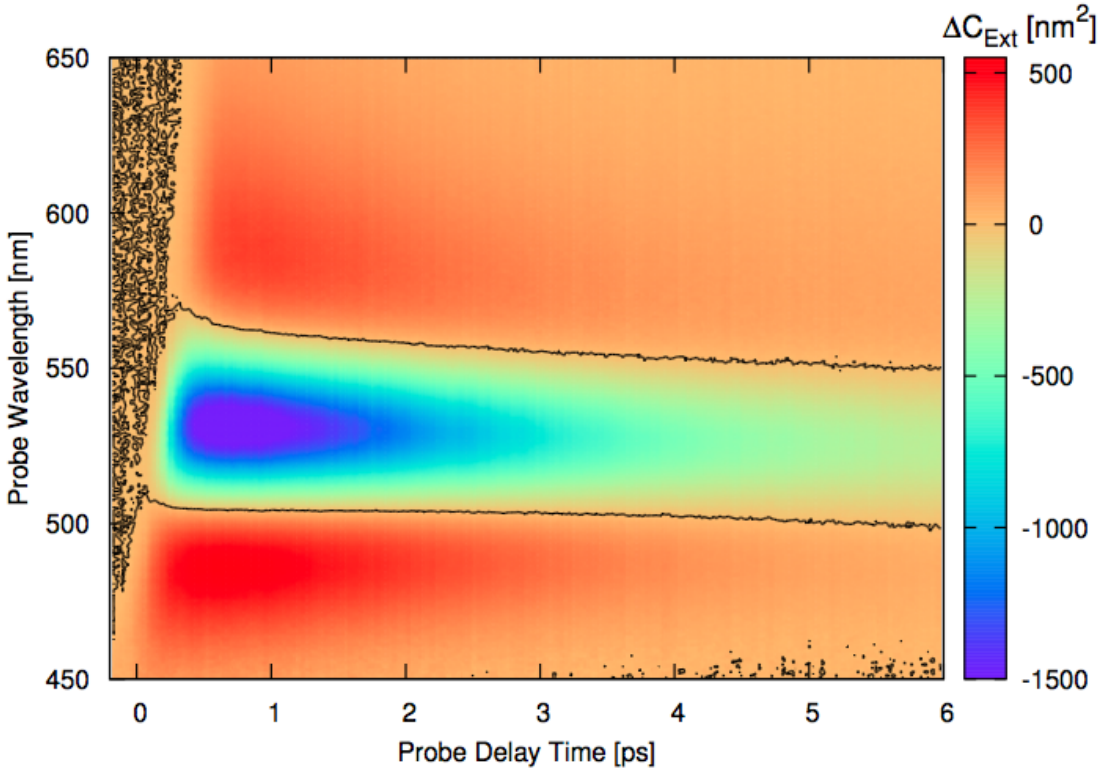

Figure 6.2: Map of the differential extinction cross section as a function of pump-probe delay time and probe wavelength for a pump pulse of 68 μJ/cm^2 energy density at 380 nm. At time 0 ps, the pump pulse excites the sample. As the electrons thermalize, extinction near the absorption peak (533 nm) decreases while extinction in the wings to either side of the absorption peak increases. After ~ 500 fs, the electrons began to thermalize with the lattice and the differential extinction decays. A contour line is drawn in black at zero extinction change.

Taking a slice of the map at one time gives the spectral response, as shown in Figure 6.3(a) for a set of times relative to the delay time with maximum signal, t_{max} = 700 fs. In noble metals excited by a pump pulse, the largest changes in the electron occupation occur near the interband transition threshold, and consequently the changes in the dielectric function and thus the differential optical signal are largest near these energies.[35] The highest sensitivity to the electron temperature is achieved by choosing a probe wavelength near this energy.[147]

Transient absorption measurements of noble metal nanoparticles with a plasmon resonance will display a spectral feature around the plasmon resonance energy, in addition to the usual feature around the interband transition threshold. The differential signal associated with the plasmon resonance is a result of the enhancement of the nonlinear optical response by dielectric confinement around the plasmon res-

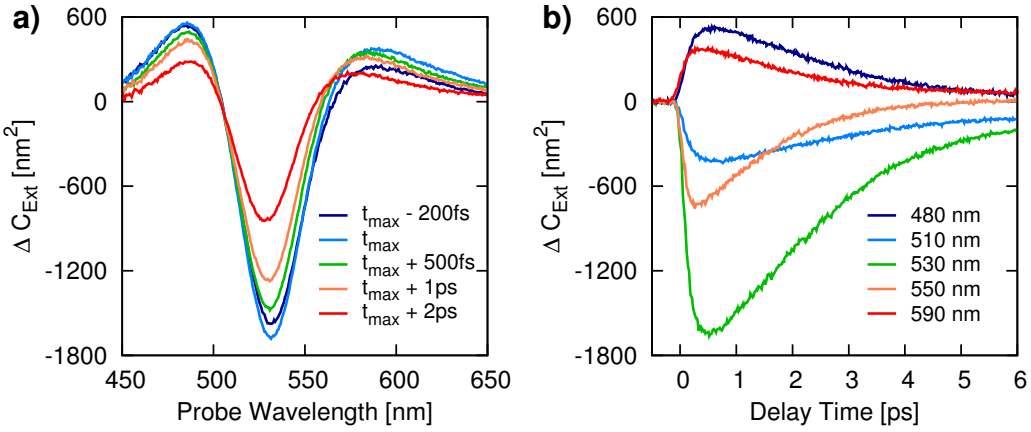

Figure 6.3: Spectral and kinetic traces from differential extinction map in Figure 6.2, for a pump pulse of 68 μJ/cm^2 energy density at 380 nm. Differential extinction (a) as a function of probe wavelength at various times relative to the pump-probe delay time with maximum signal, t_{max} = 700 ps; and (b) as a function of pump-probe delay time at various probe wavelengths.

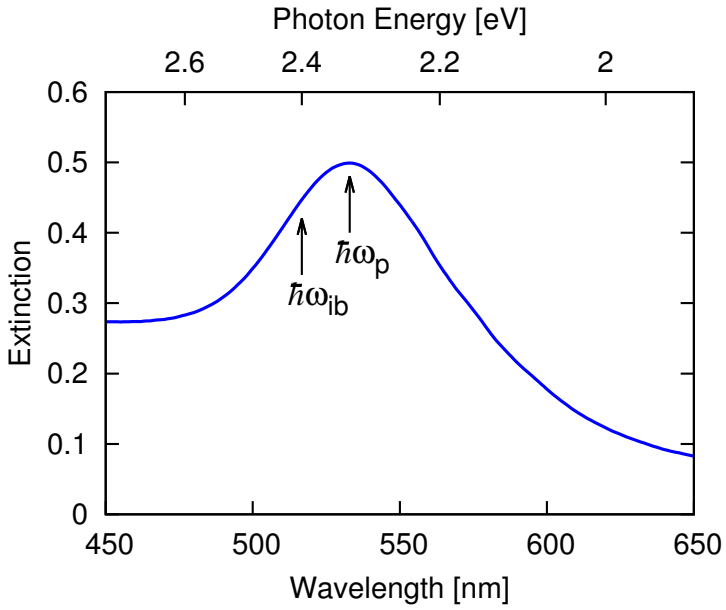

Figure 6.4: Extinction spectra of 60 nm diameter Au colloids in water. The positions of the plasmon resonance, $\hbar\omega_p$, at 2.33 eV and the interband transition threshold, $\hbar\omega_{ib}$, at 2.4 eV are indicated.

onance.[141] For the 60-nm-diameter Au nanoparticles used in the measurements presented in this Chapter, the plasmon resonance (533 nm) is close to the interband transition energy (see Figure 6.4), and the spectral features due to the interband transition and plasmon resonance overlap. The overall spectral shape of the differential optical signal seen in Figure 6.3 (a) can be understood as a thermal broadening of the plasmon absorption resonance, which is the dominant absorption mechanism in the visible wavelength range considered here. The thermal broadening of the resonance results in a decrease in extinction (negative signal) near the plasmon resonance, and an increase in extinction (positive signal) in the wings to either side of the peak.

Recent literature has focused on the contributions of thermalized and nonthermalized electrons to the optical signal in ultrafast pump-probe measurements.[32, 123, 141, 159, 160, 163] However, a detailed *ab initio* understanding of thermal and nonthermal carrier dynamics in conjunction with theory-directed experimental studies has been conspicuously absent. This Chapter addresses the excitation and relaxation dynamics of hot carriers in metals across timescales ranging from 10 fs–10 ps with a parameter-free description of the optical signature.

This Chapter is organized as follows. We start with the theoretical background and computational methods used to calculate the ultrafast pump-probe response which includes the optical response of the metal and the dynamics of the excited carriers, including electron-electron and electron-phonon scattering (Section 6.2). To accurately predict the transient optical response of metal nanostructures without using empirical parameters, we account for the electron-temperature dependence of the electronic heat capacity, electron-phonon coupling factor, and dielectric functions, from fully *ab initio* calculations using the method presented in Chapter 5. In Section 6.3, we describe the experimental details and methodology of the pump-probe measurements performed. We then present the key results of this Chapter: the experimental and theoretical dependence of signal amplitude and temporal behavior on pump power and probe wavelength. We show that the experimental trends are captured by our theoretical results and we analyze these trends in terms of contributions from thermal and nonthermal electron populations to the optical signal.

6.2 *Ab initio* theory

Theoretically describing pump-probe measurements of hot carrier dynamics in plasmonic systems involves two major ingredients. First, the optical response of the

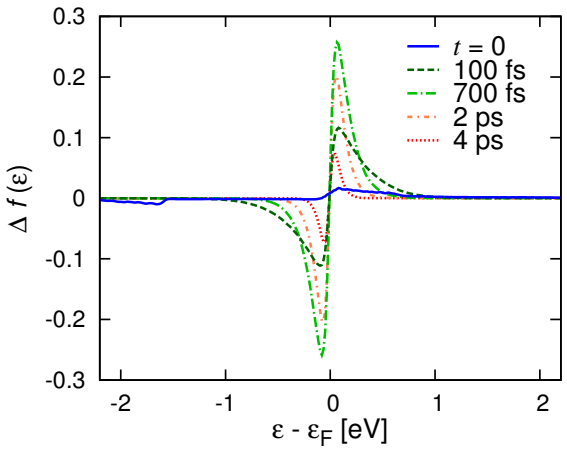

Figure 6.5: Difference of the predicted time-dependent electron distribution from the fermi distribution at 300 K, induced by a pump pulse at 560 nm with intensity of 110 μJ/cm^2. Starting from the carrier distribution excited by plasmon decay at $t = 0$, electron-electron scattering concentrates the distribution near the Fermi level with the peak optical signal at ~700 fs, followed by a return to the ambient-temperature Fermi distribution and a decay of the optical signal due to electron-phonon scattering.

metal (and its environment) determines the excitation of carriers by the pump as well as the subsequent signal measured by the probe pulse. Second, the dynamics of the excited carriers, including electron-electron and electron-phonon scattering, determines the time dependence of the probe signal. In Chapter 5 we presented *ab initio* theory and predictions for both the optical response and the dynamics within a two temperature model, where the electrons are assumed to be in internal equilibrium albeit at a different temperature from the lattice. Here, we additionally treat the response and relaxation of non-thermal electron distributions from first principles, without assuming an effective electron temperature at any point.

For the optical response, we calculate the imaginary part of the dielectric function Im$\epsilon(\omega)$ accounting for direct interband transitions, phonon-assisted intraband transitions and the Drude (resistive) response, and calculate the real part using the Kramers-Kronig relations. Specifically, we start with density-functional theory calculations of electron and phonon states as well as electron-photon and electron-phonon matrix elements using the JDFTx code,[101] convert them to an *ab initio* tight-binding model using Wannier functions,[106] and use Fermi Golden rule and linearized Boltzmann equation for the transitions and Drude contributions respectively. The theory and computational details for calculating $\epsilon(\omega)$ are presented in

detail in Chapters 4 and 5. All these expressions are directly in terms of the electron occupation function $f(\varepsilon)$, and we can straightforwardly incorporate an arbitrary non-thermal electron distribution instead of Fermi functions.

We use the *ab initio* metal dielectric function for calculating the initial carrier distribution as well as the probed response. The initial carrier distribution following the pump pulse is given by

$$f(\varepsilon, t = 0) = f_0(\varepsilon) + U\frac{P(\varepsilon, \hbar\omega)}{g(\varepsilon)}, \tag{6.1}$$

where f_0 is the Fermi distribution at ambient temperature T_0, U is the pump pulse energy absorbed per unit volume, $g(\varepsilon)$ is the electronic density of states (see Ch. 5 Section 5.3), and $P(\varepsilon, \hbar\omega)$ is the energy distribution of carriers excited by a photon of energy $\hbar\omega$ (see Ch. 4). We then evolve the carrier distributions and lattice temperature in time to calculate $f(\varepsilon, t)$ and $T_l(t)$ as described below. From those, we calculate the variation of the metal dielectric function $\epsilon(\omega, t)$, and in turn, the extinction cross section using Mie theory.[25, 26, 170] To minimize systematic errors between theory and experiment, we add the *ab initio* prediction for the change in the dielectric function from ambient temperature (see Ch. 5 Section 5.6), to the experimental dielectric functions from ellipsometry.[36]

We calculate the time evolution of the carrier distributions using the nonlinear Boltzmann equation

$$\frac{d}{dt}f(\varepsilon, t) = \Gamma_{e-e}[f](\varepsilon) + \Gamma_{e-ph}[f, T_l](\varepsilon), \tag{6.2}$$

where Γ_{e-e} and Γ_{e-ph}, respectively, are the contributions due to electron-electron and electron-phonon interactions to the collision integral. For simplicity, we assume that the phonons remain thermal at an effective temperature $T_l(t)$ and calculate the time evolution of the lattice temperature using energy balance,

$$\left.\frac{dE}{dt}\right|_{e-ph} = -C_l(T_l)\frac{dT_l}{dt}, \tag{6.3}$$

where the term on the left corresponds to the rate of energy transfer from the lattice to the electrons due to Γ_{e-ph}, and C_l is the *ab initio* lattice heat capacity (see Ch. 5 Section 5.3).

The *ab initio* collision integrals are extremely expensive to calculate repeatedly for directly solving expression 6.2. We therefore use simpler models for the collision integrals parametrized using *ab initio* calculations. For electron-electron scattering

in plasmonic metals, the calculated electron lifetimes exhibit the inverse quadratic energy dependence $\tau^{-1}(\varepsilon) \approx (D_e/\hbar)(\varepsilon-\varepsilon_F)^2$ characteristic of free electron models within Fermi liquid theory (see Ch. 5 Section 5.6). We therefore use the free-electron collision integral for initial electron states with energies $\varepsilon, \varepsilon_1$ and final electron states with energies $\varepsilon_2, \varepsilon_3$,[32, 123, 171]

$$\begin{aligned}\Gamma_{e-e}[f](\varepsilon) = \frac{2D_e}{\hbar}\int d\varepsilon_1 d\varepsilon_2 d\varepsilon_3 \frac{g(\varepsilon_1)g(\varepsilon_2)g(\varepsilon_3)}{g^3(\varepsilon_F)} \\ \times \delta(\varepsilon+\varepsilon_1-\varepsilon_2-\varepsilon_3)\big[f(\varepsilon_2)f(\varepsilon_3)(1-f(\varepsilon))(1-f(\varepsilon_1)) \\ - f(\varepsilon)f(\varepsilon_1)(1-f(\varepsilon_2))(1-f(\varepsilon_3))\big] \quad (6.4)\end{aligned}$$

with the constant of proportionality D_e extracted from *ab initio* calculations of electron lifetimes (see Appendix Section C).

We calculate the electron-phonon collision integral for the interaction of an arbitrary hot electron distribution, $f(\varepsilon)$, with a thermal phonon distribution $n(\omega, T_l)$, given by the Bose distribution at lattice temperature T_l. We start with the rate of energy transfer between the electrons and lattice per unit volume, which is exactly as in Chapter 5 expressions 5.7 and 5.8, except that we allow $f(\varepsilon)$ to be an arbitrary distribution instead of restricting it to a Fermi distribution:

$$\begin{aligned}\left.\frac{dE}{dt}\right|_{e-ph} &= \frac{2\pi}{\hbar}\int_{BZ}\frac{\Omega d\vec{k}d\vec{k}'}{(2\pi)^6}\sum_{n'n\alpha}\delta(\varepsilon_{\vec{k}'n'}-\varepsilon_{\vec{k}n}-\hbar\omega_{\vec{k}'-\vec{k},\alpha})\hbar\omega_{\vec{k}'-\vec{k},\alpha} \quad (6.5)\\ &\qquad\times\left|g^{\vec{k}'-\vec{k},\alpha}_{\vec{k}n,\vec{k}'n'}\right|^2 S(\varepsilon_{\vec{k}n},\varepsilon_{\vec{k}'n'},\omega_{\vec{k}'-\vec{k},\alpha}) \\ &= \frac{2\pi}{\hbar}\int d\varepsilon\int_{BZ}\frac{\Omega d\vec{k}d\vec{k}'}{(2\pi)^6}\sum_{n'n\alpha}\delta(\varepsilon_{\vec{k}n}-\varepsilon)\delta(\varepsilon_{\vec{k}'n'}-\varepsilon_{\vec{k}n}-\hbar\omega_{\vec{k}'-\vec{k},\alpha})\hbar\omega_{\vec{k}'-\vec{k},\alpha} \\ &\qquad\times\left|g^{\vec{k}'-\vec{k},\alpha}_{\vec{k}n,\vec{k}'n'}\right|^2 S(\varepsilon,\varepsilon+\hbar\omega_{\vec{k}'-\vec{k},\alpha},\omega_{\vec{k}'-\vec{k},\alpha}), \quad (6.6)\end{aligned}$$

where Ω is the unit cell volume, $\hbar\omega_{\vec{k}'-\vec{k},\alpha}$ is the energy of a phonon with wave-vector $\vec{q} = \vec{k}' - \vec{k}$ and polarization index α, and $g^{\vec{k}'-\vec{k},\alpha}_{\vec{k}'n',\vec{k}n}$ is the *ab initio* electron-phonon matrix element coupling this phonon to electronic states indexed by $\vec{k}n$ and $\vec{k}'n'$, described in Chapter 4, Section 4.6. The occupation term $S(\varepsilon,\varepsilon',\omega)$ is defined as

$$S(\varepsilon,\varepsilon',\omega) \equiv f(\varepsilon)n(\omega)(1-f(\varepsilon')) - (1-f(\varepsilon))(1+n(\omega))f(\varepsilon'). \quad (6.7)$$

Using energy conservation and assuming that phonon energies are negligible on the electronic energy scale (an excellent approximation for optical frequency excita-

tions in metals), we simplify the occupation term

$$S(\varepsilon,\varepsilon',\omega) = f(\varepsilon)n(\omega)(1-f(\varepsilon+\hbar\omega)) - (1-f(\varepsilon))(1+n(\omega))f(\varepsilon+\hbar\omega) \tag{6.8}$$

$$\approx f(\varepsilon)n(\omega)\left(1-f(\varepsilon)-\frac{\partial f}{\partial\varepsilon}\hbar\omega\right) - (1-f(\varepsilon))(1+n(\omega))\left(f(\varepsilon)+\frac{\partial f}{\partial\varepsilon}\hbar\omega\right) \tag{6.9}$$

$$= -f(\varepsilon)(1-f(\varepsilon)) - \frac{\partial f}{\partial\varepsilon}\hbar\omega[1+n(\omega)-f(\varepsilon)] \tag{6.10}$$

$$\approx -f(\varepsilon)(1-f(\varepsilon)) - \frac{\partial f}{\partial\varepsilon}\hbar\omega\left[\frac{k_B T_l}{\hbar\omega}\right] \tag{6.11}$$

$$= \left(-\frac{\partial f}{\partial\varepsilon}\right)k_B(T_l - T_{\text{eff}}[f(\varepsilon)]). \tag{6.12}$$

The effective electron temperature T_{eff} is defined as

$$T_{\text{eff}}[f(\varepsilon)] \equiv \frac{f(\varepsilon)(1-f(\varepsilon))}{k_B\left(-\frac{\partial f}{\partial\varepsilon}\right)}, \tag{6.13}$$

which is exactly T_e when $f(\varepsilon)$ is a Fermi distribution.

Substituting equation 6.12 into equation 6.6 gives

$$\left.\frac{dE}{dt}\right|_{e-ph} = \int d\varepsilon\frac{2\pi}{\hbar}\int\frac{\Omega d\vec{k}d\vec{k}'}{(2\pi)^6}\sum_{n'n\alpha}\delta(\varepsilon_{\vec{k}n}-\varepsilon)\delta(\varepsilon_{\vec{k}'n'}-\varepsilon_{\vec{k}n}-\hbar\omega_{\vec{k}'-\vec{k},\alpha}) \times\hbar\omega_{\vec{k}'-\vec{k},\alpha}\left|g^{\vec{k}'-\vec{k},\alpha}_{\vec{k}n,\vec{k}'n'}\right|^2\left(-\frac{\partial f}{\partial\varepsilon}\right)k_B(T_l - T_{eff}[f(\varepsilon)]) \tag{6.14}$$

$$= \frac{2\pi k_B}{\hbar}\int d\varepsilon\left(-\frac{\partial f}{\partial\varepsilon}\right)H(\varepsilon)(T_l - T_{\text{eff}}[f(\varepsilon)]), \tag{6.15}$$

where we define the electron-phonon coupling strength term, $H(\varepsilon)$ as

$$H(\varepsilon) \equiv \int\frac{\Omega d\vec{k}d\vec{k}'}{(2\pi)^6}\sum_{n'n\alpha}\delta(\varepsilon_{\vec{k}n}-\varepsilon)\delta(\varepsilon_{\vec{k}'n'}-\varepsilon_{\vec{k}n}-\hbar\omega_{\vec{k}'-\vec{k},\alpha})\hbar\omega_{\vec{k}'-\vec{k},\alpha}\left|g^{\vec{k}'-\vec{k},\alpha}_{\vec{k}n,\vec{k}'n'}\right|^2 \tag{6.16}$$

or, in terms of the electron-phonon coupling strength $h(\varepsilon)$ defined in Chapter 5,

$$H(\varepsilon) = \frac{g^2(\varepsilon)}{2g(\varepsilon_F)}h(\varepsilon). \tag{6.17}$$

To find the electron-phonon collision integral $\Gamma_{e-ph}(f(\varepsilon,t),T_l) = \left.\frac{df(\varepsilon)}{dt}\right|_{e-ph}$ we note that the contribution to dE/dt (expression 6.3) from electrons with energy ε

corresponds to energy exchange between the lattice and electrons of energy $\varepsilon + \hbar\omega$, where $\hbar\omega$ is negligible on the energy scale of the electrons. Therefore we can equate the energy flow from the electrons to the lattice to an energy flow from electrons with energy ε to electrons with energy $\varepsilon + d\varepsilon$:

$$d\varepsilon \left(-\frac{\partial f}{\partial \varepsilon}\right) H(\varepsilon)(T_l - T_{\text{eff}}[f(\varepsilon)]) = g(\varepsilon + d\varepsilon)\frac{df(\varepsilon + d\varepsilon)}{dt} - g(\varepsilon)\frac{df(\varepsilon)}{dt} \tag{6.18}$$

$$\left(-\frac{\partial f}{\partial \varepsilon}\right) H(\varepsilon)(T_l - T_{\text{eff}}[f(\varepsilon)]) = \frac{\partial}{\partial \varepsilon}[g(\varepsilon)\frac{df(\varepsilon)}{dt}]. \tag{6.19}$$

Integrating by parts over ε yields the desired collision integral

$$\Gamma_{e-ph}(f(\varepsilon,t),T_l) = \left.\frac{df(\varepsilon)}{dt}\right|_{e-ph} = \frac{-1}{g(\varepsilon)}\frac{\partial}{\partial \varepsilon}\left[\left(-\frac{\partial f}{\partial \varepsilon}\right) H(\varepsilon)(T_l - T_{\text{eff}}[f(\varepsilon)])\right]. \tag{6.20}$$

Expressions 6.4, 6.20, and 6.3 give us the time derivatives of the electron occupations and lattice temperature, allowing us to evolve expression 6.2 in time and numerically solve for the electron distribution as a function of time. We use the results for the electron distribution at an array of points in time to calculate the *ab initio* dielectric function, as described in Chapter 5 Section 5.6, at each time. It is then simple to obtain the differential cross section as a function of time, and compare this to experimental results.

Combining the above first-principles calculations of carrier dynamics and optical response produces a complete theoretical description of pump-probe measurements, free of any fitting parameters that are typical in previous analyses.[121, 139, 150, 160] This theory accounts for detailed energy distributions of excited carriers (Figure 6.5) instead of assuming flat distributions,[141, 159, 171] and accounts for electronic-structure effects in the density of states, electron-phonon coupling and dielectric functions beyond the empirical free-electron or parabolic band models previously employed.[31, 32, 121, 123, 132, 139, 141, 144, 150, 171] We use the *ab initio* energy dependent electron-phonon matrix elements, as opposed to the common practice of replacing the matrix element with an empirical constant, which we showed in Chapter 5 Section 5.5 to be a poor approximation.[31, 132, 144, 171] All of these advancements result in a model that is more accurate than previous models, and importantly is free of any fitting parameters, which can easily cause a cancelation of errors and omissions in a model and obscure the correct physical interpretation of experimental data.

6.3 Experimental Methods

We use a ultrafast transient absorption system with a tunable pump and white light probe to measure the extinction of Au colloids in solution as a function of pump-probe delay time and probe wavelength.

The laser system consists of a regeneratively amplified Ti:sapphire oscillator (Coherent Libra), which delivers 1mJ pulse energies centered at 800 nm with a 1 kHz repetition rate. The pulse duration of the amplified pulse is approximately 50 fs. The laser output is split by an optical wedge to produce the pump and probe beams. The pump beam wavelength is tuned using a coherent OperA OPA. The probe beam is focused onto a sapphire plate to generate a white-light continuum probe. The time-resolved differential extinction spectra are collected with a commercial Helios absorption spectrometer (Ultrafast Systems LLC). The temporal behavior is monitored by increasing the path length of the probe pulse and delaying it with respect to the pump pulse with a linear translation stage capable of step sizes as small as 7 fs. Our sample is a solution of 60-nm-diameter Au colloids in water with a concentration of 2.6×10^{10} particles per milliliter (BBI International, EM.GC60, OD1.2) in a quartz cuvette with a 2 mm path length.

6.4 Results

The initial excitation by the pump pulse generates an electron distribution that is far from equilibrium, for which temperature is not well-defined. Our *ab initio* predictions of the carrier distribution at $t = 0$ in Figure 6.5 exhibits high-energy holes in the *d*-bands of gold and lower energy electrons near the Fermi level. These highly non-thermal carriers rapidly decay within 100 fs, resulting in carriers closer to the Fermi level which thermalize in several 100 fs, reaching a peak higher-temperature thermal distribution at $\sim$ 700 fs in the example shown in Figure 6.5. These thermalized carriers then lose energy to the lattice via electron-phonon scattering over several picoseconds.

The conventional two-temperature analysis is only valid in that last phase of signal decay (beyond 1 ps) once the electrons have thermalized; non-thermal character of the electrons plays an important role in the initial rise of the response at earlier times.[32] This initial response consists of two contributions mentioned above: the short-lived highly non-thermal carriers excited initially and the longer-lived thermalizing carriers near the Fermi level.[160]

These two contributions introduce distinct temporal and spectral signatures. Due

to the smaller lifetimes of higher energy carriers (due to higher electron-electron scattering rates), the non-thermal carriers exhibit faster rise and decay times than the thermal carriers closer to the Fermi level.[32, 160] Additionally, the larger energy range of the carrier distribution produces a broader spectral contribution (as a function of probe wavelength) from non-thermal electrons, compared to the thermal electrons which contribute primarily near the resonant d-band to Fermi level transition.[32, 35] We can therefore detect response of non-thermal electrons at low pump powers, where thermal contributions are much smaller due to lower temperature changes, and at probe wavelengths far from the interband resonance, where thermal electrons contribute less. Combining *ab initio* predictions and experimental measurements of 60-nm colloidal gold solutions, we quantitatively identify these signatures of thermal and non-thermal electrons, first as a function of pump power and then as a function of probe wavelength.

Pump power dependence

Increasing the pump power generates a greater number of initial carriers, producing a higher thermalized electron temperature, which increases the overall amplitude of the measured signal, but also increases electron-electron thermalization times and reduces electron-phonon thermalization times. Figure 6.6 shows that our *ab initio* predictions of electron dynamics and optical response quantitatively capture the *absolute* extinction cross section as a function of time for various pump pulse energies. In the remainder of this section, we examine the cross section time dependence normalized by their peak values to more clearly observe the changes in rise and decay time scales.

Decay of the measured signal is because of energy transfer from electrons to the lattice via electron-phonon scattering. At higher pump pulse energies, the electrons thermalize to a higher temperature. For $T_e < 2000$ K, the electron heat capacity increases linearly with temperature, whereas the electron-phonon coupling strength does not appreciably change with electron temperature.[35, 123] Therefore, the electron temperature, and correspondingly the measured probe signal, decays more slowly at higher pump powers as shown in Figure 6.7(a,b). Again, we find quantitative agreement between the measurements and *ab initio* predictions with no empirical parameters.

Rise of the measured signal arises from electron-electron scattering which transfers the energy from few excited non-thermal electrons to several thermalizing electrons

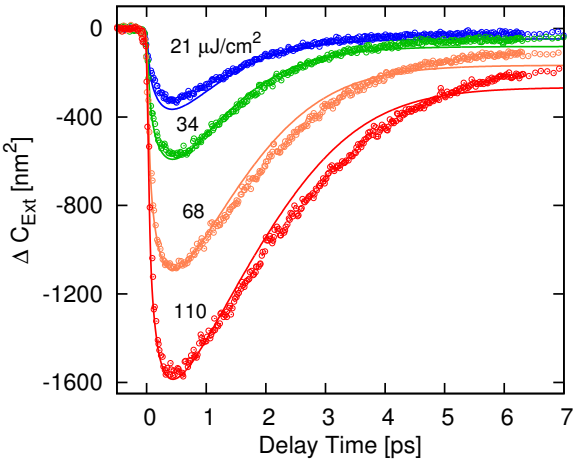

Figure 6.6: Measured (circles) and computed (solid line) differential extinction cross section for a pump pulse at 560 nm with intensity of 21, 34, 68, and 110 μJ/cm^2, and monitored with a 530 nm probe wavelength. As pump power is increased, the signal amplitude increases because of increasing perturbation of the electron distribution and higher peak electron temperatures.

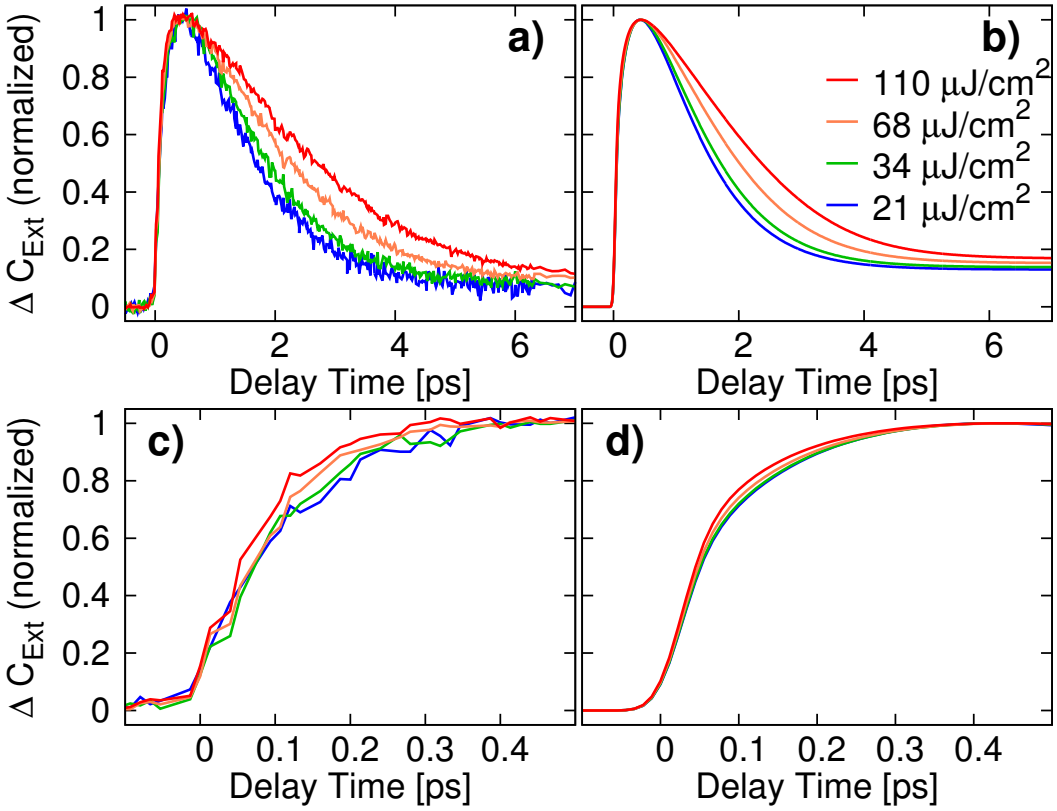

Figure 6.7: The (a) measured and (b) calculated data from Fig. 6.6 normalized to unity. Parts (a) and (b) show that the signal decay slows as pump intensity is increased. Parts (c) and (d) show the data from parts (a), (b) in the first 0.5 ps after excitation, and demonstrate the faster rise time at higher pump intensities.

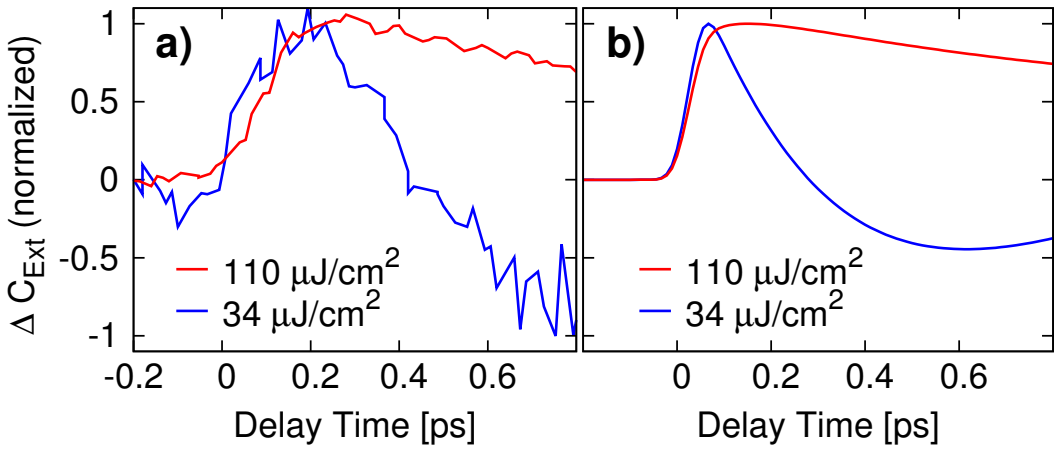

Figure 6.8: The (a) measured and (b) calculated differential cross section for a pump pulse at 380 nm with intensity of 34 and 110 μJ/cm^2 and monitored at 560 nm probe wavelength, normalized to unity. Contributions from the nonthermalized electron distribution dominate at lower pump power, resulting in a fast signal rise and decay, while contributions from the thermalized electron distribution dominate at higher pump powers, resulting in slower signal rise and decay. The small signals at this probe wavelength result in the higher noise to signal ratio seen in part (a).

closer to the Fermi level. Higher power pump pulses generate a greater number of initial non-thermal carriers, requiring fewer electron-electron collisions to raise the temperature of the background of thermal carriers. Additionally, the electron-electron collision rate increases with temperature because of increased phase space for scattering.[123] Both these effects lead to a faster rise time at higher pump powers, as seen in the measurements shown in Figure 6.7(c), as well as in the *ab initio* predictions shown in Figure 6.7(d), which are in quantitative agreement.

Finally, we examine the variation of the ratio of thermal and non-thermal electron contributions with pump power. Figure 6.8 shows the sub-picosecond variation of measured response for two different pump powers, but now with a pump wavelength of 380 nm with a higher energy photon that excites non-thermal carriers further from the Fermi level. Additionally, the probe wavelength of 560 nm is far from the interband resonance at $\sim$ 520 nm, so that the thermal electrons contribute less to the measured response. For the lower pump power, the thermal contribution is small at this probe wavelength making the non-thermal contribution relatively more important, resulting in a faster rise and decay time. At higher power, the thermal contribution response broadens, changing the ratio between the nonthermal and thermal contributions at this probe wavelength. The thermal contribution dominates at higher power, resulting in a slower signal rise and decay time. Once again, the

measurements and *ab initio* calculations, which include all these effects implicitly, are in quantitative agreement.

Probe wavelength dependence

The contributions of the nonthermal and thermal electron populations to the optical signal vary as a function of probe energy, as discussed above. Thus, the temporal behavior of the nonthermalized and thermalized electron signal contributions can be separated by properly selecting the probe energy with which to monitor the electron-relaxation process. At probe energies far away from the interband transition energy the contribution from thermalized electrons is reduced and the short time response of the metal (<1 ps) is dominated by the nonthermal character of the electron distribution. These probe energies allow for direct and sensitive observation of the internal thermalization of the electron gas. For probe energies close to the interband transition energy, the signal contributions from the thermalized electrons dominate, and the signal rise and decay is much slower than that at probe energies where the nonthermal contributions dominate. At these probe energies close to the interband transition energy, only the distribution change close to the Fermi level is detected because of the high transition probability to those states, and although the signal at these probe energies *a priori* detects the electron thermalization over the full excited region, the signal is dominated by electron-electron collisions close to the Fermi level. Because of Pauli exclusion effects, these are the slowest scattering processes involved in the internal thermalization and result in the slow rise time of the signal– a longer "local" thermalization time, as predicted by Fermi-liquid theory.[32, 123]

Figure 6.9 shows the measured and theoretical response of the gold nanoparticles excited with a pump pulse at 560 nm with an intensity of 110 μJ/cm^2 and monitored at a probe energy near (530 nm) and far (620 nm) from the interband transition threshold. As expected, where the thermalized distribution contribution dominate at 530 nm, the measured signal reaches its maximum at a later time and exhibits a slower decay than where the nonthermal contributions dominate at 620 nm. This behavior is captured by the theoretical results in part (b) of the Figure.

Figure 6.10 shows data with the same excitation parameters as those in Figure 6.9 for a variety of probe wavelengths. Our theoretical results are in qualitative agreement with the temporal behavior of the signal at the various probe wavelengths. Both the measured and theoretical data show the fastest signal rise and decay when

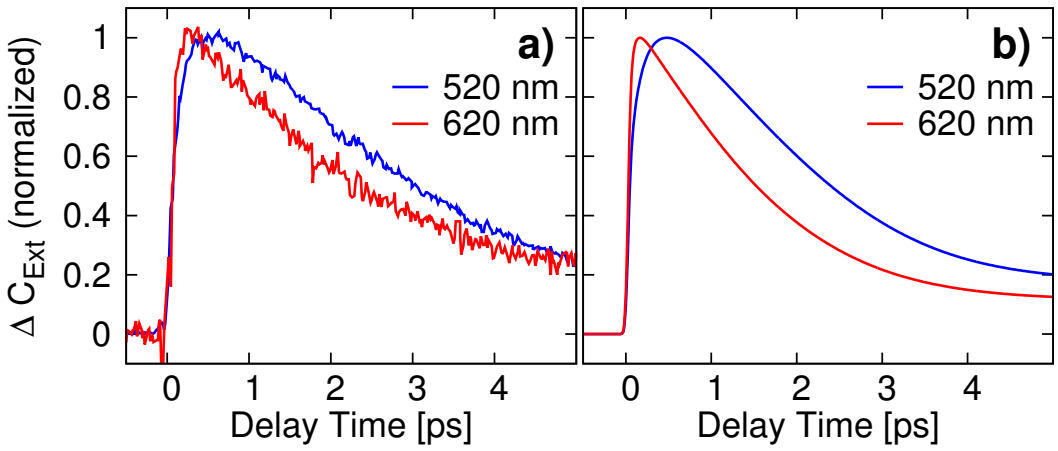

Figure 6.9: The (a) measured and (b) calculated differential cross section for a pump pulse at 560 nm with an intensity of 110 μJ/cm^2 normalized to unity, for probe wavelengths of 520 and 620 nm. Where contributions from the thermalized distribution dominates at 530 nm, the measured signal reaches its maximum at a later time and exhibits a slower decay than where the nonthermal distribution contributions dominate at 620 nm.

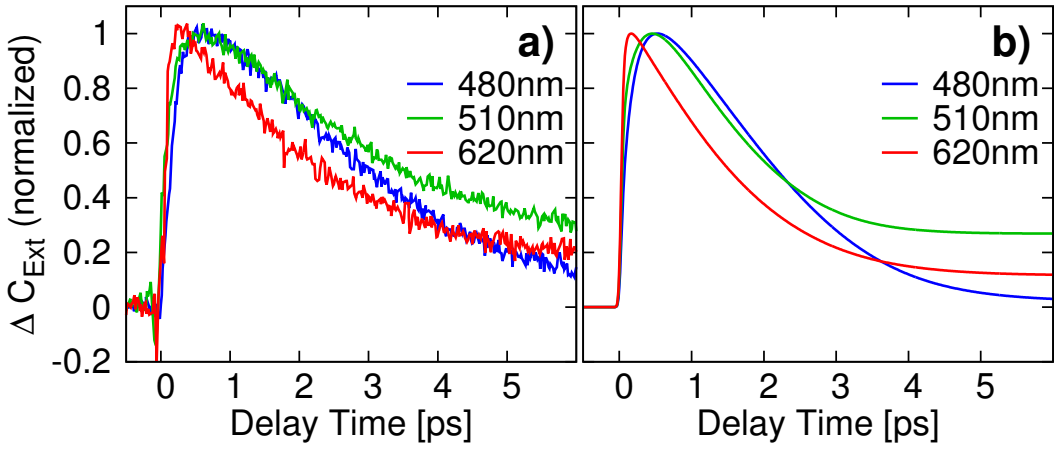

Figure 6.10: The (a) measured and (b) calculated differential cross section for a pump pulse at 560 nm with an intensity of 110 μJ/cm^2 normalized to unity, for probe wavelengths of 480, 510, and 620 nm.

the probe is furthest from the interband transition energy (620 nm probe). The crossing points of the data traces and the relative positions, especially at long delay times, are in good agreement for the experimental and theoretical results.

6.5 Conclusions

In this Chapter, we presented experimental and theoretical results that explored the effects of pump power and probe wavelength on the spectral and temporal behavior of the transient extinction of 60 nm Au colloids in solution. We com-

bined first-principles calculations of carrier dynamics and optical response from Chapters 4 and 5 to achieve an improved nonlinearized Boltzmann method that fully accounts for the nonthermal character of the exited electron distribution and electronic-structure effects. The theoretical calculations use our *ab initio* results for the excited electron distribution produced via plasmon decay, electronic density of states, and electron-temperature dependent electron-phonon coupling and dielectric function to replace approximations of these parameters used by previous investigations. We presented experimental and theoretical results which investigated the contributions from thermal and non-thermal electrons to the optical signal, as function of both pump power and probe wavelength. Our *ab initio* predictions captured the signature temporal and spectral features seen experimentally for these two contributions. This complete theoretical description of hot carrier dynamics will be useful as researchers investigate new roles for hot carriers in technologies ranging from energy conversion and photocatalysis to photodetection.

Chapter 7

SUMMARY AND OUTLOOK

The work presented in this thesis focused on the classical relationship between charge density and the plasmon resonance and on a quantum description of plasmon decay and hot carrier relaxation.

The first investigation discussed in this thesis laid out a thermodynamic framework which predicts optically induced electrochemical potentials on plasmonic resonators. We showed experimental and optical measurements which showed evidence of the predicted plasmoelectric effect. Future work to find further evidence of a plasmoelectric response could involve repeating the optical experiments detailed in Chapter 2 with Au colloids suspended in a gel electrolyte that is highly polarizable. In our experiments, we used Au colloids suspended in water, as received from the supplier. We did not add electrolytes to the solution because this would cause the particles to aggregate and precipitate out of solution. However, a gel electrolyte matrix could be used to immobilize the particles as suspended single particles and the high polarizability of the matrix would allow increased charging of the particles and a larger plasmoelectric response. Other optical plasmoelectric experiments could include monitoring the change in extinction of Au colloids under white light illumination (as a control) and under white light illumination plus a single monochromatic optical pump to either side of the neutral plasmon resonance. Under these conditions, measuring a blue-shift of the extinction profile with a pump to the blue of the resonance, and a red-shift of the extinction profile with a pump to the red of the resonance would provide further evidence of a plasmoelectric response.

Future applications could use a plasmoelectric system to convert optical power to electrical power by engineering a system with two components: one that will take on a decreased charge density and one that will take on an increased charge density, and connecting the components to produce a voltage difference. For example, this could be done by using two components with the same resonance and illuminating one with light to the blue of the resonance and the other with light to the red of the resonance, or by using one color of light to illuminate two components– one with a resonance to the blue of the illumination wavelength and another with a resonance

to the red of the illumination wavelength. This would allow for a new avenue for harnessing the power of the sun as a renewable energy source using an all-metal system.

The second investigation presented in this thesis explored the non-ideal effects which play a role in the electrical tuning of the optical properties of Au nanoparticles. We developed simulations that used a modified dielectric function to account for voltage-dependent changes in the system, and used these simulations to quantify the contributions of various effects to the changes in the optical properties. Tunable plasmonic systems have a multitude of applications, including applications in energy conservation. For example tunable plasmonic systems consisting of plasmonic resonators dispersed in a transparent conductive medium are currently being investigated as a means of controlling the amount of near-infrared and visible light that is transmitted through windows.[172, 173] These technologies could decrease the energy requirements for air-conditioning. The simulations methods discussed in Chapter 3 could be used to analyze and optimize tunable plasmonic systems for such applications.

In the last three projects discussed in this thesis we preformed *ab initio* calculations to achieve a complete theoretical description of plasmon decay and the relaxation of plasmonicaly excited hot carriers. We showed that the electronic structure and the role of phonons, which have been previously ignored, are critical for an accurate description of plasmon decay. We also explored the effect of surfaces and geometric confinement in nanoscale systems. Our fitting-parameter-free theory, which we have shown to be in good agreement with experimental results, is a significant advancement over previously used models that relied on empirical parameters and fitting-parameters to achieve agreement with experimental results.[121, 139, 150, 160] Moreover, these previously used empirical and fitting parameters may obscure the correct physical interpretation of experimental data.

Currently, researchers are investigating the use of plasmonicaly excited hot carriers as catalysts for photochemistry such as the dissociation of hydrogen gas and reduction of carbon dioxide, as well as collection of hot carriers across a metal-semiconductor boundary to avoid the loss of absorption at energies below the band-gap of the semiconductor.[33, 156, 174, 175] These applications take advantage of the excellent light absorption and confinement provided by plasmons, but very low quantum efficiencies have been achieved so far and it is experimentally difficult to separate effects of hot carriers from overall local heating, making it hard to use ex-

perimental results to optimize efficiency. For improved efficiencies in applications, we must collect or use hot carriers before they thermalize. Our complete theoretical description of plasmon decay and hot carrier relaxation from first-principles gives us a better understanding that can be used to aid advancement of hot carrier applications in photocatalysis, energy conversion, and photodetection.

The next steps in this work would be to combine our theoretical description of hot carrier generation and relaxation with a theoretical description of hot carrier transport to provide a complete picture of temporal and spatial dynamics that could be used to improve the efficiency of hot carrier applications. In this way, one could investigate the interplay of material electronic structure and nanoscale geometry and predict space and time resolved carrier distributions and response. This would allow the computational design of nanostructures and interfaces for the efficient use and collection of hot carriers with localized carrier generation.

BIBLIOGRAPHY

1. Schuller, J. A. *et al.* Plasmonics for extreme light concentration and manipulation. *Nature Materials* **9,** 193–204 (2010).
2. Barnes, W. L., Dereux, A. & Ebbesen, T. W. Surface plasmon subwavelength optics. *Nature* **424,** 824–830 (2003).
3. Pendry, J. Playing Tricks with Light. *Science* **285,** 1687–1688 (1999).
4. Khurgin, J. B. How to deal with the loss in plasmonics and metamaterials. *Nature Nanotechnology* **10,** 2–6 (2015).
5. Polman, A. Plasmonics Applied. *Science* **322,** 868–869 (2008).
6. Maier, S. A. Plasmonics: a route to nanoscale optical devices. *Advanced Mater* **13,** 1501–1505 (2001).
7. Novotny, L. & van Hulst, N. Antennas for light. *Nature Photonics* **5,** 83–90 (2011).
8. Zia, R. & Brongersma, M. L. Surface plasmon polariton analogue to Young's double-slit experiment. *Nature Nanotechnology* **2,** 426–429 (2007).
9. Dionne, J. A., Sweatlock, L. A., Sheldon, M. T., Alivisatos, A. P. & Atwater, H. A. Silicon-based plasmonics for on-chip photonics. *Ieee Journal Of Selected Topics In Quantum Electronics* **16,** 295–206 (2010).
10. Macdonald, K. F., Samson, Z. L., Stockman, M. I. & Zheludev, N. I. Ultrafast active plasmonics. *Nature Photonics* **3,** 55–58 (2009).
11. Ma, R. M., Oulton, R. F., Sorger, V. J., Bartal, G. & Zhang, X. Room-temperature sub-diffraction-limited plasmon laser by total internal reflection. *Nature Materials* **10,** 110–113 (2011).
12. Noginov, M. A. *et al.* Demonstration of a spaser-based nanolaser. *Nature* **460,** 1110–1112 (2009).
13. Atwater, H. A. & Polman, A. Plasmonics for improved photovoltaic devices. *Nature Materials* **9,** 205–13 (2010).
14. Pallai, S., Catchpole, T. K. Trupke & Green, M. Surface plasmon enhanced silicon solar cells. *Journal of Applied Physics* **101,** 093105–093108 (2007).
15. Reinhard, B. M., Sheikholeslami, S., Mastroianni, A., Alivisatos, A. P. & Liphardt, J. Use of plasmon coupling to reveal the dynamics of DNA bending and cleavage by single EcoRV restriction enzymes. *Proceedings of the National Academy of Sciences* **104,** 2667–2672 (2007).
16. Marty, R., Baffou, G., Arbouet, A., Girard, C. & Quidant, R. Charge distribution induced inside complex plasmonic nanoparticles. *Optics Express* **18,** 3035–3044 (2010).

17. Hartland, G. Optical Studies of Dynamics in Noble Metal Nanostructures. *Chemical Reviews* **111,** 3858–3887 (2011).

18. Knight, M. W., Sobhani, H., Nordlander, P. & Halas, N. J. Photodetection with Active Optical Antennas. *Science* **332,** 702–704 (2011).

19. Y., L., Jung, C., Park, J., Seo, H. & Somorjai, G. Surface plasmon-driven hot electron flow probed with metal-semiconductor nanodiodes. *Nano Letters* **11,** 4251–4255 (2011).

20. Drude, P. On the electron theory of metals. *Annals of Physics* **306,** 566–613 (1900).

21. Drude, P. Zur elektronentheorie der metalle; II. Teil. galvanomagnetische und thermomagnetische effecte. *Annalen der Physik* **308,** 369–402 (1900).

22. Lorentz, H. A. *Le mouvement des électrons dans les métaux* (1905).

23. Lorentz, H. *The motion of electrons in metallic bodies* in *KNAW, proceedings* **7** (1905), 438–453.

24. Rakic, A. D., Djurisic, A. B., Elazar, J. M. & Majewski, M. L. Optical Properties of Metallic FIlms for Vertical-Cavity Optoelectronic Devices. *Applied Optics* **37,** 5271–5283 (1998).

25. Mie, G. Beiträge zur Optik trüber Medien, speziell kolloidaler Metallösungen. *Annalen der Physik* **330,** 377–445 (1908).

26. Bohren, C. F. & R., H. D. *Absorption and Scattering of Light by Small Particles* (Wiley, New York, 1983).

27. Sannomiya, T., Dermutz, H., Hafner, C., Voros, J. & Dahlin, A. B. Electrochemistry on a Localized Surface Plasmon Resonance Sensor. *Langmuir* **26,** 7619–7626 (2010).

28. Dondapati, S. K. *et al.* Voltage-induced adsorbate damping of single gold nanorod plasmons in aqueous solution. *Nano Letters* **12,** 1247–52 (2012).

29. Novo, C., Funston, A. M., Gooding, A. K. & Mulvaney, P. Electrochemical charging of single gold nanorods. *Journal of the American Chemical Society* **131,** 14664–6 (2009).

30. Maier, S. *Plasmonics: Fundamentals and Applications* (Springer, New York, 2007).

31. Lin, Z., Zhigilei, L. V. & Celli, V. Electron-phonon coupling and electron heat capacity of metals under conditions of strong electron-phonon nonequilibrium. *Physical Review B,* 075133 (77 Feb. 2008).

32. Sun, C.-K., Vallée, F., Acioli, L. H., Ippen, E. P. & Fujimoto, J. G. Femtosecond-tunable measurement of electron thermalization in gold. *Physical Review B* **50,** 15337–15348 (Nov. 1994).

33. Sundararaman, R., Narang, P., Jermyn, A. S., Goddard III, W. A. & Atwater, H. A. Theoretical Predictions for Hot-carrier Generation from Surface Plasmon Decay. *Nature Communication* **5** (5788 2014).

34. Brown, A. M., Sundararaman, R., Narang, P., Goddard III, W. A. & Atwater, H. A. Non-Radiative Plasmon Decay and Hot Carrier Dynamics: Effects of Phonons, Surfaces and Geometry. *ACS Nano* **10,** 957–966 (2015).

35. Brown, A. M., Sundararaman, R., Narang, P., Goddard III, W. A. & Atwater, H. A. Ab initio phonon coupling and optical response of hot electrons in plasmonic metals. *Physical Review B* (2016). Submitted.

36. Palik, E. D. *Handbook of Optical Constants of Solids* (Academic, New York, 1985).

37. Luther, J. M., Jain, P. K., Ewers, T. & Alvisatos, A. Localized surface plasmon resonances arising from free carriers in doped quantum dots. *Nature Materials* **10,** 361–366 (2011).

38. Garcia, G. *et al.* Dynamically modulating the surface plasmon resonance of doped semiconductor nanocrystals. *Nano Letters* **11,** 4415–4420 (2011).

39. Gordon, J. & Ernst, S. Surface-plasmons as a probe of the electrochemcial interface. *Surface Science* **101,** 599–506 (1980).

40. Ashcroft, N. W. & Mermin, N. D. *Solid State Physics* (Harcourt, New York, 1976).

41. Askerov, B. M. & Figarova, S. *Thermodynamics, Gibbs Method and Statistical Physics of Electron Gases* (Springer, New York, 2010).

42. Shockley, W. & J., Q. H. Detailed balance limit of efficiency of p-n junction solar cells. *Journal of Applied Physics* **32,** 510–519 (1961).

43. Kittel, C. *Introduction to Solid State Physics* (Wiley, New York, 2005).

44. Landsberg, P. T. & Tonge, G. Thermodynamic energy conversion efficiencies. *Journal of Applied Physics* **51,** R1–R20 (1980).

45. Cerruti, M. G. *et al.* Gold and Silica-Coated Gold Nanoparticles as Thermographic Labels for DNA Detection. *Analytical Chemistry* **78,** 3282–3288 (2006).

46. Holand, J. P. *Heat Transfer* (McGraw-Hill, New York, 2009).

47. Blatt, F. J., Schroeder, P. A. & Foiles, C. F. *Thermoelectric Power of Metals* (Plenum, New York, 1976).

48. Lang, N. D. & Kohn, W. Theory of metal surfaces: induced surface charge and image potential. *Physical Review B* **7,** 3541 (1973).

49. *FDTD Solutions* (Lumerical Solutions Inc., Vancouver, BC, Canada).

50. Johnson, P. B. & Christy, R. W. Optical constants of the noble metals. *Physical Review B* **6,** 4370–4379 (1972).

51. Nonnenmacher, M., O'Boyle, P. & Wickramasighe, H. K. Kelvin probe force microscopy. *Applied Physics Letters* **58,** 2921 (1991).

52. Noginova, N., Yakima, A. V., Soimo, J., Gu, L. & Noginov, M. A. Light-to-current and current-to-light coupling in plasmonic systems. *Physical Review B* **84,** 035447 (2011).

53. Linic, S., Christopher, P. & Ingram, D. B. Plasmonic-metal nanostructures for efficient conversion of solar to chemical energy. *Nature Materials* **10,** 911–21 (2011).

54. Singh Sekhonand, J. & Verma, S. Refractive Index Sensitivity Analysis of Ag, Au, and Cu Nanoparticles. *Plasmonics* **6,** 311–317 (2011).

55. Kambhampati, A. C. & Patanjali. Surface-enhanced Raman Scattering. *Chemical Society Reviews* **27,** 241–250 (1998).

56. Miyazaki, T. *et al.* Electrical Control of Plasmon Resonance of Gold Nanoparticles Using Electrochemical Oxidation. *Journal of Physical Chemistry C* **113,** 8484–8490 (2009).

57. Persson, B. N. J. Polarizability of Small Spherical Metal Particles: Influence of the Matrix Environment. *Surface Science* **281,** 153–162 (1993).

58. Mayer, K. M. & Hafner, J. H. Localized surface plasmon resonance sensors. *Chemical Reviews* **111,** 3828–57 (2011).

59. Novo, C., Funston, A. M. & Mulvaney, P. Direct observation of chemical reactions on single gold nanocrystals using surface plasmon spectroscopy. *Nature Nanotechnology* **3,** 598–602 (2008).

60. Mulvaney, P. Surface Plasmon Spectroscopy of Nanosized Metal Particles Mulvaney. *Langmuir* **12,** 788–800 (1996).

61. Kreibig, U. *Optical Properties of Metal Clusters* (Springer, Heidelberg, Germany, 1995).

62. Malinsky, M. D., Kelly, K. L., Schatz, G. C. & Duyne, R. P. V. Nanosphere Lithography: Effect of Substrate on the Localized Surface Plasmon Resonance Spectrum of Silver Nanoparticles. *Journal of Physical Chemistry B* **195,** 2243–2350 (2001).

63. Hilger, A., Cuppers, N., Tenfelde, M. & Kreibig, U. Surface And Interface Effects In The Optical Properties Of Silver Nanoparticles. *European Physics Journal D* **10,** 115–118 (2000).

64. Dahlin, A. B. *et al.* Electrochemical plasmonic sensors. *Analytical and Bioanalytical Chemistry* **402,** 1773–84 (2012).

65. Ung, T., Giersig, M., Dunstan, D. & Mulvaney, P. Spectroelectrocheistory Of Ag Colloids. *Langmuir* **13,** 1773–1782 (1997).

66. Dahlin, A. B., Sannomiya, T., Zahn, R., Sotiriou, G. A. & Voros, J. Electrochemical crystallization of plasmonic nanostructures. *Nano Letters* **11,** 1337–43 (2011).

67. Loo, B. In Situ Identification of Halide Complexes on Gold Electrode by Surface-Enhanced Raman Spectroscopy. *Journal of Physical Chemistry* **85,** 433–437 (1982).

68. Muller, J. *et al.* Electrically controlled light scattering with single metal nanoparticles. *Applied Physics Letters* **81,** 171 (2002).

69. Dahlin, A. B., Zahn, R. & Voros, J. Nanoplasmonic sensing of metal-halide complex formation and the electric double layer capacitor. *Nanoscale* **4,** 2339–51 (2012).

70. Jing, C. *et al.* New insights into electrocatalysis based on plasmon resonance for the real-time monitoring of catalytic events on single gold nanorods. *Analytical Chemistry* **86,** 5513–5518 (2014).

71. Byers, C. P. *et al.* Single-Particle Spectroscopy Reveals Heterogeneity in Electrochemical Tuning of the Localized Surface Plasmon. *Journal of Physical Chemistry B* **118,** 14047–14055 (2014).

72. Brendel, R. & Bormann, D. An infrared dielectric function model for amorphous solids. *Journal of Applied Physics* **71,** 1 (1992).

73. Lioubimov, V., Kolomenskii, A., Mershin, A., Nanopoulos, D. V. & Schuessler, H. A. Effect of Varying Electric Potential on Surface-Plasmon Resonance Sensing. *Applied Optics* **43,** 3426–3432 (2004).

74. Templeton, A. C., Pietron, J. J., Murray, R. W. & Mulvaney, P. Solvent Refractive Index and Core Charge Influences on the Surface Plasmon Absorbance of Alkanethiolate Monolayer-Protected Gold Clusters. *Journal of Physical Chemistry B* **104,** 564–570 (2000).

75. Pinchuk, A., Kreibig, U. & Hilger, A. Optical properties of metallic nanoparticles: influence of interface effects and interband transitions. *Surface Science* **557,** 269–280 (2004).

76. Hendrich, C. *et al.* Chemical interface damping of surface plasmon excitation in metal nanoparticles: a study by persistent spectral hole burning. *Applied Physics B: Lasers and Optics* **76,** 869–875 (2003).

77. Hovel, H., Fritz, S., Hilger, A., Kreibig, U. & Vollmer, M. Width of cluster plasmon resonances: Bulk dielectric functions and chemical interface damping. *Physical Review B* **48,** 18178–18188 (1993).

78. Hubenthal, F. Ultrafast dephasing time of localized surface plasmon polariton resonance and the involved damping mechanisms in colloidal gold nanoparticles. *Progress in Surface Science* **82,** 378–387 (2007).

79. Mulvaney, P., Pérez-Juste, J., Giersig, M., Liz-Marzán, L. M. & Pecharromán, C. Drastic surface plasmon mode shifts in gold nanorods due to electron charging. *Plasmonics* **1,** 61–66 (2006).

80. Lerme, J. *et al.* Size Dependence of the Surface Plasmon Resonance Damping in Metal Nanospheres. *The Journal of Physical Chemistry Letters* **1,** 2922–2928 (2010).

81. Liebsch, A. Prediction of a Ag Multipole Surface. *Physical Review B* **57,** 3803–3806 (1998).

82. Maier, S. A. *Plasmonics: fundamentals and applications* (Springer Science and Business Media, New York, 2007).

83. Moskovits, M. The case for plasmon-derived hot carrier devices. *Nature Nanotechnology* **10,** 6–8 (2015).

84. Clavero, C. Plasmon-induced hot-electron generation at nanoparticle/metal-oxide interfaces for photovoltaic and photocatalytic devices. *Nature Photonics* **8,** 95–103 (2014).

85. Christopher, P., Xin, H. & Linic, S. Visible-light-enhanced catalytic oxidation reactions on plasmonic silver nanostructures. *Nature Chemistry* **3,** 467–472 (2011).

86. Babicheva, V. E. *et al.* Hot Electron Photoemission from Plasmonic Nanostructures: The Role of Surface Photoemission and Transition Absorption. *ACS Photonics* (2015).

87. Zheng, B. Y. *et al.* Distinguishing between plasmon-induced and photoexcited carriers in a device geometry. *Nature Communication* **6.** doi:10.1038/ncomms8797 (2015).

88. Khurgin, J. B. *Ultimate limit of field confinement by surface plasmon polaritons* preprint arXiv:1410.1226. 2014.

89. Stanley, R. Plasmonics in the mid-infrared. *Nature Photonics* **6,** 409–411 (2012).

90. Rakić, A. D., Djurišić, A. B., Elazar, J. M. & Majewski, M. L. Optical properties of metallic films for vertical-cavity optoelectronic devices. *Applied Optics* **37,** 5271–5283 (1998).

91. Ordal, M. A. *et al.* Optical properties of the metals Al, Co, Cu, Au, Fe, Pb, Ni, Pd, Pt, Ag, Ti, and W in the infrared and far infrared. *Applied Optics* **22,** 1099–1119 (1983).

92. Etchegoin, P. G., Le Ru, E. C. & Meyer, M. An analytic model for the optical properties of gold. *The Journal of Chemical Physics* **125,** pages (2006).

93. Bernardi, M., Mustafa, J., Neaton, J. B. & Louie, S. G. Theory and Computation of Hot Carriers Generated by Surface Plasmon Polaritons in Noble Metals. *Nature Communication* **In press** (2015).

94. Noffsinger, J., Kioupakis, E., Van de Walle, C. G., Louie, S. G. & Cohen, M. L. Phonon-Assisted Optical Absorption in Silicon from First Principles. *Physical Review Letters* **108,** 167402 (16 2012).

95. Kioupakis, E., Rinke, P., Schleife, A., Bechstedt, F. & Van de Walle, C. G. Free-carrier absorption in nitrides from first principles. *Physical Review B* **81,** 241201 (24 2010).

96. Hamaguchi, C. *Basic Semiconductor Physics* ISBN: 9783662046562 (Springer Berlin Heidelberg, 2013).

97. Tame, M. S. *et al.* Quantum plasmonics. *Nature Physics* **9,** 329 (June 2013).

98. Archambault, A., Marquier, F., Greffet, J. & Arnold, C. Quantum theory of spontaneous and stimulated emission of surface plasmons. *Physical Review B* **82,** 035411 (2010).

99. Rangel, T. *et al.* Band structure of gold from many-body perturbation theory. *Physical Review B* **86,** 125125 (12 2012).

100. Salpeter, E. E. & Bethe, H. A. A Relativistic Equation for Bound-State Problems. *Physical Review* **84,** 1232–1242 (6 1951).

101. Sundararaman, R., Gunceler, D., Letchworth-Weaver, K. & Arias, T. A. *JDFTx* `http://jdftx.sourceforge.net`. 2012.

102. Perdew, J. P. *et al.* Restoring the Density-Gradient Expansion for Exchange in Solids and Surfaces. *Physical Review Letters* **100,** 136406 (13 2008).

103. Dudarev, S. L., Botton, G. A., Savrasov, S. Y., Humphreys, C. J. & Sutton, A. P. Electron-energy-loss spectra and the structural stability of nickel oxide: An LSDA+U study. *Physical Review B* **57,** 1505–1509 (3 1998).

104. Marini, A., Onida, G. & Del Sole, R. Plane-wave DFT-LDA calculation of the electronic structure and absorption spectrum of copper. *Physical Review B* **64,** 195125 (19 2001).

105. Marzari, N. & Vanderbilt, D. Maximally localized generalized Wannier functions for composite energy bands. *Physical Review B* **56,** 12847–12865 (20 1997).

106. Souza, I., Marzari, N. & Vanderbilt, D. Maximally localized Wannier functions for entangled energy bands. *Physical Review B* **65,** 035109 (3 2001).

107. Giustino, F., Cohen, M. L. & Louie, S. G. Electron-phonon interaction using Wannier functions. *Physical Review B* **76,** 165108 (16 2007).

108. Sundararaman, R., Narang, P., Atwater, H. & III, W. G. *Geometry-induced intraband transitions in surface-plasmon polaritons and nano-structured geometries* 2016. In preparation.

109. Govorov, A. O., Zhang, H. & Gun'ko, Y. K. Theory of Photoinjection of Hot Plasmonic Carriers from Metal Nanostructures into Semiconductors and Surface Molecules. *The Journal of Physical Chemistry C* **117,** 16616–16631 (2013).

110. Manjavacas, A., Liu, J. G., Kulkarni, V. & Nordlander, P. Plasmon-Induced Hot Carriers in Metallic Nanoparticles. *ACS Nano* **8,** 7630–7638 (2014).

111. Zhang, H. & Govorov, A. O. Optical Generation of Hot Plasmonic Carriers in Metal Nanocrystals: The Effects of Shape and Field Enhancement. *The Journal of Physical Chemistry C* **118,** 7606–7614 (2014).

112. Landau, L. On the vibration of the electronic plasma. *Journal of Physics USSR* **10** (1946).

113. Bohm, D. & Pines, D. A Collective Description of Electron Interactions: III. Coulomb Interactions in a Degenerate Electron Gas. *Physical Review* **92,** 609–625 (3 Nov. 1953).

114. Elson, J. M. & Ritchie, R. H. Photon Interactions at a Rough Metal Surface. *Physical Review B* **4,** 4129–4138 (12 1971).

115. Nozieres, P. & Pines, D. *Theory Of Quantum Liquids* ISBN: 9780813346533 (Westview Press, 1999).

116. Lide, D. *CRC Handbook of Chemistry and Physics, 84th Edition* ISBN: 9780849304842 (Taylor & Francis, 2003).

117. Grimvall, G. *The electron-phonon interaction in metals* **9** (North-Holland Amsterdam, 1981).

118. Gan, Y., Wang, C. & Chen, Z. Ultrafast laser-excited vibration and elastic modulus of individual gold nanorods. *Optics Letters* **40,** 340–343 (Feb. 2015).

119. Link, S. & A., E.-S. M. Spectral Properties and Relaxation Dynamics of Surface Plasmon Electronic Oscillations in Gold and Silver Nanodots and Nanorods. *The Journal of Physical Chemistry B* **103,** 8410–8426 (1999).

120. Luo, T. & Chen, G. Nanoscale heat transfer - from computation to experiment. *Physical Chemistry Chemical Physics* **15,** 3389–3412 (2013).

121. Norris, P. M. *et al.* Femtosecond pump-probe nondestructive examination of materials. *Review of Scientific Instruments* **74,** 400 (1 Jan. 2003).

122. Anisimov, S. I., Kapeliovich, B. L. & Perelman, T. L. Electron emission from metal surfaces exposed to ultrashort laser pulses. *Zh. Eksp. Teor. Fiz* **66,** 375–377 (1974).

123. Del Fatti, N. *et al.* Nonequilibrium electron dynamics in noble metals. *Physical Review B* **61,** 16956 (2000).

124. Elsayed-Ali, H., Norris, T., Pessot, M. & Mourou, G. Time-resolved observation of electron-phonon relaxation in copper. *Physical Review Letters* **58,** 1212 (1987).

125. Elsayed-Ali, H. E., Juhasz, T., Smith, G. O. & Bron, W. E. Femtosecond thermoreflectivity and thermotransmissivity of polycrystalline and single-crystalline gold films. *Physical Review B* **43,** 4488–4491 (5 1991).

126. Giri, A., Gaskins, J. T., Foley, B. M., Cheaito, R. & Hopkins, P. E. Experimental evidence of excited electron number density and temperature effects on electron-phonon coupling in gold films. *Journal of Applied Physics,* 044305 (117 Jan. 2015).

127. Hartland, G. V. Optical Studies of Dynamics in Noble Metal Nanostructures. *Chemical Reviews* **111,** 3858–3887 (2011).

128. Kaganov, M. I., Lifshitz, I. M. & Tanatarov, L. V. Relaxation between electrons and the crystalline lattice. *Soviet Physics Jetp-Ussr* **4,** 173–178 (1957).

129. Mueller, B. Y. & Rethfeld, B. Nonequilibrium electron–phonon coupling after ultrashort laser excitation of gold. *Applied Surface Science* **302,** 24–28 (May 2014).

130. Groeneveld, R. H., Sprik, R. & Lagendijk, A. Ultrafast relaxation of electrons probed by surface plasmons at a thin silver film. *Physical Review Letters* **64,** 784 (1990).

131. Groeneveld, R. H., Sprik, R. & Lagendijk, A. Femtosecond spectroscopy of electron-electron and electron-phonon energy relaxation in Ag and Au. *Physical Review B* **51,** 11433 (1995).

132. Rethfeld, B., Kaiser, A., Vicanek, M. & Simon, G. Ultrafast dynamics of nonequilibrium electrons in metals under femtosecond laser irradiation. *Physical Review B* **65,** 214303 (May 2002).

133. Ma, Y. A two-parameter nondiffusive heat conduction model for data analysis in pump-probe experiments. *Journal of Applied Physics* **116,** pages (2014).

134. Landau, L. D. & Lifschitz, E. M. *Electrodynamics of Continuous Media, Course of Theoretical Physics* (Pergamon Press, Oxford, 1960).

135. Ziman, J. M. *Electrons and Phonons* (Clarendon Press, Oxford, 1962).

136. Ashcroft, N. W. & Mermin, N. D. *Solid State Physics* (Holt, Rinehart and Winston: New York, 1976).

137. Pines, D. & Nozieres, P. *Normal Fermi Liquids, The Theory of Quantum Liquids* (Addison-Wesley, New York, 1966).

138. Link, S., Burda, C., Mohamed, M. B., Nikoobakht, B. & El-Sayed, M. A. Laser Photothermal Melting and Fragmentation of Gold Nanorods: Energy and Laser Pulse-Width Dependence. *The Journal of Physical Chemistry A* **103,** 1165–1170 (Mar. 1999).

139. Giri, A., Gaskins, J. T., Foley, B. M., Cheaito, R. & Hopkins, P. E. Experimental evidence of excited electron number density and temperature effects on electron-phonon coupling in gold films. *Journal of Applied Physics* **117,** pages (2015).

140. Perdew, J. P., Burke, K. & Ernzerhof, M. *Physical Review Letters* **77,** 3865 (1996).

141. Voisin, C., Del Fatti, N., Christofilos, D. & Vallée, F. Ultrafast electron dynamics and optical nonlinearities in metal nanoparticles. *The Journal of Physical Chemistry B* **105,** 2264–2280 (2001).

142. Hodak, J. H., Henglein, A. & Hartland, G. V. Photophysics of nanometer sized metal particles: electron-phonon coupling and coherent excitation of breathing vibrational modes. *The Journal of Physical Chemistry B* **104,** 9954–9965 (2000).

143. Allen, P. B. Theory of thermal relaxation of electrons in metals. *Physical Review Letters* **59,** 1460 (1987).

144. Wang, X. Y., Riffe, D. M., Lee, Y.-S. & Downer, M. C. Time-resolved electron-temperature measurement in a highly excited gold target using femtosecond thermionic emission. *Physical Review B* **50,** 8016 (1994).

145. McMillan, W. Transition temperature of strong-coupled superconductors. *Physical Review* **167,** 331 (1968).

146. Hostetler, J. L., Smith, A. N., Czajkowsky, D. M. & Norris, P. M. Measurement of the electron-phonon coupling factor dependence on film thickness and grain size in Au, Cr, and Al. *Applied Optics* **38,** 3614–3620 (1999).

147. Hohlfeld, J. *et al.* Electron and lattice dynamics following optical excitation of metals. *Chemical Physics* **251,** 237–258 (2000).

148. Guo, C., Rodriguez, G., Lobad, A. & Taylor, A. Structural phase transition of aluminum induced by electronic excitation. *Physical Review Letters* **84,** 4493 (2000).

149. Ladstädter, F., Hohenester, U., Puschnig, P. & Ambrosch-Draxl, C. First-principles calculation of hot-electron scattering in metals. *Physical Review B* **70,** 235125 (23 2004).

150. Rosei, R., Antonangeli, F. & Grassano, U. d bands position and width in gold from very low temperature thermomodulation measurements. *Surface Science* **37,** 689–699. ISSN: 0039-6028 (1973).

151. Brongersma, M. L., Halas, N. J. & Nordlander, P. Plasmon-induced hot carrier science and technology. *Nature Nanotechnology* **10,** 25–34 (2015).

152. Linic, S., Aslam, U., Boerigter, C. & Morabito, M. Photochemical transformations on plasmonic metal nanoparticles. *Nat Mater* **14,** 567–576 (June 2015).

153. Leenheer, A. J., Narang, P., Lewis, N. S. & Atwater, H. A. Solar energy conversion via hot electron internal photoemission in metallic nanostructures: efficiency estimates. *J. Appl. Phys.* **115,** 134301 (2014).

154. White, T. P. & Catchpole, K. R. Plasmon-enhanced internal photoemission for photovoltaics: Theoretical efficiency limits. *Applied Physics Letters* **101,** pages (2012).

155. Linic, S., Christopher, P., Xin, H. & Marimuthu, A. Catalytic and photocatalytic transformations on metal nanoparticles with targeted geometric and plasmonic properties. *Acc. Chem. Res.* **46,** 1890–1899 (2013).

156. Mukherjee, S., Libisch, F. & Large, N. Hot electrons do the impossible: Plasmon-induced dissociation of H2 on Au. *Nano Lett.* **13,** 240–247 (2012).

157. Harutyunyan, H. *et al.* Anomalous ultrafast dynamics of hot plasmonic electrons in nanostructures with hot spots. *Nature Nanotechnology* **10,** 770–774 (Sept. 2015).

158. Del Fatti, N., Flytzanis, C. & Vallee, F. Ultrafast induced electron–surface scattering in a confined metallic system. *Applied Physics B: Lasers and Optics* **68,** 433–437 (1999).

159. Della Valle, G., Conforti, M., Longhi, S., Cerullo, G. & Brida, D. Real-time optical mapping of the dynamics of nonthermal electrons in thin gold films. *Physical Review B* **86,** 155139 (2012).

160. Shen, X., Timalsina, Y. P., Lu, T.-M. & Yamaguchi, M. Experimental study of electron-phonon coupling and electron internal thermalization in epitaxially grown ultrathin copper films. *Physical Review B* **91,** 045129 (2015).

161. Del Fatti, N., Vallée, F., Flytzanis, C., Hamanaka, Y. & Nakamura, A. Electron dynamics and surface plasmon resonance nonlinearities in metal nanoparticles. *Chemical Physics* **251,** 215–226 (2000).

162. Averitt, R., Westcott, S. & Halas, N. Ultrafast electron dynamics in gold nanoshells. *Physical Review B* **58,** R10203 (1998).

163. Giri, A. & Hopkins, P. E. Transient thermal and nonthermal electron and phonon relaxation after short-pulsed laser heating of metals. *Journal of Applied Physics* **118,** 215101 (2015).

164. Link, S. & El-Sayed, M. A. Optical properties and ultrafast dynamics of metallic nanocrystals. *Annual Review of Physical Chemistry* **54,** 331–366 (2003).

165. Huang, W., Qian, W., El-Sayed, M. A., Ding, Y. & Wang, Z. L. Effect of the lattice crystallinity on the electron-phonon relaxation rates in gold nanoparticles. *The Journal of Physical Chemistry C* **111,** 10751–10757 (2007).

166. Knoesel, E., Hotzel, A. & Wolf, M. Ultrafast dynamics of hot electrons and holes in copper: Excitation, energy relaxation, and transport effects. *Physical Review B* **57,** 12812 (1998).

167. Aeschlimann, M. *et al.* Ultrafast spin-dependent electron dynamics in fcc Co. *Physical Review Letters* **79,** 5158 (1997).

168. Hohlfeld, J., Matthias, E., Knorren, R. & Bennemann, K. Nonequilibrium magnetization dynamics of nickel. *Physical Review Letters* **78,** 4861 (1997).

169. Brorson, S., Fujimoto, J. & Ippen, E. Femtosecond electronic heat-transport dynamics in thin gold films. *Physical Review Letters* **59,** 1962 (1987).

170. Matzler, C. *MATLAB Functions for Mie Scattering and Absorption* tech. rep. 2002-08 (Institut fur Angewandte Physik, University of Bern, Sidlerstrasse 5, 3012 Bern, Schweiz, 2002).

171. Mueller, B. & Rethfeld, B. Relaxation dynamics in laser-excited metals under nonequilibrium conditions. *Physical Review B* **87,** 035139 (2013).

172. Runnerstrom, E. L., Llordés, A., Lounis, S. D. & Milliron, D. J. Nanostructured electrochromic smart windows: traditional materials and NIR-selective plasmonic nanocrystals. *Chemical Communications* **50,** 10555–10572 (2014).

173. Llordés, A., Garcia, G., Gazquez, J. & Milliron, D. J. Tunable near-infrared and visible-light transmittance in nanocrystal-in-glass composites. *Nature* **500,** 323–326 (2013).

174. Hou, W. *et al.* Photocatalytic conversion of CO2 to hydrocarbon fuels via plasmon-enhanced absorption and metallic interband transitions. *ACS Catalysis* **1,** 929–936 (2011).

175. Zhang, X., Chen, Y. L., Liu, R.-S. & Tsai, D. P. Plasmonic photocatalysis. *Reports on Progress in Physics* **76,** 046401 (2013).

Appendix A

DERIVATIONS OF EXPRESSIONS FOR DIRECT AND PHONON-ASSISTED PLASMON DECAY

A.1 Direct Transitions

Here we sketch the derivation of equation 4.2, presented in Reference 33. For further details and discussion please see Reference 33.

The initial system we consider is a surface plasmon with wave vector $\vec{k}$ on the surface of a semi-infinite slab with the surface normal in the z direction, and a Fermi sea of qausiparticles within the slab. Fermi's golden rule for the decay of a plasmon to a single electron-hole pair is

$$\Gamma_{\text{direct}} = \frac{2\pi}{\hbar} \sum_{\vec{q}n\vec{q}'n'} \delta(\varepsilon_{\vec{q}'n'} - \varepsilon_{\vec{q}n} - \hbar\omega)|M^k_{qn,q'n'}|^2, \tag{A.1}$$

where $\vec{q}$, $\vec{q}'$ are the electron and hole wave vectors, n, n' are the electron and hole band indices, and $M^k_{qn,q'n'}$ is the electron-dipole transition matrix element.

Given an approximation of the quasiparticle orbitals $\psi^\sigma_{\vec{q}n}(\vec{r})$ with energies $\epsilon_{\vec{q}n}$, the many-body real-space annihilation operator (also called the field operator) can be written as $\Psi_\sigma(\vec{r},t) = \sum_{\vec{q}n} \psi^\sigma_{\vec{q}n}(\vec{r}) e^{-i\epsilon_{\vec{q}n}t/\hbar} c_{\vec{q}n}$, where $c_{\vec{q}n}$ is the fermionic annihilation operator for state $\vec{q}n$. The index σ in the orbitals is used to fully treat relativistic effects such as spin-orbit coupling. The plasmon-quasiparticle interaction is approximated using the lowest order vertex as $\hat{H}_{e-pl} = \frac{e}{m_e} \sum_\sigma \int d\vec{r} \Psi^\dagger_\sigma \hat{A} \cdot \hat{p} \Psi_\sigma$, with $\hat{p}$ the electronic momentum operator. The vector potential operator for plasmons in this system is $\hat{\vec{A}}(\vec{r},t) = \sum_k \vec{u}_{\vec{k}}(\vec{r},t)\hat{\vec{a}}_{\vec{k}} + h.c.$, with $\hat{\vec{a}}_{\vec{k}}$ the annihilation operator and $\vec{u}_{\vec{k}}$ the normalized mode functions of wave vector $\vec{k}$ and angular frequency ω,

$$\vec{u}_{\vec{k}}(\vec{r},t) = \sqrt{\frac{2\pi\hbar}{\omega S L(\omega)}} \left(\hat{k} - \frac{k\hat{\vec{z}}}{\gamma(z)} \right) e^{i\left(\gamma(z)z + \vec{k}\cdot\vec{r} - \omega t\right)}, \tag{A.2}$$

where S is the surface area for plasmon quantization with periodic boundary conditions for discretizing the modes and $L(\omega)$ is a normalization length chosen so that each mode has energy $\hbar\omega$. The wavenumber z satisfies $\gamma^2(z) = \epsilon(z)\omega^2/c^2 - k^2$, with $\epsilon(z) = \epsilon(\omega)$ for $z < 0$ and $\epsilon(z) = 1$ for $z > 0$.

Then, neglecting the photon momentum and the higher-order magnetic field coupling, the electron-dipole transition matrix element is:

$$M^k_{qn,q'n'} = \langle \vec{q}n, \vec{q}'n', \vec{k}|\hat{H}_{e-pl}|0\rangle \tag{A.3a}$$

$$= \frac{\langle 0|\hat{c}^\dagger_{\vec{q}n}\hat{c}_{\vec{q}'n'}a_k}{\sqrt{f_{\vec{q}n}(1-f_{\vec{q}'n'})n_{pl}}}\left[\frac{e}{m_e}\sum_\sigma \int d\vec{r}\Psi^\dagger_\sigma \hat{A}\cdot\hat{p}\Psi_\sigma\right]|0\rangle \tag{A.3b}$$

$$= \sqrt{f_{\vec{q}n}(1-f_{\vec{q}'n'})n_{pl}} \times\left[\frac{\Omega}{L_zS}\sum_\sigma\int_{L_zS} d\vec{r}\psi^{\sigma*}_{\vec{q}'n'}(\vec{r})\frac{e}{m_e}\vec{u}_{\vec{k}}(\vec{r})\cdot\left(\frac{\hbar\nabla+[\vec{r},\hat{V}_{NL}]}{i}\right)\psi^\sigma_{\vec{q}n}(\vec{r})\right] \tag{A.3c}$$

$$\approx \delta_{q'q}\sqrt{f_{\vec{q}n}(1-f_{\vec{q}n'})n_{pl}\overline{\left(\frac{u_k(\vec{r})}{u_k(0)}\right)^2}_{L_zS}} \times\left[\vec{u}_{\vec{k}}(0)\cdot\sum_\sigma\int_\Omega d\vec{r}\psi^{\sigma*}_{qn'}(\vec{r})\frac{e(\hbar\nabla+[\vec{r},\hat{V}_{NL}])}{im_e}\psi^\sigma_{\vec{q}n}(\vec{r})\right] \tag{A.3d}$$

$$= \delta_{q'q}\sqrt{f_{\vec{q}n}(1-f_{\vec{q}n'})n_{pl}\frac{1}{2L_z|\gamma(z<0)|}} \times\left[\vec{u}_{\vec{k}}(0)\cdot\sum_\sigma\int_\Omega d\vec{r}\psi^{\sigma*}_{\vec{q}n'}(\vec{r})\frac{e(\hbar\nabla+[\vec{r},\hat{V}_{NL}])}{im_e}\psi^\sigma_{\vec{q}n}(\vec{r})\right] \tag{A.3e}$$

$$= \delta_{q'q}\sqrt{f_{\vec{q}n}(1-f_{\vec{q}n'})n_{pl}\frac{1}{2L_z|\gamma(z<0)|}}[\vec{u}_{\vec{k}}(0)\cdot e\langle\hat{\vec{p}}\rangle^{\vec{q}}_{n'n}] \tag{A.3f}$$

with momentum matrix elements$\langle\hat{\vec{p}}\rangle^{\vec{q}}_{n'n}$

$$\langle\hat{\vec{p}}\rangle^{\vec{q}}_{n'n} \equiv \sum_\sigma\int_\Omega d\vec{r}\psi^{\sigma*}_{\vec{q}n'}(\vec{r})\frac{\hbar\nabla+[\vec{r},\hat{V}_{NL}]}{im_e}\psi^\sigma_{\vec{q}n}(\vec{r}). \tag{A.3g}$$

n_{pl} is the plasmon occupation number. We quantize the quasiparticles in a box of area S on the surface that extends a depth L_z into the surface. $L_z >> 1/|\gamma(z<0)|$, the decay length of the plasmon mode into the metal. The factor of Ω/L_zS in the third line above accounts for the fact that the orbitals are normalized on the unit cell of volume Ω instead of on the quantization volume L_zS.

Plugging this into equation A.1:

$$\Gamma_{\text{direct}} = \frac{2\pi}{\hbar} \sum_{\vec{q}n\vec{q}'n'} \delta(\varepsilon_{\vec{q}'n'} - \varepsilon_{\vec{q}n} - \hbar\omega)|M^k_{qn,q'n'}|^2 \tag{A.4a}$$

$$= \frac{2\pi}{\hbar} \sum_{\vec{q}n\vec{q}'n'} \delta(\varepsilon_{\vec{q}'n'} - \varepsilon_{\vec{q}n} - \hbar\omega)\delta_{q'q} \frac{f_{\vec{q}n}(1 - f_{\vec{q}n'})n_{pl}}{2L_z|\gamma(z<0)|} \times \left| \sqrt{\frac{2\pi\hbar}{\omega S L(\omega)}} \left(\hat{k} - \frac{k\hat{z}}{\gamma(z<0)} \right) \cdot e\langle \hat{\vec{p}} \rangle^{\vec{q}}_{n'n} \right|^2 \tag{A.4b}$$

$$= \frac{2\pi^2 e^2}{\omega L(\omega)|\gamma(z<0)|} \frac{1}{L_z S} \sum_{\vec{q}nn'} f_{\vec{q}n}(1 - f_{\vec{q}n'})n_{pl}\delta(\varepsilon_{\vec{q}n'} - \varepsilon_{\vec{q}n} - \hbar\omega) \times \left| \left(\hat{k} - \frac{k\hat{z}}{\gamma(z<0)} \right) \cdot \langle \hat{\vec{p}} \rangle^{\vec{q}}_{n'n} \right|^2 \tag{A.4c}$$

$$= \frac{2\pi^2 e^2}{\omega L(\omega)|\gamma(z<0)|\Omega} \times \frac{1}{N_{\vec{q}}} \sum_{\vec{q}nn'} f_{\vec{q}n}(1 - f_{\vec{q}n'})n_{pl}\delta(\varepsilon_{\vec{q}n'} - \varepsilon_{\vec{q}n} - \hbar\omega)|\vec{\lambda}_{\vec{k}} \cdot \langle \hat{\vec{p}} \rangle^{\vec{q}}_{n'n}|^2 \tag{A.4d}$$

$$\vec{\lambda}_{\vec{k}} \equiv \hat{k} - \frac{k\hat{z}}{\gamma(z<0)}, \tag{A.4e}$$

where the quantization number $N_q = L_z S/\Omega$. See Section A.3 for the final expression for direct transitions after accounting for reverse transitions.

A.2 Phonon-Assisted Transitions

Fermi's golden rule for plasmon decay through a phonon-assisted transition is calculated similarly to the direct case in the previous section. For a phonon-assisted transition involving a phonon with energy $\hbar\omega_{\vec{k}'\alpha}$, indexed by wavevector $\vec{k}'$ and mode α,

$$\Gamma_{\text{indirect}} = \frac{2\pi}{\hbar} \sum_{\vec{q}n\vec{q}'n'k'\alpha\pm} \delta(\varepsilon_{\vec{q}'n'} - \varepsilon_{\vec{q}n} - \hbar\omega \mp \hbar\omega_{\vec{k}'\alpha})|\mathcal{T}^{kk'\alpha\pm}_{qn,q'n'}|^2. \tag{A.5}$$

The second-order perturbation theory transition matrix elements are:

$$\mathcal{T}^{k,k'\alpha+}_{qn,q'n'} = \sum_M \left[\frac{\langle \vec{q}n,\vec{q}'n',\vec{k},\vec{k}'\alpha|\hat{H}_{e-pl}|M\rangle\langle M|\hat{H}_{e-ph}|0ph\rangle}{E_M - (\hbar\omega + \hbar\omega_{\vec{k}'\alpha})} + (pl \leftrightarrow ph) \right] \tag{A.6a}$$

$$\mathcal{T}^{k,k'\alpha-}_{qn,q'n'} = \sum_M \left[\frac{\langle \vec{q}n,\vec{q}'n',\vec{k},\vec{k}'\alpha|\hat{H}_{e-pl}|M\rangle\langle M|\hat{H}_{e-ph}|0\rangle}{E_M - (\hbar\omega - \hbar\omega_{\vec{k}'\alpha})} + (pl \leftrightarrow ph) \right] \tag{A.6b}$$

with the electron-plasmon interaction hamiltonian:

$$\hat{H}_{e-pl} = \frac{e}{m_e}\sum_{\sigma}\int d\vec{r}\Psi^{\dagger}_{\sigma}\hat{A}\cdot\hat{p}\Psi_{\sigma} \tag{A.7a}$$

using the interband approximation:

$$\approx \sqrt{\frac{1}{2L_z|\gamma(z<0)|}\frac{2\pi\hbar}{\omega SL(\omega)}}\sum_{\vec{q}n'n}\delta_{\vec{q}\vec{q}'}[\vec{\lambda}_{\vec{k}}\cdot e\langle\hat{\vec{p}}\rangle^{\vec{q}}_{n'n}a_k c^{\dagger}_{\vec{q}n'}c_{\vec{q}n}+h.c.] \tag{A.7b}$$

$$= \sqrt{\frac{\pi\hbar e^2}{\omega L(\omega)|\gamma(z<0)|L_z S}}\sum_{\vec{q}n'n}\delta_{\vec{q}\vec{q}'}[\vec{\lambda}_{\vec{k}}\cdot\langle\hat{\vec{p}}\rangle^{\vec{q}}_{n'n}a_k c^{\dagger}_{\vec{q}n'}c_{\vec{q}n}+h.c.] \tag{A.7c}$$

and the electron-phonon interaction hamiltonian with $\vec{R}s$ labeling the nuclear displacement modes for the degree of freedom s in the unit cell located at $\vec{R}$:

$$\hat{H}_{e-ph} = \sum_{\vec{R}s}\hat{x}_{\vec{R}s}\sum_{\sigma}\int_{N_{\vec{R}}\Omega}d\vec{r}\Psi^{\dagger}_{\sigma}\partial_{\vec{R}s}V_{nuc}(\vec{r})\Psi_{\sigma} \tag{A.8a}$$

writing this in terms of phonon ladder operators:

$$= \frac{1}{\sqrt{N_{\vec{k}'}}}\sum_{\vec{k}'\alpha}\sum_{\vec{q}n}\sum_{\vec{q}'n'}\delta_{\vec{q}+\vec{k}',\vec{q}'}g^{\vec{k}'\alpha}_{n',\vec{q}n}(b^{\dagger}_{\vec{k}'\alpha}+b_{-\vec{k}'\alpha})c^{\dagger}_{\vec{q}'n'}c_{\vec{q}n} \tag{A.8b}$$

with the standard definition:

$$g^{\vec{k}'\alpha}_{n',\vec{q}n} \equiv \int_{\Omega}d\vec{r}\psi^{*}_{\vec{q}+\vec{k}',n'}(\vec{r})\psi_{\vec{q}n}(\vec{r})\sum_{\vec{R}s}f^{\vec{k}'}_{\alpha s}\sqrt{\frac{\hbar}{2m_s\omega_{\vec{k}'\alpha}}}e^{i\vec{k}'\cdot\vec{R}}\partial_{\vec{R}s}V_{nuc}(\vec{r}) \tag{A.8c}$$

Now we take an aside to simplify the second-order perturbation theory transition matrix elements in a general framework. For simplicity, use a lumped electron state index (not labeling k-points explictly), and let the interaction hamiltonian be $H_1 = \sum_{i\neq j}\alpha_{1ij}(a_1 c^{\dagger}_i c_j + a^{\dagger}_1 c^{\dagger}_j c_i)$ and similarly for H_2. The general transition matrix elements are:

$$\mathcal{T} = \underbrace{\sum_{M}\frac{\langle F|\hat{H}_1|M\rangle\langle M|\hat{H}_2|I\rangle}{E_M - E_I}}_{\mathcal{T}_{12}} + (1\leftrightarrow 2), \tag{A.9}$$

where I, M, and F are the many-body initial, intermediate, and final states. Let $I = |0\rangle$ be the normalized initial state with some distribution of electrons and two types of bosons (call them type 1 and type 2; in our case, they are plamsons and phonons), and set the reference energy, $E_I = 0$. Let $F = \frac{c^{\dagger}_c c_v a_1 a_2|0\rangle}{\sqrt{(1-f_c)f_v n_1 n_2}}$ be the normalized final state with an electron-hole pair and two less bosons compared to the initial state, with relative energy $E_F = \varepsilon_c - \varepsilon_v - \omega_1 - \omega_2$.

The intermediate state should be summed over all possible many-body states. The H_2 expectation value will be non-zero only if M differs from I by a single electron-hole pair and a single boson of type 2 (in our case, a phonon). Likewise the H_1

expectation value will be non-zero only if M differs from F by a single electron-hole pair and a single boson of type 1 (in our case, a plasmon). Therefore $M = \frac{c_l^\dagger c_m a_2|0\rangle}{\sqrt{(1-f_l)f_m n_2}}$, indexed by two electron indices l, m with $l \neq m$, and energy $E_M = \varepsilon_l - \varepsilon_m - \omega_2$.

$$\mathcal{T}_{12} \equiv \sum_M \frac{\langle F|\hat{H}_1|M\rangle\langle M|\hat{H}_2|I\rangle}{E_M - E_I} \tag{A.10a}$$

$$= \sum_{l\neq m, w\neq x, y\neq z} \frac{\alpha_{1wx}\alpha_{2yz}\langle 0\left|a_2^\dagger a_1^\dagger c_v^\dagger c_c a_1 c_w^\dagger c_x c_l^\dagger c_m a_2\right|0\rangle\langle 0|a_2^\dagger c_m^\dagger c_l a_2 c_y^\dagger c_z^\dagger|0\rangle}{(\varepsilon_l - \varepsilon_m - \omega_2)(1-f_l)f_m n_2\sqrt{(1-f_c)f_v n_1 n_2}} \tag{A.10b}$$

$$= \sum_{l\neq m, w\neq x, y\neq z} \frac{\alpha_{1wx}\alpha_{2yz} n_2 n_1 n_2\langle 0|c_v^\dagger c_c c_w^\dagger c_x c_l^\dagger c_m|0\rangle\langle 0|c_m^\dagger c_l c_y^\dagger c_z|0\rangle}{(\varepsilon_l - \varepsilon_m - \omega_2)(1-f_l)f_m n_2\sqrt{(1-f_c)f_v n_1 n_2}} \tag{A.10c}$$

$$= \sqrt{\frac{n_1 n_2}{(1-f_c)f_v}} \sum_{l\neq m, w\neq x, y\neq z} \alpha_{1wx}\alpha_{2yz} \frac{\langle 0|c_v^\dagger c_c c_w^\dagger c_x c_l^\dagger c_m|0\rangle\langle 0|c_m^\dagger c_l c_y^\dagger c_z|0\rangle}{(\varepsilon_l - \varepsilon_m - \omega_2)(1-f_l)f_m} \tag{A.10d}$$

Simplifying the bosonic sector:

$$\begin{aligned}
\langle 0|c_m^\dagger c_l c_y^\dagger c_z|0\rangle &= \langle 0|c_m^\dagger(\delta_{ly} - c_y^\dagger c_l)c_z|0\rangle && \text{(A.11a)}\\
&= \langle 0|(c_m^\dagger c_z \delta_{ly} - c_m^\dagger c_y^\dagger c_l c_z)|0\rangle && \text{(A.11b)}\\
&= \delta_{ly}\delta_{mz} f_m - f_m f_y(\delta_{mz}\delta_{ly} - \delta_{ml}\delta_{yz}) && \text{(A.11c)}\\
&= \delta_{ly}\delta_{mz} f_m - f_m f_y \delta_{mz}\delta_{ly} (y \neq z, l \neq m) && \text{(A.11d)}\\
&= f_m(1-f_l)\delta_{mz}\delta_{ly} && \text{(A.11e)}
\end{aligned}$$

Plugging this back into $\mathcal{T}_{12}$ and simplifying:

$$\mathcal{T}_{12} = \sqrt{\frac{n_1 n_2}{(1-f_c)f_v}} \sum_{l\neq m, w\neq x, y\neq z} \alpha_{1wx}\alpha_{2yz} \frac{\langle 0|c_v^\dagger c_c c_w^\dagger c_x c_l^\dagger c_m|0\rangle f_m(1-f_l)\delta_{mz}\delta_{ly}}{(\varepsilon_l - \varepsilon_m - \omega_2)(1-f_l)f_m} \tag{A.12a}$$

$$= \sqrt{\frac{n_1 n_2}{(1-f_c)f_v}} \sum_{l\neq m, w\neq x} \alpha_{1wx}\alpha_{2lm} \frac{\langle 0|c_v^\dagger c_c c_w^\dagger c_x c_l^\dagger c_m|0\rangle}{\varepsilon_l - \varepsilon_m - \omega_2} \tag{A.12b}$$

$$\langle 0|c_v^\dagger c_c c_w^\dagger c_x c_l^\dagger c_m|0\rangle = \langle 0|(\delta_{cw} c_v^\dagger c_x c_l^\dagger c_m - c_v^\dagger c_w^\dagger c_c c_x c_l^\dagger c_m)|0\rangle \tag{A.13a}$$

$$= \langle 0|(\delta_{cw}\delta_{lx} c_v^\dagger c_m - \delta_{cw} c_v^\dagger c_l^\dagger c_x c_m - \delta_{lx} c_v^\dagger c_w^\dagger c_c c_m + c_v^\dagger c_w^\dagger c_c c_l^\dagger c_x c_m)|0\rangle \tag{A.13b}$$

$$= \langle 0|(\delta_{cw}\delta_{lx} c_v^\dagger c_m - \delta_{cw} c_v^\dagger c_l^\dagger c_x c_m - \delta_{lx} c_v^\dagger c_w^\dagger c_c c_m + \delta_{lc} c_v^\dagger c_w^\dagger c_x c_m - c_v^\dagger c_w^\dagger c_l^\dagger c_c c_x c_m)|0\rangle \tag{A.13c}$$

using $l \neq m, w \neq x, y \neq z$:

$$= \delta_{cw}\delta_{lx}(\delta_{mv} f_v) - \delta_{cw}(\delta_{vm}\delta_{lx} f_v f_l) - \delta_{lx}(\delta_{vm}\delta_{wc} f_v f_c) + \delta_{lc}(-\delta_{vx}\delta_{wm} f_v f_m) - (-\delta_{vx}\delta_{wm}\delta_{lc} f_v f_m f_c - \delta_{vm}\delta_{wc}\delta_{lx} f_v f_c f_l) \tag{A.13d}$$

$$= \delta_{vx}\delta_{wm}\delta_{lc}(-f_v f_m + f_v f_m f_c) + \delta_{vm}\delta_{wc}\delta_{lx}(f_v - f_v f_l - f_v f_c + f_v f_c f_l) \tag{A.13e}$$

$$= -\delta_{vx}\delta_{wm}\delta_{lc} f_v (1 - f_c) f_m + \delta_{vm}\delta_{wc}\delta_{lx} f_v (1 - f_l)(1 - f_c) \tag{A.13f}$$

$$= f_v (1 - f_c)[\delta_{vm}\delta_{wc}\delta_{lx}(1 - f_l) - \delta_{vx}\delta_{wm}\delta_{lc} f_m] \tag{A.13g}$$

$$\mathcal{T}_{12} = \sqrt{\frac{n_1 n_2}{(1-f_c)f_v}} \sum_{l\neq m, w\neq x} \alpha_{1wx}\alpha_{2lm} \frac{f_v(1-f_c)[\delta_{vm}\delta_{wc}\delta_{lx}(1-f_l) - \delta_{vx}\delta_{wm}\delta_{lc}f_m]}{\varepsilon_l - \varepsilon_m - \omega_2} \tag{A.14a}$$

$$= \sqrt{n_1 n_2 f_v(1-f_c)} \sum_{l\neq m, w\neq x} \alpha_{1wx}\alpha_{2lm} \frac{[\delta_{vm}\delta_{wc}\delta_{lx}(1-f_l) - \delta_{vx}\delta_{wm}\delta_{lc}f_m]}{\varepsilon_l - \varepsilon_m - \omega_2} \tag{A.14b}$$

$$= \sqrt{n_1 n_2 f_v(1-f_c)} \left(\sum_{l\neq v,c} \alpha_{1cl}\alpha_{2lv} \frac{(1-f_l)}{\varepsilon_l - \varepsilon_v - \omega_2} - \sum_{m\neq v,c} \alpha_{1mv}\alpha_{2cm} \frac{f_m}{\varepsilon_c - \varepsilon_m - \omega_2} \right) \tag{A.14c}$$

Relabeling dummy index $m \to l$

$$= \sqrt{n_1 n_2 f_v(1-f_c)} \left(\sum_{l\neq v,c} (1-f_l) \frac{\alpha_{1cl}\alpha_{2lv}}{\varepsilon_l - \varepsilon_v - \omega_2} + \sum_{l\neq v,c} f_l \frac{\alpha_{2cl}\alpha_{1lv}}{\varepsilon_l - \varepsilon_c + \omega_2} \right) \tag{A.14d}$$

Using energy conservation:

$$= \sqrt{n_1 n_2 f_v(1-f_c)} \sum_{l\neq v,c} \left[(1-f_l) \frac{\alpha_{1cl}\alpha_{2lv}}{\varepsilon_l - \varepsilon_v - \omega_2} + f_l \frac{\alpha_{2cl}\alpha_{1lv}}{\varepsilon_l - \varepsilon_v - \omega_1} \right] \tag{A.14e}$$

Substituting equation A.14e back into equation A.9,

$$\mathcal{T} = \mathcal{T}_{12} + \mathcal{T}_{21} \tag{A.15a}$$

$$= \sqrt{n_1 n_2 f_v(1-f_c)} \sum_{l\neq v,c} \left[\begin{array}{c} (1-f_l)\frac{\alpha_{1cl}\alpha_{2lv}}{\varepsilon_l - \varepsilon_v - \omega_2} + f_l \frac{\alpha_{2cl}\alpha_{1lv}}{\varepsilon_l - \varepsilon_v - \omega_1} \\ +(1-f_l)\frac{\alpha_{2cl}\alpha_{1lv}}{\varepsilon_l - \varepsilon_v - \omega_1} + f_l \frac{\alpha_{1cl}\alpha_{2lv}}{\varepsilon_l - \varepsilon_v - \omega_2} \end{array} \right] \tag{A.15b}$$

$$= \sqrt{n_1 n_2 f_v(1-f_c)} \sum_{l\neq v,c} \left[\frac{\alpha_{1cl}\alpha_{2lv}}{\varepsilon_l - \varepsilon_v - \omega_2} + \frac{\alpha_{2cl}\alpha_{1lv}}{\varepsilon_l - \varepsilon_v - \omega_1} \right] \tag{A.15c}$$

$$= \sqrt{n_1 n_2 f_v(1-f_c)} \sum_{l\neq v,c} \left[\frac{\alpha_{1cl}\alpha_{2lv}}{\varepsilon_l - \varepsilon_v - \omega_2} + (1 \leftrightarrow 2) \right]. \tag{A.15d}$$

Note that the occupation factors correspond intuitively to whether the particle is being absorbed or emitted. To switch from absorption to emission, $n \to n+1$ for each boson, and $f \to 1-f$ for each fermion. Also, in switching from absorption to emission, the signs on the corresponding energy in the denominator and energy-conserving delta are reversed, and we take the complex conjugate of the corresponding matrix element coefficient (α).

Returning to equation A.6 and using the above results to simplify:

$$\mathcal{T}^{kk'\alpha+}_{qn,q'n'} = \delta_{\vec{q}+\vec{k}',\vec{q}'}\sqrt{\frac{\pi\hbar e^2}{\omega L(\omega)|\gamma(z<0)|L_z S}\frac{1}{N_{\vec{k}'}}f_{\vec{q}n}(1-f_{\vec{q}'n'})n_{pl}n_{\vec{k}'\alpha}} \times \vec{\lambda}_{\vec{k}}\cdot\sum_l\left[\frac{\langle\hat{\vec{p}}\rangle^{\vec{q}'}_{n'l}g^{\vec{k}'\alpha}_{l,\vec{q}n}}{\bar{\varepsilon}_{\vec{q}'l}-(\varepsilon_{\vec{q}n}+\hbar\omega_{\vec{k}'\alpha})}+\frac{g^{\vec{k}'\alpha}_{n',\vec{q}l}\langle\hat{\vec{p}}\rangle^{\vec{q}}_{ln}}{\bar{\varepsilon}_{\vec{q}l}-(\varepsilon_{\vec{q}n}+\hbar\omega)}\right] \tag{A.16a}$$

Using energy conservation,$\vec{q}' = \vec{q}+\vec{k}'$:

$$= \delta_{\vec{q}+\vec{k}',\vec{q}'}\sqrt{\frac{\pi\hbar e^2}{\omega L(\omega)|\gamma(z<0)|N_{\vec{k}'}L_z S}f_{\vec{q}n}(1-f_{\vec{q}'n'})n_{pl}n_{\vec{k}'\alpha}} \times \vec{\lambda}_{\vec{k}}\cdot\sum_l\left[\frac{\langle\hat{\vec{p}}\rangle^{\vec{q}+\vec{k}'}_{n'l}g^{\vec{k}'\alpha}_{l,\vec{q}n}}{\bar{\varepsilon}_{\vec{q}+\vec{k}',l}-\varepsilon_{\vec{q}+\vec{k}',n'}-\hbar\omega_{\vec{k}'\alpha}}+\frac{g^{\vec{k}'\alpha}_{n',\vec{q}l}\langle\hat{\vec{p}}\rangle^{\vec{q}}_{ln}}{\bar{\varepsilon}_{\vec{q}l}-\varepsilon_{\vec{q}n}-\hbar\omega}\right] \tag{A.16b}$$

Similarly,

$$\mathcal{T}^{kk'\alpha-}_{qn,q'n'} = \delta_{\vec{q}+\vec{k}',\vec{q}'}\sqrt{\frac{\pi\hbar e^2}{\omega L(\omega)|\gamma(z<0)|N_{\vec{k}'}L_z S}f_{\vec{q}n}(1-f_{\vec{q}'n'})n_{pl}(n_{\vec{k}'\alpha}+1)} \times \vec{\lambda}_{\vec{k}}\cdot\sum_l\left[\frac{\langle\hat{\vec{p}}\rangle^{\vec{q}+\vec{k}'}_{n'l}g^{\vec{k}'\alpha}_{l,\vec{q}n}}{\bar{\varepsilon}_{\vec{q}+\vec{k}',l}-\varepsilon_{\vec{q}+\vec{k}',n'}+\hbar\omega_{\vec{k}'\alpha}}+\frac{g^{\vec{k}'\alpha}_{n',\vec{q}l}\langle\hat{\vec{p}}\rangle^{\vec{q}}_{ln}}{\bar{\varepsilon}_{\vec{q}l}-\varepsilon_{\vec{q}n}-\hbar\omega}\right] \tag{A.17}$$

Combining equations A.16b and A.17 gives

$$\mathcal{T}^{kk'\alpha\pm}_{qn,q'n'} = \delta_{\vec{q}+\vec{k}',\vec{q}'}\sqrt{\frac{\pi\hbar e^2}{\omega L(\omega)|\gamma(z<0)|N_{\vec{k}'}L_z S}f_{\vec{q}n}(1-f_{\vec{q}'n'})n_{pl}\left(n_{\vec{k}'\alpha}+\frac{1}{2}\mp\frac{1}{2}\right)} \times \vec{\lambda}_{\vec{k}}\cdot\sum_l\left[\frac{\langle\hat{\vec{p}}\rangle^{\vec{q}+\vec{k}'}_{n'l}g^{\vec{k}'\alpha}_{l,\vec{q}n}}{\bar{\varepsilon}_{\vec{q}+\vec{k}',l}-\varepsilon_{\vec{q}+\vec{k}',n'}\mp\hbar\omega_{\vec{k}'\alpha}}+\frac{g^{\vec{k}'\alpha}_{n',\vec{q}l}\langle\hat{\vec{p}}\rangle^{\vec{q}}_{ln}}{\bar{\varepsilon}_{\vec{q}l}-\varepsilon_{\vec{q}n}-\hbar\omega}\right] \tag{A.18}$$

Above, $\bar{\varepsilon}_{\vec{q}n} \equiv \varepsilon_{\vec{q}n} + iIm\Sigma_{\vec{q}n}$ is the complex eigenvalue of the intermediate state.

And finally, plugging this into equation A.5 and simplifying:

$$\Gamma_{\text{indirect}} = \frac{2\pi}{\hbar} \sum_{\vec{q}n\vec{q}'n'k'\alpha\pm} \delta(\varepsilon_{\vec{q}'n'} - \varepsilon_{\vec{q}n} - \hbar\omega \mp \hbar\omega_{\vec{k}'\alpha}) |\mathcal{T}^{kk'\alpha\pm}_{qn,q'n'}|^2 \tag{A.19a}$$

$$= \frac{2\pi}{\hbar} \frac{\pi\hbar e^2}{\omega L(\omega)|\gamma(z<0)|N_{\vec{k}'}L_z S} \times \sum_{\vec{q}nn'k'\alpha\pm} f_{\vec{q}n}(1 - f_{\vec{q}+\vec{k}',n'}) n_{pl} \left(n_{\vec{k}'\alpha} + \frac{1}{2} \mp \frac{1}{2}\right) \delta(\varepsilon_{\vec{q}+\vec{k}',n'} - \varepsilon_{\vec{q}n} - \hbar\omega \mp \hbar\omega_{\vec{k}'\alpha}) \times \left| \vec{\lambda}_{\vec{k}} \cdot \sum_l \left[\frac{\langle\hat{\vec{p}}\rangle^{\vec{q}+\vec{k}'}_{n'l} g^{\vec{k}'\alpha}_{l,\vec{q}n}}{\bar{\varepsilon}_{\vec{q}+\vec{k}',l} - \varepsilon_{\vec{q}+\vec{k}',n'} \mp \hbar\omega_{\vec{k}'\alpha}} + \frac{g^{\vec{k}'\alpha}_{n',\vec{q}l} \langle\hat{\vec{p}}\rangle^{\vec{q}}_{ln}}{\bar{\varepsilon}_{\vec{q}l} - \varepsilon_{\vec{q}n} - \hbar\omega} \right] \right|^2 \tag{A.19b}$$

$$= \frac{2\pi^2 e^2}{\omega L(\omega)|\gamma(z<0)|\Omega} \times \frac{1}{N_{\vec{q}} N_{\vec{k}'}} \times \sum_{\vec{q}\vec{k}'nn'\alpha\pm} f_{\vec{q}n}(1 - f_{\vec{q}+\vec{k}',n'}) n_{pl} \left(n_{\vec{k}'\alpha} + \frac{1}{2} \mp \frac{1}{2}\right) \delta(\varepsilon_{\vec{q}+\vec{k}',n'} - \varepsilon_{\vec{q}n} - \hbar\omega \mp \hbar\omega_{\vec{k}'\alpha}) \times \left| \vec{\lambda}_{\vec{k}} \cdot \sum_l \left[\frac{\langle\hat{\vec{p}}\rangle^{\vec{q}+\vec{k}'}_{n'l} g^{\vec{k}'\alpha}_{l,\vec{q}n}}{\bar{\varepsilon}_{\vec{q}+\vec{k}',l} - \varepsilon_{\vec{q}+\vec{k}',n'} \mp \hbar\omega_{\vec{k}'\alpha}} + \frac{g^{\vec{k}'\alpha}_{n',\vec{q}l} \langle\hat{\vec{p}}\rangle^{\vec{q}}_{ln}}{\bar{\varepsilon}_{\vec{q}l} - \varepsilon_{\vec{q}n} - \hbar\omega} \right] \right|^2 \tag{A.19c}$$

and repeating equation A.4d here for comparison :

$$\Gamma_{\text{direct}} = \frac{2\pi^2 e^2}{\omega L(\omega)|\gamma(z<0)|\Omega} \times \frac{1}{N_{\vec{q}}} \sum_{\vec{q}nn'} f_{\vec{q}n}(1 - f_{\vec{q}n'}) n_{pl} \delta(\varepsilon_{\vec{q}n'} - \varepsilon_{\vec{q}n} - \hbar\omega) |\vec{\lambda}_{\vec{k}} \cdot \langle\hat{\vec{p}}\rangle^{\vec{q}}_{n'n}|^2. \tag{A.20}$$

A.3 Final Expressions for Direct and Phonon-assisted Plasmon Decay After Accounting For Reverse Transitions

To calculate the net transition rate from plasmon occupation number $n_{pl} \to (n_{pl}-1)$, we need to account for the above absorption process as well as the corresponding emission processes that go from $(n_{pl} - 1) \to n_{pl}$. By detailed balance, the matrix element is exactly the same for absorption and emission and only the occupation factors for the fermions change: $f_v(1 - f_c) \to (1 - f_v)f_c$. The difference between the two processes has a fermion factor of $f_v(1 - f_c) - (1 - f_v)f_c = f_v - f_c$. Thus the final transition rates accounting for this are:

$$\Gamma_{\text{direct}} = \frac{2\pi^2 e^2}{\omega L(\omega)|\gamma(z<0)|\Omega} \times \frac{1}{N_{\vec{q}}} \sum_{\vec{q}nn'} (f_{\vec{q}n} - f_{\vec{q}n'}) n_{pl} \delta(\varepsilon_{\vec{q}n'} - \varepsilon_{\vec{q}n} - \hbar\omega) |\vec{\lambda}_{\vec{k}} \cdot \langle\hat{\vec{p}}\rangle^{\vec{q}}_{n'n}|^2 \tag{A.21}$$

$$\Gamma_{\text{indirect}} = \frac{2\pi^2 e^2}{\omega L(\omega)|\gamma(z<0)|\Omega} \times \frac{1}{N_{\vec{q}} N_{\vec{k}'}} \times \sum_{\vec{q}\vec{k}' n n' \alpha \pm} (f_{\vec{q}n} - f_{\vec{q}+\vec{k}',n'}) n_{pl} \left(n_{\vec{k}'\alpha} + \frac{1}{2} \mp \frac{1}{2} \right) \delta(\varepsilon_{\vec{q}+\vec{k}',n'} - \varepsilon_{\vec{q}n} - \hbar\omega \mp \hbar\omega_{\vec{k}'\alpha}) \times \left| \vec{\lambda}_{\vec{k}} \cdot \sum_{l} \left[\frac{\langle \hat{\vec{p}} \rangle_{n'l}^{\vec{q}+\vec{k}'} g_{l,\vec{q}n}^{\vec{k}'\alpha}}{\bar{\varepsilon}_{\vec{q}+\vec{k}',l} - \varepsilon_{\vec{q}+\vec{k}',n'} \mp \hbar\omega_{\vec{k}'\alpha}} + \frac{g_{n',\vec{q}l}^{\vec{k}'\alpha} \langle \hat{\vec{p}} \rangle_{ln}^{\vec{q}}}{\bar{\varepsilon}_{\vec{q}l} - \varepsilon_{\vec{q}n} - \hbar\omega} \right] \right|^2 \tag{A.22}$$

These are directly related to the expressions (4.2 and 4.3) for plasmon decay via direct and indirect transitions presented in Chapter 4.

Appendix B

TABULATED ELECTRONIC HEAT CAPACITY AND ELECTRON-PHONON COUPLING FACTOR AS A FUNCTION OF ELECTRON TEMPERATURE

Here we provide tabulated *ab initio* electronic heat capacity from expression 5.3 and electron-phonon coupling factor from expression 5.9 as a function of electron temperature for aluminum, silver, gold, and copper. See Chapter 5 for discussion of these parameters.

Table B.1: Tabulated electronic heat capacity and electron-phonon coupling factor as a function of electron temperature

T_e [K]	C_e [10^5 J/m^{3}K]				G [10^{17} W/m^3K]			
	Al	**Ag**	**Au**	**Cu**	**Al**	**Ag**	**Au**	**Cu**
300	0.279649	0.180129	0.184019	0.277610	5.039960	0.302574	0.245301	0.985599
400	0.376354	0.239219	0.245105	0.369473	5.208740	0.305198	0.248132	1.010650
500	0.472946	0.298001	0.306298	0.460837	5.312170	0.307018	0.250093	1.025440
600	0.568945	0.356496	0.367593	0.552057	5.381720	0.308271	0.251564	1.034980
700	0.664438	0.414751	0.428952	0.643278	5.431590	0.309100	0.252719	1.041480
800	0.759542	0.472777	0.490335	0.734512	5.468990	0.309607	0.253649	1.046040
900	0.854331	0.530547	0.551705	0.825722	5.497950	0.309869	0.254410	1.049250
1000	0.948845	0.588019	0.613042	0.916856	5.520900	0.309941	0.255039	1.051500
1100	1.043110	0.645156	0.674336	1.007870	5.539410	0.309867	0.255563	1.053030
1200	1.137150	0.701925	0.735593	1.098750	5.554560	0.309681	0.256005	1.054020
1300	1.230990	0.758311	0.796824	1.189480	5.567120	0.309408	0.256379	1.054590
1400	1.324650	0.814307	0.858050	1.280090	5.577650	0.309067	0.256701	1.054830
1500	1.418170	0.869918	0.919296	1.370680	5.586580	0.308674	0.256979	1.054830
1600	1.511560	0.925154	0.980596	1.461390	5.594240	0.308240	0.257224	1.054620
1700	1.604860	0.980032	1.041990	1.552470	5.600880	0.307774	0.257441	1.054270
1800	1.698070	1.034570	1.103550	1.644260	5.606710	0.307285	0.257638	1.053840
1900	1.791220	1.088790	1.165350	1.737240	5.611880	0.306777	0.257819	1.053360
2000	1.884320	1.142700	1.227490	1.832020	5.616510	0.306256	0.257991	1.052900
2100	1.977390	1.196330	1.290100	1.929310	5.620710	0.305725	0.258160	1.052540
2200	2.070440	1.249690	1.353330	2.029960	5.624550	0.305189	0.258331	1.052340
2300	2.163480	1.302800	1.417370	2.134900	5.628080	0.304649	0.258510	1.052400
2400	2.256530	1.355670	1.482440	2.245110	5.631370	0.304107	0.258706	1.052800
2500	2.349590	1.408310	1.548750	2.361640	5.634440	0.303565	0.258925	1.053670
2600	2.442670	1.460740	1.616580	2.485540	5.637340	0.303026	0.259178	1.055100
2700	2.535800	1.512980	1.686190	2.617820	5.640080	0.302488	0.259473	1.057220
2800	2.628960	1.565050	1.757850	2.759470	5.642680	0.301955	0.259820	1.060140
2900	2.722190	1.616970	1.831870	2.911410	5.645170	0.301426	0.260230	1.063990
3000	2.815480	1.668780	1.908520	3.074450	5.647560	0.300903	0.260715	1.068870
3100	2.908850	1.720530	1.988090	3.249310	5.649860	0.300387	0.261286	1.074900
3200	3.002310	1.772260	2.070850	3.436580	5.652080	0.299878	0.261955	1.082180
3300	3.095860	1.824040	2.157060	3.636740	5.654240	0.299377	0.262734	1.090820

Continued on next page

Table B.1 – *Continued from previous page*

T_e [K]	C_e [10^5 J/m^{3}K]				G [10^{17} W/m^3K]			
	Al	Ag	Au	Cu	Al	Ag	Au	Cu
3400	3.189520	1.875940	2.246960	3.850120	5.656340	0.298886	0.263635	1.100880
3500	3.283280	1.928050	2.340780	4.076910	5.658390	0.298406	0.264670	1.112450
3600	3.377170	1.980480	2.438720	4.317190	5.660400	0.297939	0.265848	1.125580
3700	3.471180	2.033330	2.540940	4.570880	5.662370	0.297485	0.267182	1.140320
3800	3.565320	2.086730	2.647590	4.837810	5.664310	0.297049	0.268681	1.156690
3900	3.659590	2.140830	2.758800	5.117680	5.666230	0.296631	0.270355	1.174720
4000	3.754010	2.195760	2.874650	5.410090	5.668130	0.296234	0.272211	1.194410
4100	3.848560	2.251700	2.995200	5.714540	5.670020	0.295862	0.274257	1.215740
4200	3.943260	2.308810	3.120500	6.030460	5.671890	0.295517	0.276501	1.238700
4300	4.038110	2.367270	3.250550	6.357220	5.673770	0.295203	0.278947	1.263240
4400	4.133100	2.427280	3.385330	6.694130	5.675640	0.294924	0.281599	1.289320
4500	4.228240	2.489010	3.524820	7.040450	5.677510	0.294683	0.284461	1.316880
4600	4.323530	2.552670	3.668940	7.395420	5.679390	0.294486	0.287536	1.345860
4700	4.418960	2.618460	3.817610	7.758260	5.681280	0.294337	0.290824	1.376190
4800	4.514530	2.686580	3.970740	8.128180	5.683190	0.294240	0.294327	1.407790
4900	4.610250	2.757230	4.128210	8.504390	5.685100	0.294200	0.298042	1.440580
5000	4.706100	2.830610	4.289890	8.886120	5.687030	0.294224	0.301969	1.474470
5100	4.802080	2.906900	4.455620	9.272590	5.688980	0.294315	0.306105	1.509370
5200	4.898200	2.986320	4.625270	9.663060	5.690950	0.294480	0.310446	1.545200
5300	4.994440	3.069030	4.798660	10.056800	5.692940	0.294723	0.314989	1.581870
5400	5.090800	3.155210	4.975620	10.453200	5.694950	0.295051	0.319728	1.619280
5500	5.187280	3.245040	5.155980	10.851500	5.696990	0.295469	0.324659	1.657360
5600	5.283870	3.338680	5.339570	11.251100	5.699050	0.295982	0.329775	1.696020
5700	5.380560	3.436270	5.526190	11.651500	5.701130	0.296596	0.335069	1.735170
5800	5.477360	3.537960	5.715660	12.052000	5.703240	0.297317	0.340535	1.774740
5900	5.574250	3.643870	5.907820	12.452300	5.705370	0.298149	0.346167	1.814650
6000	5.671230	3.754120	6.102460	12.851800	5.707530	0.299098	0.351955	1.854830
6100	5.768300	3.868800	6.299430	13.250100	5.709710	0.300168	0.357893	1.895210
6200	5.865440	3.988020	6.498540	13.646800	5.711920	0.301365	0.363973	1.935720
6300	5.962660	4.111840	6.699630	14.041500	5.714150	0.302693	0.370187	1.976310
6400	6.059940	4.240320	6.902520	14.433900	5.716410	0.304156	0.376526	2.016910
6500	6.157280	4.373520	7.107070	14.823700	5.718680	0.305758	0.382984	2.057480
6600	6.254680	4.511460	7.313110	15.210700	5.720990	0.307503	0.389551	2.097960
6700	6.352120	4.654180	7.520500	15.594600	5.723310	0.309395	0.396221	2.138310
6800	6.449600	4.801660	7.729100	15.975200	5.725650	0.311436	0.402986	2.178490
6900	6.547120	4.953920	7.938770	16.352300	5.728020	0.313630	0.409837	2.218450
7000	6.644670	5.110920	8.149380	16.725700	5.730400	0.315978	0.416768	2.258170
7100	6.742240	5.272640	8.360810	17.095300	5.732800	0.318483	0.423771	2.297610
7200	6.839820	5.439030	8.572940	17.461100	5.735220	0.321146	0.430840	2.336740
7300	6.937420	5.610030	8.785660	17.822800	5.737660	0.323970	0.437967	2.375540
7400	7.035020	5.785580	8.998870	18.180400	5.740110	0.326954	0.445146	2.413980
7500	7.132620	5.965600	9.212480	18.533800	5.742570	0.330100	0.452370	2.452040
7600	7.230220	6.150000	9.426380	18.883100	5.745050	0.333408	0.459634	2.489700
7700	7.327800	6.338690	9.640490	19.228000	5.747540	0.336877	0.466932	2.526960
7800	7.425360	6.531550	9.854730	19.568700	5.750040	0.340508	0.474258	2.563790
7900	7.522900	6.728490	10.069000	19.905000	5.752550	0.344300	0.481607	2.600180
8000	7.620400	6.929360	10.283300	20.237000	5.755070	0.348251	0.488974	2.636120
8100	7.717870	7.134060	10.497500	20.564700	5.757600	0.352360	0.496353	2.671600
8200	7.815300	7.342440	10.711600	20.888100	5.760130	0.356626	0.503741	2.706620
8300	7.912680	7.554370	10.925400	21.207200	5.762670	0.361046	0.511134	2.741180
8400	8.010010	7.769710	11.139000	21.522000	5.765210	0.365619	0.518526	2.775250

Continued on next page

Table B.1 – *Continued from previous page*

T_e [K]	C_e [10^5 J/m^{3}K]				G [10^{17} W/m^3K]			
	Al	**Ag**	**Au**	**Cu**	**Al**	**Ag**	**Au**	**Cu**
8500	8.107280	7.988310	11.352300	21.832600	5.767760	0.370341	0.525914	2.808850
8600	8.204490	8.210020	11.565300	22.139000	5.770300	0.375211	0.533295	2.841980
8700	8.301620	8.434690	11.777800	22.441200	5.772850	0.380225	0.540665	2.874620
8800	8.398690	8.662170	11.989900	22.739200	5.775400	0.385380	0.548021	2.906780
8900	8.495670	8.892310	12.201600	23.033200	5.777940	0.390673	0.555361	2.938460
9000	8.592570	9.124950	12.412700	23.323100	5.780490	0.396100	0.562680	2.969670
9100	8.689380	9.359940	12.623300	23.609100	5.783030	0.401658	0.569977	3.000400
9200	8.786090	9.597130	12.833400	23.891200	5.785560	0.407343	0.577248	3.030660
9300	8.882700	9.836360	13.042800	24.169300	5.788100	0.413151	0.584493	3.060450
9400	8.979210	10.077500	13.251700	24.443700	5.790620	0.419078	0.591708	3.089780
9500	9.075610	10.320400	13.459900	24.714300	5.793140	0.425120	0.598893	3.118640
9600	9.171900	10.564800	13.667400	24.981300	5.795650	0.431273	0.606044	3.147060
9700	9.268060	10.810700	13.874300	25.244600	5.798150	0.437534	0.613160	3.175020
9800	9.364110	11.058000	14.080400	25.504300	5.800640	0.443897	0.620240	3.202530
9900	9.460020	11.306400	14.285900	25.760600	5.803120	0.450358	0.627282	3.229610
10000	9.555800	11.555800	14.490600	26.013400	5.805590	0.456914	0.634286	3.256260
10100	9.651450	11.806200	14.694600	26.262800	5.808040	0.463560	0.641249	3.282480
10200	9.746950	12.057300	14.897800	26.508900	5.810490	0.470292	0.648171	3.308280
10300	9.842310	12.309100	15.100200	26.751800	5.812920	0.477105	0.655051	3.333670
10400	9.937520	12.561500	15.301900	26.991500	5.815330	0.483996	0.661887	3.358650
10500	10.032600	12.814200	15.502800	27.228100	5.817740	0.490961	0.668680	3.383230
10600	10.127500	13.067300	15.702800	27.461600	5.820120	0.497995	0.675428	3.407420
10700	10.222200	13.320600	15.902100	27.692200	5.822490	0.505095	0.682131	3.431220
10800	10.316800	13.573900	16.100600	27.919800	5.824840	0.512256	0.688788	3.454640
10900	10.411200	13.827300	16.298200	28.144500	5.827180	0.519475	0.695399	3.477690
11000	10.505400	14.080600	16.495000	28.366400	5.829490	0.526748	0.701962	3.500380
11100	10.599500	14.333700	16.691000	28.585600	5.831790	0.534071	0.708479	3.522710
11200	10.693300	14.586500	16.886200	28.802100	5.834070	0.541441	0.714949	3.544690
11300	10.787000	14.839000	17.080500	29.015900	5.836330	0.548854	0.721370	3.566320
11400	10.880500	15.091000	17.273900	29.227200	5.838570	0.556306	0.727744	3.587620
11500	10.973800	15.342600	17.466500	29.435900	5.840780	0.563795	0.734069	3.608580
11600	11.067000	15.593500	17.658300	29.642200	5.842980	0.571317	0.740347	3.629220
11700	11.159900	15.843800	17.849200	29.846100	5.845150	0.578869	0.746576	3.649550
11800	11.252600	16.093400	18.039200	30.047600	5.847310	0.586448	0.752756	3.669560
11900	11.345100	16.342300	18.228400	30.246800	5.849440	0.594051	0.758888	3.689280
12000	11.437400	16.590300	18.416700	30.443700	5.851540	0.601675	0.764972	3.708690
12100	11.529500	16.837400	18.604100	30.638500	5.853630	0.609318	0.771008	3.727810
12200	11.621400	17.083600	18.790700	30.831100	5.855690	0.616975	0.776995	3.746650
12300	11.713100	17.328800	18.976400	31.021500	5.857720	0.624647	0.782935	3.765210
12400	11.804600	17.573100	19.161200	31.210000	5.859740	0.632328	0.788826	3.783490
12500	11.895800	17.816200	19.345200	31.396400	5.861720	0.640018	0.794669	3.801510
12600	11.986900	18.058300	19.528300	31.580800	5.863680	0.647714	0.800465	3.819270
12700	12.077700	18.299300	19.710500	31.763300	5.865620	0.655413	0.806213	3.836770
12800	12.168200	18.539100	19.891900	31.943900	5.867530	0.663114	0.811914	3.854030
12900	12.258600	18.777700	20.072400	32.122700	5.869410	0.670814	0.817568	3.871030
13000	12.348700	19.015100	20.252000	32.299700	5.871270	0.678512	0.823174	3.887800
13100	12.438600	19.251200	20.430800	32.475000	5.873100	0.686206	0.828735	3.904340
13200	12.528200	19.486100	20.608700	32.648500	5.874910	0.693894	0.834249	3.920650
13300	12.617600	19.719700	20.785800	32.820300	5.876680	0.701574	0.839717	3.936730
13400	12.706800	19.952000	20.961900	32.990500	5.878430	0.709244	0.845139	3.952600
13500	12.795700	20.183000	21.137300	33.159200	5.880160	0.716904	0.850515	3.968250

Continued on next page

Table B.1 – *Continued from previous page*

T_e [K]	C_e [10^5 J/m^{3}K]				G [10^{17} W/m^3K]			
	Al	Ag	Au	Cu	Al	Ag	Au	Cu
13600	12.884400	20.412600	21.311700	33.326200	5.881850	0.724551	0.855847	3.983690
13700	12.972900	20.640900	21.485300	33.491700	5.883520	0.732184	0.861133	3.998930
13800	13.061100	20.867900	21.658100	33.655700	5.885160	0.739802	0.866375	4.013970
13900	13.149000	21.093500	21.830000	33.818300	5.886770	0.747404	0.871573	4.028810
14000	13.236800	21.317700	22.001000	33.979400	5.888350	0.754988	0.876727	4.043460
14100	13.324200	21.540500	22.171200	34.139200	5.889900	0.762553	0.881837	4.057920
14200	13.411400	21.762000	22.340600	34.297600	5.891420	0.770097	0.886904	4.072200
14300	13.498400	21.982000	22.509100	34.454600	5.892920	0.777621	0.891928	4.086300
14400	13.585100	22.200700	22.676800	34.610400	5.894380	0.785123	0.896909	4.100220
14500	13.671500	22.418000	22.843600	34.764800	5.895820	0.792602	0.901848	4.113980
14600	13.757700	22.633800	23.009600	34.918100	5.897230	0.800058	0.906746	4.127560
14700	13.843700	22.848300	23.174800	35.070100	5.898600	0.807488	0.911601	4.140980
14800	13.929300	23.061400	23.339200	35.220900	5.899950	0.814893	0.916416	4.154240
14900	14.014800	23.273100	23.502700	35.370600	5.901270	0.822272	0.921189	4.167340
15000	14.099900	23.483400	23.665400	35.519100	5.902550	0.829624	0.925922	4.180290
15100	14.184800	23.692300	23.827300	35.666600	5.903810	0.836949	0.930615	4.193080
15200	14.269400	23.899800	23.988400	35.812900	5.905040	0.844245	0.935269	4.205730
15300	14.353800	24.106000	24.148700	35.958200	5.906230	0.851513	0.939882	4.218230
15400	14.437900	24.310800	24.308200	36.102500	5.907400	0.858752	0.944457	4.230590
15500	14.521800	24.514200	24.466900	36.245700	5.908530	0.865960	0.948993	4.242810
15600	14.605400	24.716300	24.624800	36.388000	5.909640	0.873139	0.953490	4.254890
15700	14.688700	24.917000	24.781900	36.529300	5.910710	0.880287	0.957950	4.266840
15800	14.771800	25.116300	24.938300	36.669600	5.911750	0.887403	0.962371	4.278660
15900	14.854600	25.314400	25.093800	36.809100	5.912760	0.894489	0.966756	4.290340
16000	14.937100	25.511100	25.248600	36.947600	5.913740	0.901542	0.971103	4.301910
16100	15.019400	25.706500	25.402600	37.085200	5.914690	0.908563	0.975414	4.313340
16200	15.101400	25.900500	25.555900	37.222000	5.915610	0.915552	0.979689	4.324660
16300	15.183100	26.093300	25.708400	37.357900	5.916500	0.922508	0.983927	4.335860
16400	15.264600	26.284800	25.860100	37.493000	5.917350	0.929432	0.988130	4.346940
16500	15.345800	26.475000	26.011100	37.627400	5.918180	0.936322	0.992298	4.357900
16600	15.426700	26.663900	26.161300	37.760900	5.918970	0.943178	0.996430	4.368760
16700	15.507400	26.851600	26.310900	37.893600	5.919730	0.950001	1.000530	4.379500
16800	15.587800	27.038000	26.459600	38.025600	5.920470	0.956791	1.004590	4.390130
16900	15.667900	27.223200	26.607700	38.156900	5.921160	0.963546	1.008620	4.400660
17000	15.747800	27.407200	26.755000	38.287400	5.921830	0.970267	1.012620	4.411080
17100	15.827400	27.589900	26.901600	38.417200	5.922470	0.976955	1.016580	4.421390
17200	15.906700	27.771500	27.047500	38.546300	5.923070	0.983608	1.020510	4.431610
17300	15.985800	27.951800	27.192700	38.674800	5.923650	0.990226	1.024410	4.441730
17400	16.064600	28.131000	27.337200	38.802600	5.924190	0.996810	1.028270	4.451750
17500	16.143200	28.309000	27.481000	38.929700	5.924700	1.003360	1.032110	4.461670
17600	16.221400	28.485800	27.624100	39.056200	5.925180	1.009880	1.035910	4.471500
17700	16.299500	28.661500	27.766500	39.182100	5.925620	1.016360	1.039680	4.481230
17800	16.377200	28.836000	27.908200	39.307400	5.926040	1.022800	1.043410	4.490870
17900	16.454700	29.009400	28.049300	39.432100	5.926420	1.029210	1.047120	4.500430
18000	16.531900	29.181700	28.189700	39.556200	5.926770	1.035590	1.050800	4.509890
18100	16.608900	29.352900	28.329400	39.679700	5.927090	1.041930	1.054450	4.519270
18200	16.685600	29.523000	28.468500	39.802700	5.927380	1.048240	1.058060	4.528560
18300	16.762100	29.692000	28.606900	39.925100	5.927640	1.054510	1.061650	4.537760
18400	16.838200	29.859900	28.744700	40.047000	5.927860	1.060750	1.065210	4.546880
18500	16.914200	30.026800	28.881900	40.168300	5.928060	1.066960	1.068740	4.555920
18600	16.989800	30.192600	29.018400	40.289200	5.928220	1.073130	1.072240	4.564880

Continued on next page

Table B.1 – *Continued from previous page*

T_e **[K]**	C_e [10^5 **J/m^{3}K**]				**G** [10^{17} **W/m^3K**]			
	Al	**Ag**	**Au**	**Cu**	**Al**	**Ag**	**Au**	**Cu**
18700	17.065200	30.357400	29.154300	40.409500	5.928350	1.079260	1.075710	4.573760
18800	17.140400	30.521200	29.289600	40.529300	5.928450	1.085360	1.079150	4.582560
18900	17.215300	30.683900	29.424200	40.648700	5.928510	1.091430	1.082570	4.591280
19000	17.289900	30.845700	29.558200	40.767500	5.928550	1.097460	1.085960	4.599930
19100	17.364300	31.006400	29.691700	40.885900	5.928550	1.103460	1.089320	4.608500
19200	17.438400	31.166200	29.824500	41.003800	5.928530	1.109430	1.092650	4.616990
19300	17.512300	31.325000	29.956800	41.121300	5.928470	1.115360	1.095960	4.625410
19400	17.585900	31.482800	30.088400	41.238400	5.928380	1.121250	1.099240	4.633760
19500	17.659200	31.639700	30.219500	41.354900	5.928260	1.127120	1.102490	4.642040
19600	17.732300	31.795700	30.350000	41.471100	5.928100	1.132950	1.105720	4.650250
19700	17.805200	31.950700	30.479900	41.586900	5.927920	1.138740	1.108920	4.658390
19800	17.877800	32.104700	30.609300	41.702200	5.927700	1.144510	1.112100	4.666460
19900	17.950200	32.257900	30.738100	41.817100	5.927460	1.150240	1.115250	4.674460
20000	18.022300	32.410200	30.866300	41.931600	5.927180	1.155930	1.118380	4.682390

Appendix C

DIELECTRIC FUNCTION TEMPERATURE DEPENDENCE PREFACTOR DERIVATION

The energy dependence of the electron-electron scattering rate is given by $\frac{1}{\tau_{ee}} = D_e(E - E_F)^2$, with prefactor D_e given in Reference [123], equation 10 (converted to atomic units) as:

$$\frac{1}{\tau_{ee}(E)} = \frac{(4\pi)^2(E - E_F)^2}{64\pi^3\varepsilon_b^2 E_s^{3/2}\sqrt{E_F}} \times \left[\frac{2\sqrt{E_F E_s}}{4E_F + E_s} + \arctan\sqrt{\frac{4E_F}{E_s}}\right] \tag{C.1}$$

$$D_e = \frac{1}{4\pi\varepsilon_b^2 E_s^{3/2}\sqrt{E_F}} \times \left[\frac{2\sqrt{E_F E_s}}{4E_F + E_s} + \arctan\sqrt{\frac{4E_F}{E_s}}\right]. \tag{C.2}$$

To derive an expression for the prefactor, which we will call A, for the temperature dependent form $\frac{1}{\tau_{ee}} = AT_e^2$, we begin with equation 8 from Reference [123]

$$\frac{df(E = E_F, T)}{dt}\Big|_{e-e} = \frac{(4\pi)^2}{32\pi^3\varepsilon_b^2 E_s\sqrt{E_F}} \int\int dE_1 dE_2 \left[\frac{\sqrt{\tilde{E}}}{\tilde{E} + E_s} + \frac{1}{\sqrt{E_s}}\arctan\sqrt{\frac{\tilde{E}}{E_s}}\right]_{\tilde{E}_{\min}}^{\tilde{E}_{\max}} \times \{[1 - f(E_1)]f(E_2)f(E_3) + f(E_1)[1 - f(E_2)][1 - f(E_3)]\} \tag{C.3}$$

with $\tilde{E}_{\max} = \inf\left\{\left(\sqrt{E_1} + \sqrt{E_3}\right)^2; \left(\sqrt{E_F} + \sqrt{E_2}\right)^2\right\}$ and $\tilde{E}_{\min} = \sup\left\{\left(\sqrt{E_1} - \sqrt{E_3}\right)^2; \left(\sqrt{E_F} - \sqrt{E_2}\right)^2\right\}$. Take $\tilde{E}_{\min} = 0$. $\tilde{E}_{\max}$ is slowly varying in E_1 and E_2, therefore, approximate $\tilde{E}_{\max}$ as a constant equal to its value at $E_1 = E_2 = E_F$: $\tilde{E}_{\max} \approx 4E_F$

$$\left[\frac{\sqrt{\tilde{E}}}{\tilde{E} + E_s} + \frac{1}{\sqrt{E_s}}\arctan\sqrt{\frac{\tilde{E}}{E_s}}\right]_{\tilde{E}_{\min}}^{\tilde{E}_{\max}} \approx \left[\frac{\sqrt{\tilde{E}}}{\tilde{E} + E_s} + \frac{1}{\sqrt{E_s}}\arctan\sqrt{\frac{\tilde{E}}{E_s}}\right]_0^{4E_F} \tag{C.4a}$$

$$= \frac{2\sqrt{E_F}}{4E_F + E_s} + \frac{1}{\sqrt{E_s}}\arctan\sqrt{\frac{4E_F}{E_s}} \tag{C.4b}$$

The temperature dependence of expression C.3 lies in the occupation factors term:

$$F(E_1, E_2) = (1 - f(E_1))f(E_2)f(E_3) + f(E_1)(1 - f(E_2))(1 - f(E_3)) \tag{C.5}$$

We can simplify this expression using

$$f(E)f(E_1)(1-f(E_2))(1-f(E_3)) = (1-f(E))(1-f(E_1))f(E_2)f(E_3) \quad \text{(C.6)}$$

to write $f(E_3)$ in terms of the other occupation factors as

$$f(E_3) = \frac{f(E)f(E_1)(1-f(E_2))}{f(E)f(E_1)+f(E_2)-f(E)f(E_2)-f(E_1)f(E_2)} \quad \text{(C.7)}$$

and replacing E by E_F and using $f(E=E_F) = 1/2$:

$$f(E_3) = \frac{\frac{1}{2}f(E_1)(1-f(E_2))}{\frac{1}{2}f(E_1)+\frac{1}{2}f(E_2)-f(E_1)f(E_2)}. \quad \text{(C.8)}$$

Substituting this into the occupation factors term:

$$F(E_1,E_2) = (1-f(E_1))f(E_2)\frac{\frac{1}{2}f(E_1)(1-f(E_2))}{\frac{1}{2}f(E_1)+\frac{1}{2}f(E_2)-f(E_1)f(E_2)}. \quad \text{(C.9)}$$

This is only nonzero around E_F in both the E_1 and E_2 direction, so we evaluate the term at $E_1 = E_2 = E_F$:

$$F(E_F,E_F) = (1-f(E_F))f(E_F)\frac{\frac{1}{2}f(E_F)(1-f(E_F))}{\frac{1}{2}f(E_F)+\frac{1}{2}f(E_F)-f(E_F)f(E_F)} \quad \text{(C.10a)}$$

$$= \frac{1}{2}\frac{1}{2}\frac{\frac{1}{2}\frac{1}{2}\frac{1}{2}}{\frac{1}{2}\frac{1}{2}+\frac{1}{2}\frac{1}{2}-\frac{1}{2}\frac{1}{2}} \quad \text{(C.10b)}$$

$$= \frac{\frac{1}{2}\frac{1}{2}\frac{1}{2}}{1+1-1} \quad \text{(C.10c)}$$

$$F(E_F,E_F) = 1/8 \quad \text{(C.10d)}$$

Substituting this into expression C.3

$$\frac{df(E=E_F,T_e)}{dt}\Big|_{e-e} \approx \frac{(4\pi)^2}{32\pi^3\varepsilon_b^2 E_s\sqrt{E_F}}\int\int dE_1 dE_2 \times\left[\frac{2\sqrt{E_F}}{4E_F+E_s}+\frac{1}{\sqrt{E_s}}\arctan\sqrt{\frac{4E_F}{E_s}}\right]F(E_1,E_2) \tag{C.11a}$$

$$= \frac{(4\pi)^2}{32\pi^3\varepsilon_b^2 E_s\sqrt{E_F}}\left[\frac{2\sqrt{E_F}}{4E_F+E_s}+\frac{1}{\sqrt{E_s}}\arctan\sqrt{\frac{4E_F}{E_s}}\right]\times\int\int dE_1 dE_2 F(E_1,E_2) \tag{C.11b}$$

$$= \frac{(4\pi)^2}{32\pi^3\varepsilon_b^2 E_s\sqrt{E_F}}\left[\frac{2\sqrt{E_F}}{4E_F+E_s}+\frac{1}{\sqrt{E_s}}\arctan\sqrt{\frac{4E_F}{E_s}}\right]\frac{\pi^2}{2}T_e^2 \tag{C.11c}$$

$$= \frac{(4\pi)^2}{64\pi^3\varepsilon_b^2 E_s\sqrt{E_F}}\frac{\sqrt{E_s}}{\sqrt{E_s}}\left[\frac{2\sqrt{E_F}}{4E_F+E_s}+\frac{1}{\sqrt{E_s}}\arctan\sqrt{\frac{4E_F}{E_s}}\right]\pi^2 T_e^2 \tag{C.11d}$$

$$= \frac{(4\pi)^2}{64\pi^3\varepsilon_b^2 E_s^{3/2}\sqrt{E_F}}\left[\frac{2\sqrt{E_F E_s}}{4E_F+E_s}+\arctan\sqrt{\frac{4E_F}{E_s}}\right]\pi^2 T^2 \tag{C.11e}$$

$$= \pi^2 D_e T_e^2 \tag{C.11f}$$

$$= AT_e^2. \tag{C.11g}$$

Thus, $A = \pi^2 D_e$ (in atomic units); the prefactors for the energy and temperature dependence of the electron-electron scattering rate are related by a factor of π^2.